



**Politecnico
di Torino**

Politecnico di Torino

Master's Degree in Aerospace Engineering

Master's Degree Thesis

Dynamic virtualization of a small-scale wind turbine

Supervisors

Prof. Dr. Alfonso PAGANI

Prof. Dr. Matteo FILIPPI

Eng. Silvia VETTORI

Eng. Dr. Emilio DI LORENZO

Eng. Dr. Alberto GARCIA DE MIGUEL

Candidate

Alessia ANTONACI

April 2023

Abstract

The use of wind turbines for clean energy generation has grown rapidly in recent years due to their cost-effectiveness and mature manufacturing technology. However, these structures experience complex and nonlinear conditions during operation, which necessitates early damage detection. As a result, it is important to use both numerical and experimental methods to characterize the dynamic properties of wind turbines. Experimental Modal Analysis (EMA) is typically used to conduct laboratory tests on scaled models, while Operational Modal Analysis (OMA) is used for full-scale wind turbines. OMA enables the implementation of structural health monitoring strategies (SHM) to assess wind turbine conditions and detect potential damages. Additionally, experimental data can be used to update numerical models with the purpose of implementing a dynamic virtualization process. This thesis focuses on analyzing a scaled wind turbine specimen using EMA and exploring the potential of OMA for wind turbine health monitoring.

This dissertation summarizes a six-month work experience at Siemens Digital Industries Software. The work focuses on the analysis of a scaled wind turbine using numerical modeling and EMA. The potential of OMA has also been explored to perform SHM of the scaled wind turbine. The primary objective is to estimate the modal parameters by integrating test and numerical techniques. To accomplish this, a numerical model is developed and validated using mathematical modeling techniques and simulation tools that replicate the wind turbine's dynamic response.

The tower model is initially developed in Simcenter 3D and preliminary modal properties are estimated. Subsequently, EMA is carried out using a modal impact hammer and acquired data is used to estimate the modal properties via Simcenter PolyMax. To assess the reliability of the numerical results, modal data from the Finite Element (FE) analysis are compared to modal test outputs. The tower FE model is successfully updated using the Model Update tool in Simcenter 3D, which employs a genetic algorithm for optimizing the model parameters, to better fit the numerical and experimental results. The modal analysis reveals that the first five mode shapes for the wind turbine comprise the first and second tower bending in both the fore-aft (FA) and side-side (SS) directions, representing the fundamental tower mode shapes for a wind turbine.

The entire wind turbine system is then subjected to numerical and experimental modal analysis. Two types of tests are conducted: experimental modal analysis and operational modal analysis. It is noteworthy that the dynamic behavior of the structure is primarily influenced by the dominant blades, resulting in the presence of only the first bending in the tower's fore-aft and side-side directions. The results of both numerical and experimental analyses indicate that the primary mode shapes for the wind turbine are the tower bending, the first three flap-wise modes, as well as the two edgewise modes and the second group of flap-wise modes.

Finally, OMA is carried out with rotating blades to verify the applicability of this technique and compare the results with the experimental and numerical ones. The outcomes of the tests validate the previous results and demonstrate the reliability of this innovative modal testing technology.

Contents

List of Tables	III
List of Figures	IV
1 Introduction	1
1.1 Framework and Motivation	1
2 Experimental Modal Analysis: an Overview	6
2.1 Modal analysis identification techniques	6
2.2 Leakage and windowing	8
2.3 Model correlation theory	8
3 Operational Modal Analysis: an Overview	10
3.1 Theoretical basis	10
3.2 PolyMax method	11
3.3 OMA benefits and drawbacks	13
3.4 Wind Turbine OMA Historical background	14
4 Structural Health Monitoring	17
4.1 SHM System for helicopter composite blades	17
4.2 SHM for space structures	19
4.3 Damage detection on wind turbines	21
4.4 Response estimation techniques for Wind Turbine SHM	23
5 Wind Turbine FE Model	26
5.1 Model Description	26
5.2 Material Description	27
5.3 FE modeling	28
5.3.1 Gluing and 1D connections	30
5.3.2 Boundary conditions	34
5.4 Eigenvalue solution	36
5.4.1 Tower and hub modal parameters	36
5.4.2 Wind turbine modal parameters	39

6	Wind turbine EMA results	42
6.1	Wind turbine tower EMA	42
6.1.1	Pre-Test Solution Process	42
6.1.2	Modal Survey Test: Impact Hammer Test	46
6.1.3	Test Results	51
6.2	Wind turbine EMA	56
6.2.1	Test setup	56
6.2.2	Test results	58
7	Wind turbine OMA results	61
7.1	Wind turbine OMA	61
7.1.1	Test setup	61
7.1.2	Run-up test	62
7.1.3	Constant speed test	64
8	Model Update	68
8.1	Wind turbine tower model update	68
8.1.1	Model update process	68
8.1.2	Model update results	72
8.2	Wind turbine model update	76
9	Conclusions and Future Work	78
9.1	Conclusions	78
9.2	Future Work	79

List of Tables

1.1	Analysed offshore wind farms [15]	4
5.1	Aluminum 6061 material properties	27
5.2	Composite material layers properties	28
5.3	Composite material properties	28
5.4	Mesh modeling: tower and inserts	29
5.5	Mesh modeling: nacelle	30
5.6	Mesh modeling: rotor and hub	30
5.7	Natural frequencies and shapes description	37
5.8	Natural frequencies and shapes description	39
6.1	Accelerometers' Model	48
6.2	Testlab Acquisition Parameters	50
6.3	Natural frequencies and damping ratios	52
6.4	Testlab Acquisition Parameters	57
6.5	Test modal parameters	59
6.6	Off-diagonal elements with high MAC value	59
7.1	Testlab acquisition parameters	62
7.2	Natural frequencies and damping ratios	67
8.1	Aluminum design variables	69
8.2	Motor design variables	69
8.3	Composite material design variables	70
8.4	Modal parameters before update	70
8.5	Model Update Design Variables	72
8.6	Model Update Design Variables	74
8.7	Model Update Results	74
8.8	Wind turbine correlation parameters	76
8.9	Model update design variables	77
8.10	Wind turbine correlation parameters	77

List of Figures

1.1	Total global new wind power installations in 2021 [3]	1
1.2	Projected new wind capacity based on current growth rates [3]	2
1.3	1 st tower bending modes [13],[5]	3
1.4	Flapwise mode of a single blade [13],[5]	3
1.5	Edgewise mode of a single blade [13],[5]	3
1.6	1 st rotor flapwise modes [6]	3
1.7	Field of modern Horizontal Axis Wind Turbines offshore in Denmark [16] .	4
1.8	Typical wind and wave spectra, rotational speed (1P) and blade passing (3P) frequency bands for six commercial turbines and measured natural frequencies of existing wind farms [15].	4
2.1	Stabilization diagram using Polymax for noisy test data [23]	7
2.2	Auto-MAC matrix example	9
3.1	Wind turbines for OMA applications	15
3.2	Comparison of the auto-spectra from measured data and the synthesis using the NExT extracted modal parameters	16
3.3	Modal results for an offshore wind turbine [36]	16
4.1	Dynamic deformation sensors [40]	18
4.2	MPVI comparison for different states [40]	19
4.3	Sketch model of the large flexible spacecraft [39]	20
4.4	Experimental setup for the dynamic testing of the inflatable boom [41] . .	20
4.5	Whirling modes: Healthy case (left) vs Stiffness reduction ($k_1=0.99$) [38] .	21
4.6	Normalized curvatures of the 1st and 2nd mode shapes [38]	22
4.7	Overlay plot of the 6 fundamental tower-foundation mode shapes derived from OMA (continuous line with circular points) and FE model (dashed line with star points) [37]	23
4.8	Time domain and frequency domain comparison of predicted (green) and measured accelerations (red) at the lowest sensor level in FA and SS direction for rotating conditions of the wind turbine. The nominal rotation frequency 1 P at 0.235 Hz (14.1 rpm) and the higher order harmonics up to 15 P are shown in the frequency domain plot for the indicative timestamp [37]	24

4.9	Time history (left), detail time history (middle) and estimated PSD (right) of the FA strain (top) and SS strain (bottom) at level h=19 m LAT for rotating conditions, sensor configuration S_2 . The measured strains are shown in black, the estimated strains obtained from the Kalman filter are shown in gray [44]	25
4.10	Time history (left), detail time history (middle) and estimated PSD (right) of the FA strain (top) and SS strain (bottom) at level h=19 m LAT for rotating conditions, sensor configuration S_2 . The measured strains are shown in black, the estimated strains obtained from the joint input-state estimation algorithm are shown in gray [44]	25
4.11	Time history (left), detail time history (middle) and estimated PSD (right) of the FA strain (top) and SS strain (bottom) at level h=19 m LAT for rotating conditions, sensor configuration S_2 . The measured strains are shown in black, the estimated strains obtained from the modal expansion algorithm are shown in gray [44]	25
5.1	WT Tower CAD	27
5.2	Rotor CAD	27
5.3	Nacelle CAD	27
5.4	Motor CAD	27
5.6	Tower mesh	29
5.7	Top insert mesh	29
5.8	Bottom insert mesh	29
5.9	Nacelle and Motor Mesh	30
5.10	Rotor assembly mesh	30
5.11	Blade mesh	31
5.12	Entire FE model	31
5.13	Nacelle gluing connection	32
5.14	Tower and inserts gluing connection	32
5.15	Tower and inserts 1D connections	33
5.16	Motor 1D connections	33
5.17	Motor CAD modified model	34
5.18	1D connection for the rotor and motor structure	34
5.19	Blade and Rotor connection	34
5.20	Wind turbine base and supporting tripod	35
5.21	1 st Constraint configuration	35
5.22	Final Constraint Configuration	36
5.23	Modal shapes of the wind turbine tower structure (1,2,3,4)	36
5.24	Modal shapes of the wind turbine tower structure (5,6,7,8)	37
5.25	Modal shapes of the wind turbine tower structure (9,10,11,12)	37
5.26	Modal shapes of the wind turbine tower structure (13,14,15,16)	38
5.27	Modal shapes of the wind turbine structure (1,2,3)	40
5.28	Modal shapes of the wind turbine structure (4,5,6)	40
5.29	Modal shapes of the wind turbine structure (7,8)	41
5.30	Modal shapes of the wind turbine structure (9,10)	41

6.1	Triaxial Accelerometers Configuration	44
6.2	MAC matrix - Min-MAC algorithm	45
6.3	DPR algorithm results for a single exciter point	46
6.4	Exciter Selection	47
6.5	Accelerometers	48
6.6	Impact Hammer	49
6.7	Input Profile	49
6.8	Response Profile	49
6.9	Simcenter SCADAS Mobile	50
6.10	Testlab Geometry	51
6.11	FRF and Coherence of 4 driving points	51
6.12	Stabilization Diagrams for single input configurations	53
6.13	Stabilization Diagram XZ Input	53
6.14	Auto-MAC XZ Input	54
6.15	Synthesized and Measured FRFs	54
6.16	Modal shapes of the wind turbine tower structure (1,2,3,4,5)	55
6.17	Modal shapes of the wind turbine tower structure (6,7,8,9,10)	55
6.18	Modal shapes of the wind turbine tower structure (11,12,13,14,15,16)	55
6.19	Wind turbine blades' sensor configuration	56
6.20	Tower sensor configuration	56
6.21	Wind turbine measurement set-up	57
6.22	Input Profile Frequency Domain	57
6.23	FRF and coherence of the three driving points	58
6.24	Stabilization diagram	58
6.25	Driving points	59
6.26	Auto-MAC matrix	60
6.27	Modal shapes of the wind turbine (1,2,3,4,5)	60
6.28	Modal shapes of the wind turbine(6,7,8,9,10)	60
7.1	Test set-up	62
7.2	Run-up test results	63
7.3	Run-up colormap - restricted bandwidth	63
7.4	Stabilization diagram (10 rpm)	64
7.5	Stabilization diagram (10 rpm) - restricted bandwidth	65
7.6	Stabilization diagram (20 rpm)	65
7.7	Stabilization diagram (30 rpm)	65
7.8	Autopower comparison 10, 20, 30 rpm	66
7.9	Autopower comparison 20, 30 rpm	66
7.10	Whirling modes' frequency - test speed	67
8.1	MAC matrices before and after the motor change	69
8.2	MAC and frequency error comparison for the diagonal values before and after the update	73
8.3	MAC matrix comparison before and after the update	73
8.4	Modal shapes of the wind turbine tower structure (1,2,3,4)	74

8.5	Modal shapes of the wind turbine tower structure (5,6,7,8)	75
8.6	Modal shapes of the wind turbine tower structure (9,10,11,12)	75
8.7	Modal shapes of the wind turbine tower structure (13,14,15,16)	75
8.8	Wind turbine correlation	76

Chapter 1

Introduction

1.1 Framework and Motivation

Wind power generation has become a focal point in the renewable energy field due to its clean and sustainable nature [1]. Its minimal impact on the ecological environment and the maturity of its manufacturing technology contributed to a rise of the installed capacity of wind turbines, as a strategic response to the energy crisis [2].

The Global Wind Report [3] confirms the increasing expansion of wind power, with 93.6 GW of new installations in late 2021 (Fig. 1.1), which was the second-best year for the wind industry. This growth takes global cumulative wind power capacity to 837 GW, with a growth rate of 12%. A record was also established for the onshore installation in Europe, Latin America and Africa and the Middle East, where there was an increase of 19%, 27% and 120%, respectively.

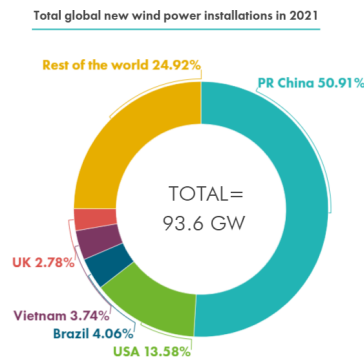


Figure 1.1: Total global new wind power installations in 2021 [3]

Nevertheless, despite the increasing expansion of wind power, reaching the net zero goal by 2050 will require a quadrupling of the wind energy supply. To give an example, in 2021, Germany, Italy and Poland added only 10 GW of the 20 GW of new onshore capacity, while offshore wind power capacity reached 18.1 GW in Europe, which is still an inadequate volume. In fact, the EU needs 32 GW of new wind capacity each year until 2030 to achieve its carbon neutrality target by 2050. Thus, the growth of wind energy should increase even faster to fulfill a secure global energy transition [3].

The majority of the wind energy produced worldwide comes from three-bladed horizontal-axis wind turbines. Blades complexity and tower flexibility are fundamental aspects of wind turbines. Hence, accurate structural characterization of these components is essential for cost

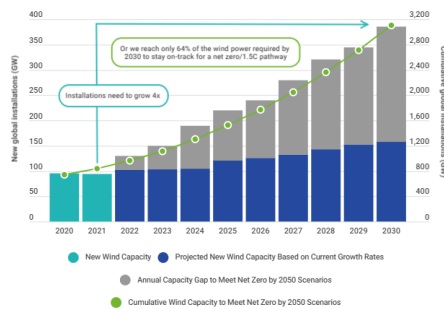


Figure 1.2: Projected new wind capacity based on current growth rates [3]

reduction and the prevention of possible structural damage. The objective of reducing costs has led to an increase in wind turbine size, resulting in longer blades and taller towers that may experience excessive vibration levels [1], [4].

A comprehensive study of wind turbine modal characteristics is necessary for ensuring structural safety operation and developing effective structural health monitoring (SHM) algorithms. Modal identification and SHM algorithms can enhance wind turbine maintenance, prevent possible damages, and reduce the risk of failure, ultimately improving wind turbine reliability [2].

Structural vibrations in wind turbine are influenced by both the tower structure and the blades. The deformation of the blades dominates the structural response of wind turbines, with in-plane and out-of-plane vibrations, typically classified as edgewise and flapwise vibrations, respectively (Fig.1.4,1.5) [5]. Wind turbine blades also exhibit high-order torsional deformations, and some blade modes are characterized by a combination of different deformation types.

For each mode of a single blade, there are three modes of the rotor, which is defined as the assembly of the blades attached to the hub. These rotor modes consist of one symmetric mode, where all blades are symmetrically deformed, and two asymmetric modes, where two blades deflect contrary to the other blade (Fig. 1.6) [6]. Furthermore, blade modes typically show a coupling with the nacelle and rotor deformation, resulting in flapwise or edgewise modes combined with yawing or pitching motions.

Mode coupling investigation can improve blade aeroelastic simulation [7], including blade flutter prediction [8], and enable the development of more precise SHM algorithms,[4], [9].

For what concerns the supporting structure, the tower is the most critical component regarding structural safety of the wind turbine and it represents beyond 20% of the total wind turbine cost [10]. The tower structure is characterized by various mode shapes, from low-order bending modes, to high-order bending modes and torsional modes. However, the interest mode for the wind turbine dynamic characterization is the first bending in both the fore-aft and side-side direction (Fig. 1.3). To avoid resonance, this first mode should not fall in the frequency range of excitation of the turbine, where the lower limit (1P) is the operating frequency, that corresponds with the rotational frequency of the rotor, increased of 10%, while the upper limit (N_bP where N_b is the number of blades) is the blade passing frequency, decreased of 15% [10], [11]. The tower structure can be classified in terms of performance dynamic in three designs: soft-soft, when the first bending natural frequency of the tower is lower than the 1P, soft-stiff, if the natural frequency falls within the 1P and the N_bP , stiff-stiff, if the natural frequency lies higher than N_bP . The optimal design in terms of safety and cost-effectiveness is the soft-stiff one. The soft-soft tower design is deemed too flexible and more susceptible to resonant problems, in contrast the stiff-stiff is considered too rigid [5], [10], [12]. Notably, resonant

problems will be avoided when the tower design belongs to the stiff-stiff region, concerning the soft-stiff design, the resonance does happen and the adequate controller is necessary in order to avoid the corresponding resonant susceptible area of the tower structure [10].



Figure 1.3: 1st tower bending modes [13],[5]

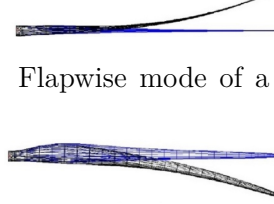


Figure 1.4: Flapwise mode of a single blade [13],[5]

Figure 1.5: Edgewise mode of a single blade [13],[5]



Figure 1.6: 1st rotor flapwise modes [6]

Wind turbines experience deformations and rigid body motions as a result of dynamic and gravitational loads that constantly excite the system. These deformations can be divided into quasi-static and dynamic responses, which are characterized by the previously described mode shapes [10]. Wind gusts, rotor imbalances (1P), rotor blade passing (N_bP) and its harmonics, and wave action (for offshore wind turbines) are examples of dynamic loads, which can take place multiple times during the system's lifetime. The frequency range of these dynamic loads is usually below 3 Hz, very close to the main natural frequencies of a large wind turbine. Therefore, precise alignment of the vibrational response of the wind turbine is required to avoid resonances [5].

Numerous works have examined the wind turbine design and how to prevent resonances due to the coincidence of the first tower bending frequency and the excitation loads frequencies. [5], [14], [15]. For instance, Arany, et al. [15], compared the measured natural frequencies of turbines of existing wind farms in Europe with the typical wind and wave power spectral densities (PSDs) for offshore sites. These PSDs represent the frequency content of the dynamic loads from wind gusts and wave action.

The plot in Fig. 1.8 also illustrates the first order of rotor speed (1P) and the blade passing frequency (3P for a three-bladed wind turbine) for commercial wind turbines of different capacities (2–8 MW), listed in Table 1.1. The plot indicates that all the examined wind turbines have been designed with a soft-stiff configuration, where the first tower bending natural frequency is located between 1P and 3P. Additionally, the graph shows a trend in the desired natural frequencies of heavier wind turbines, which tend to be closer to the excitation frequencies of wind and waves, making these structures even more susceptible to dynamic loading [15].

Numerical and experimental methods are required to characterize the dynamic properties and identify the modal parameters of wind turbines for the purposes discussed until now.

While Finite Element (FE) models can estimate the natural frequencies and the numerical



Figure 1.7: Field of modern Horizontal Axis Wind Turbines offshore in Denmark [16]

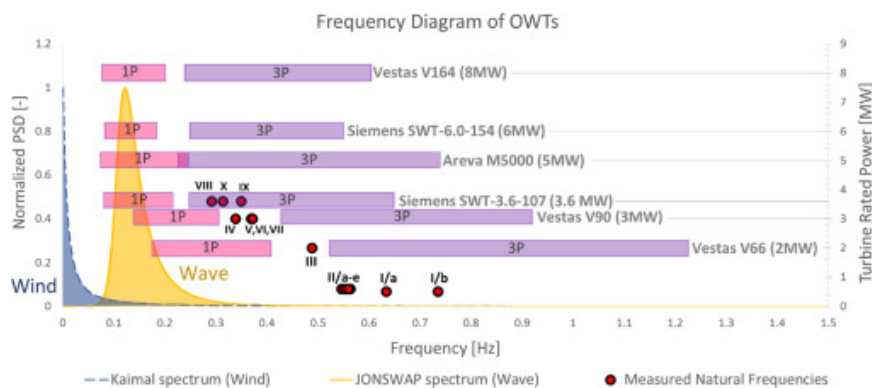


Figure 1.8: Typical wind and wave spectra, rotational speed (1P) and blade passing (3P) frequency bands for six commercial turbines and measured natural frequencies of existing wind farms [15].

Table 1.1: Analysed offshore wind farms [15]

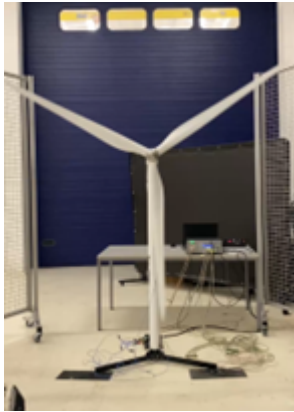
No.	Wind farm name and location	Turbine type and rated power
I	Lely Offshore Wind Farm (Netherlands)	NedWind 40/500 2-bladed 500 kW
II	Irene Vorrink Offshore Wind Farm (Netherlands)	Nordtank NTK600/43 600 kW
III	Blyth Offshore Wind Farm (UK)	Vestas V66 2 MW
IV	Kentish Flats Offshore Wind Farm (UK)	Vestas V90 3 MW
V	Barrow Offshore Wind Farm (UK)	Vestas V90 3 MW
VI	Thanet Offshore Wind Farm (UK)	Vestas V90 3 MW
VII	Belwind 1 Offshore Wind Farm (Belgium)	Vestas V90 3 MW
VIII	Burbo Bank Offshore Wind Farm (UK)	Vestas V90 3 MW
IX	Walney 1 Offshore Wind Farm (UK)	Siemens SWT-3.6-107 3.6 MW
X	Gunfleet Sands Offshore Wind Farm (UK)	Siemens SWT-3.6-107 3.6 MW

mode shapes with a desired FE discretization defined by the mesh density, experimental techniques are limited by the number of accelerometers, which have mass loading effect on the structure to take into account. Especially for high-order modes, a large number of accelerometers is required. The mode order is then limited by the number of accelerometers: a large number of sensor could obtain complex curvature mode shapes, but it requires high test capacity, and it would not accurately measure the system dynamics due to the mass loading, on the contrary, a small number would not have the mass loading problem, but complex mode shapes are not detected due to the geometrically sparse sensors. Thus, accelerometers are only suitable for low-order bending modes, which do not present complex curvature [4].

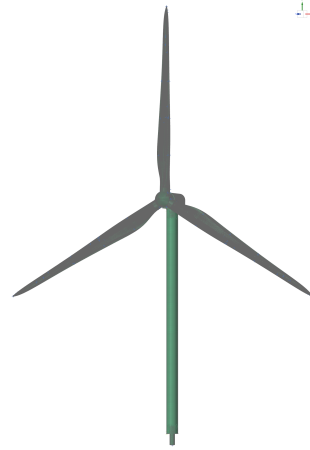
The numerical approach does not present the discretization problem due to the limited number of measurement points, considering that the mesh density can be highly fine. However, the definition of a solid FE model presents several issues. Firstly, the numerical model must

represent with great accuracy the structure design parameters, such as the material properties and the design geometry. Regarding the material, the main issues are related to the composite used for the blades, made of different materials with multiple layer thicknesses and geometric configurations. Besides, the connections between different parts and the boundary conditions also require rigorous modeling. The boundary conditions strongly affect the first natural frequencies of the wind turbine. Moreover, even if the material and the connections are replicated precisely, the model can still present errors compared to the experimental results, caused by uncertainties in the material properties due to tolerances in the manufacturing process [4]. For this reason, the numerical results must be correlated with the experimental ones to validate the model and be confident on the accuracy of its outcomes. Therefore, experimentally derived data can be used to update numerical models, implementing the basis for a dynamic virtualization process. The dynamic virtualization process can continue, once the numerical model has been validated, when combined data-driven and physics-based SHM strategies can be implemented for monitoring the turbine during its operational life and preventing potential failures and any degradation in structural integrity.

This work reports on the dynamic virtualization process of the small-scale horizontal axis wind turbine in Fig. 1.9a. The primary objective of this study consists in integrating experimental and numerical techniques for a comprehensive analysis of the small-scale wind turbine. To accomplish this task, a numerical model is developed and validated using mathematical modeling techniques and simulation tools to replicate the wind turbine dynamic response (Chapter 5). Experimental Modal Analysis (EMA) is exploited to extract modal parameters (Chapter 6), which are then employed for FE model update (Chapter 8). Operational measurements are conducted to evaluate the system dynamic behavior in rotating conditions. In this sense, Operational Modal Analysis (OMA) is exploited to extract the wind turbine modal parameters in operation (Chapter 7). The outcome of the presented study builds a solid baseline for future implementation of hybrid SHM strategies, i.e., involving combination of pre-validated mechanistic models and data-driven approaches.



(a) Small-scale wind turbine



(b) Wind turbine FE model

Chapter 2

Experimental Modal Analysis: an Overview

EMA is a key technology in structural dynamics that aims to investigate the dynamic properties of a system, resulting in the estimation of frequency, damping and modal shapes information for the structure from Frequency Response Functions (FRFs) or time responses.

This modal testing technique has been growing since the 1980s and it has become widely used, owing to the availability of user-friendly software packages and the simplicity of modal test setups [17]. The evolution of EMA has made this technique a remarkable tool for industries seeking to understand and mitigate noise, vibration and potential failures in their products. Even though great improvements have been reached, the technique still requires accurate measurements, proper excitation locations, and proper modal estimation algorithms to succeed and achieve a good accuracy for the modal survey results [18].

2.1 Modal analysis identification techniques

Over the course of several decades, the techniques employed in modal analysis identification have undergone significant advancements, progressing from simple degree of freedom (SDOF) methods to more sophisticated multiple degree of freedom (MDOF) approaches to analyze data from multiple input excitation and multiple output responses simultaneously. Another main development is the introduction of operating modal analysis approaches alongside the traditional ones, enabling the estimation of more accurate parameters from better acquired data and consequently the definition of precise modal model [17].

SDOF methods are the simplest ones, they estimate the parameters from the FRFs one mode at a time. These methods are often inappropriate when the system presents extremely light damping or closely-coupled modes. In the first case, it is difficult to acquire measurements at resonance, while systems with closely-coupled modes are characterized by closely spaced natural frequencies or relatively heavy damping or both.

MDOF methods allow the extraction of several modes at the same time, making them more adequate for the modal parameter estimation of these complex systems. Moreover, a correct modal analysis requires also a method that analyses several curves simultaneously [19].

The modal parameter extraction methods can be divided in two main groups: time-domain based methods and frequency-domain based methods. Initially, MDOF methods used time-domain data. This group of methods is known as Complex Exponential Methods.

These algorithms study the Impulse Response Function (IRF), which is the inverse Fourier transform of the FRF. Any IRF can be defined as a series of complex exponential components

2.2 Leakage and windowing

For EMA purposes, various types of input signals can be used, including impact impulses, random impulses, pseudo-random impulses, and burst-random signals. The choice of input signal depends on the instrument used and the desired properties of the system under study. However, if the input signal is not periodic during the sampling window of the test, the frequency spectrum can become smeared, resulting in inaccuracies and loss of information. This phenomenon is known as leakage. To mitigate leakage, windowing techniques are employed. A periodic signal is a signal that is completely contained in the sampling window or a cyclic signal that completes an integer number of cycles in the sampling window. For example, if the impulse due to an impact test decays to zero before the end of the sampling window, then no leakage occurs. Otherwise, the signal is not periodic and an exponential window can be applied to reduce the leakage. Windowing forces the signal to begin and end in zero, making it periodic [24].

2.3 Model correlation theory

EMA results can be used to correlate with a FE model, thereby improving the accuracy of the numerical model. This involves comparing the natural frequencies and mode shapes obtained from the experimental and numerical analyses. Natural frequencies can be directly compared between the two models to verify their agreement, while mode shapes are correlated by means of the Modal Assurance Criterion (MAC).

The natural frequencies from the EMA can be compared to the numerical results by means of the frequency error formula:

$$\epsilon_f = \frac{f_{n,num} - f_{n,exp}}{f_{n,num}} \times 100. \quad (2.1)$$

The frequency error should be kept below 10%, also lower for the first natural frequencies. The MAC is a measure of similarity between two mode shapes and provides the degree of agreement between experimental and numerical mode shapes. The mode shapes can be real or complex. The MAC value is between zero and one.

The MAC number is defined as a scalar constant expressing the degree of consistency between the numerical (work) mode shape Ψ_A and the experimentally-measured (reference) mode shape Ψ_X as follows:

$$MAC(A, X) = \frac{\left| \sum_{j=1}^N \Psi_{Xj} \Psi_{Aj}^* \right|^2}{\sum_{j=1}^N \Psi_{Xj} \Psi_{Xj}^* \sum_{j=1}^N \Psi_{Aj} \Psi_{Aj}^*} \quad (2.2)$$

where N is the number of common work and reference mode shape components and the superscript $*$ indicates the complex conjugate value.

For each mode shape matrix $[\Psi_A]$ and $[\Psi_X]$ of a given data set, there are $L_A \times L_X$ MAC numbers. L_A is the number of mode shapes in $[\Psi_A]$ and L_X is the number of mode shapes in $[\Psi_X]$. If two mode shapes are identical or differ by a simple scalar multiplier, they correlate perfectly and the diagonal MAC value is equal to 1.

After conducting a modal test, the resulting mode shapes can be compared within the same data set, which is known as Auto-MAC (Fig. 2.2). The Auto-MAC matrix is always a square matrix with L_A^2 elements, where L_A is the number of modes identified from the experimental data. The diagonal elements of the Auto-MAC matrix are always equal to one, as they correspond to the correlation between a mode shape and itself. On the other hand, the off-diagonal elements of the Auto-MAC matrix should be close to zero. These elements represent the correlation between different mode shapes and provide information on the degree of similarity

between them. If the off-diagonal elements are high, it suggests that the sensor configuration may be incorrect, which can lead to the merging of two modes or the inability to distinguish between similar modes due to insufficient accelerometers on the structure. It is important to note that interpreting Auto-MAC results requires careful consideration of the measurement setup and data quality to ensure reliable and meaningful results [24].

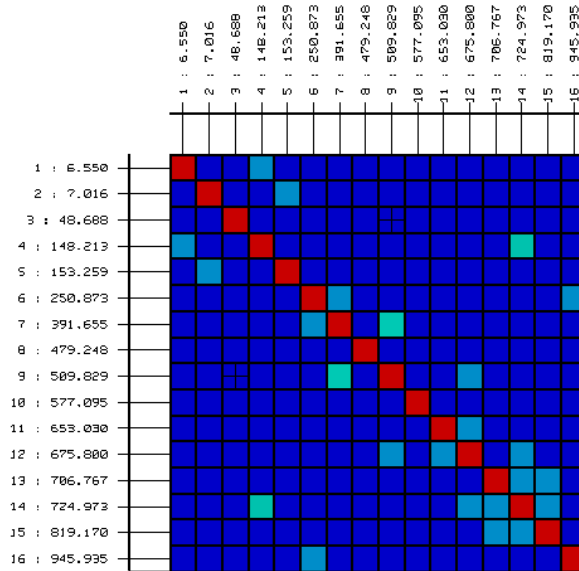


Figure 2.2: Auto-MAC matrix example

Chapter 3

Operational Modal Analysis: an Overview

The requirement to assess the dynamic behavior of systems during their operational lifespan has spurred the development of a novel modal analysis technique known as Operational Modal Analysis (OMA). Also referred to as "output-only modal analysis" the principle of this method is the investigation of modal properties using only the response measurements of structures under operational conditions, wherein input forces cannot be directly measured.

3.1 Theoretical basis

The development of OMA was a crucial advancement in the field of structural dynamics. The main assumptions for this method are: the system must be Linear Time Invariant (LTI) and the excitation forces must exhibit a flat white noise spectrum within the relevant frequency band. The accuracy of modal parameter estimates using OMA improves as the system more closely fulfills these assumptions [25].

One of the key steps in the development of this technique was identifying a function derived from operational data that would exhibit a clear relationship with, and dependence on, the modal parameters of the structure. The selected function was the cross-correlation function between responses without a measurement of the input force [16]. In this section, the process by which the relationship between the cross-correlation function and the modal parameters was developed will be outlined.

The modal identification method for OMA are similar to that used for EMA (2). However, OMA methods are based on auto- and cross-correlations in the time domain and auto- and cross-spectra in the frequency domain, whereas EMA methods use IRFs and FRFs.

Under the assumption of white noise input, the output spectra can be modelled in a very similar way as the FRF. The FRF matrix $H(\omega)$ is expressed in Equation (3.1) as a function of the modal parameters.

$$[H(\omega)] = \sum_{i=1}^n \frac{v_i \langle l_i^T \rangle}{j\omega - \lambda_i} + \frac{v_i^* \langle l_i^H \rangle}{j\omega - \lambda_i^*}. \quad (3.1)$$

In Equation (3.1), n is the number of complex conjugated mode pairs, $*$ denotes the complex conjugate of a matrix, H represents the complex conjugate transpose (Hermitian) of a matrix, v_i are the mode shapes and l_i denotes the modal participation factors. λ_i represents the poles, which exist as complex conjugate pairs and are related to the eigenfrequencies ω_i and damping

ratios χ_i as shown in Equation (3.2).

$$\lambda_i, \lambda_i^* = -\chi_i \omega_i \pm i\sqrt{1 - \chi_i^2} \omega_i. \quad (3.2)$$

The relationship between the auto- and cross-power spectral density matrix between the outputs S_{yy} and the the auto- and cross power spectral density matrix S_{uu} between the input forces, for stationary stochastic processes, is given in Equation 3.3.

$$[S_{yy}(\omega)] = [H(\omega)][S_{uu}][H(\omega)]^H \quad (3.3)$$

In OMA the input forces are unknown. In fact, the main assumption is that the input forces can be approximated as white noise inputs, thus the input matrix is not frequency dependent and is a constant matrix.

The modal decomposition of the output spectrum matrix is obtained by combining Equation 3.1 and 3.3 in Equation 3.4.

$$[S_{yy}(\omega)] = \sum_{i=1}^n \frac{v_i \langle g_i \rangle}{j\omega - \lambda_i} + \frac{v_i^* \langle g_i^* \rangle}{j\omega - \lambda_i^*} + \frac{\langle g_i \rangle v_i}{-j\omega - \lambda_i} + \frac{\langle g_i^* \rangle v_i^*}{-j\omega - \lambda_i^*} \quad (3.4)$$

where g_i denotes the operational reference factors, which corresponds to the modal participation factors for OMA. Their physical meaning is complex to understand, since they are function of all modal parameters of the system and the constant input spectrum matrix.

The last equation is the fundamental equation for most of the frequency domain operational modal identification techniques and the goal of OMA is to identify the right hand side terms of this equation based on measured output data pre-processed into output spectra [26].

3.2 PolyMax method

Frequency-domain Modal Analysis techniques can be applied to determine the modal parameters in both EMA and OMA. The primary distinction between these two methods is the function employed for estimating the modal parameters, where the FRF is utilized for EMA, while the output spectra for OMA. Pre-processing of the output data is required in OMA, and the resulting half-spectra equation is comparable to the FRF formulation. This allows for the same modal parameter estimation techniques to be utilized in both EMA and OMA.

Power spectra are the Fourier transforms of the correlation vectors. Output data is pre-processed into output spectra by means of non-parametric spectrum estimate, such as the weighted averaged periodogram and weighted correlogram. The term weighted refers to the application of a classical window, such as Hanning or Hamming, to reduce leakage.

In the context of modal analysis, the advantageous non-parametric spectrum estimate is the weighed correlogram. This method evaluates the output spectra from the Discrete Fourier Transform (DFT) of the correlation matrix (Equation 3.5):

$$R_i = \frac{1}{N} \sum_{k=0}^{N-1} y_{k+1} y_k^T. \quad (3.5)$$

The output spectra is obtained by inserting Equation 3.5 in Equation 3.6:

$$S_{yy}(\omega) = \sum_{k=-L}^L w_k R_k \exp(-j\omega k \Delta t) \quad (3.6)$$

where L is the maximum number of time lags at which the correlations are estimated, which is usually smaller than the number of data samples to avoid the greater statistical variance associated with the higher lags of the correlation estimates.

The first advantage of this technique in the modal analysis context is the possibility to compute the half spectra by considering only the correlations having a positive time lag. The half spectra is shown in Equation 3.7.

$$S_{yy}^+(\omega) = \frac{\omega_0 R_0}{2} + \sum_{k=1}^L w_k R_k \exp(-j\omega k \Delta t). \quad (3.7)$$

The relationship with the full spectra is:

$$S_{yy}(\omega) = S_{yy}^+(\omega) + S_{yy}^+(\omega)^H. \quad (3.8)$$

The half spectra is sufficient for performing the modal analysis step and its modal decomposition consists only of the first two terms of Equation 3.4.

$$[S_{yy}^+(j\omega)] = \sum_{i=1}^n \frac{v_i \langle g_i \rangle}{j\omega - \lambda_i} + \frac{v_i^* \langle g_i^* \rangle}{j\omega - \lambda_i^*}. \quad (3.9)$$

By using the half spectra, models of lower order can be fitted without affecting the quality. Another advantage is that the output correlations are equivalent to impulse responses under the white noise assumption. Thus, it is suggested to apply an exponential window to the correlations before computing the DFT, to reduce leakage and ensure the estimation of correct poles. This is not valid for other window types [26].

Once the output spectra is computed, the poly-reference Least Squares Complex Frequency method (p-LSCF), or PolyMax, can be implemented. The implementation is the same for EMA and OMA as previously stated. The first step is to fit a modal model through a modal parameter estimation step. The PolyMAX method identifies a right matrix-fraction model, which is assumed to represent the measured FRFs for EMA or the half spectrum for OMA. In the PolyMax method a z-domain is used, which is a frequency-domain derived from a discrete-time signal. The right matrix-fraction description for the FRF is (Equation 3.10):

$$[H(\omega)] = [B(\omega)][A(\omega)]^{-1} \quad (3.10)$$

where $B(\omega)$ is the numerator matrix polynomial and $A(\omega)$ is the denominator matrix polynomial, leading to the following formulation for the right matrix-fraction model:

$$[H(\omega)] = \sum_{r=0}^p \Omega_r(\omega) [\beta_{or}] \left(\sum_{r=0}^p \Omega_r(\omega) [\alpha_r] \right)^{-1}. \quad (3.11)$$

In Equation 3.11, p is the order of the polynomials, β_{or} are the numerator matrix polynomial coefficients, α_r are the denominator ones.

Regarding the Operational PolyMax, the right matrix-fraction model representing the measured half spectrum matrix is expressed in Equation 3.12.

$$S_{yy}^+(\omega) = \sum_{r=0}^p z^r [\beta_r] \left(\sum_{r=0}^p z^r [\alpha_r] \right)^{-1}. \quad (3.12)$$

The unknown numerator and denominator matrix polynomial coefficients, β_{or} and α_r , can be now estimated after the linearization of the equation in a least-squares sense and by means of a minimization of the difference between the FRF or the half spectrum obtained from

the measured one and the theoretical one computed from 3.11 and 3.12, respectively. The complete mathematical formulation is reported in [26], [27].

The poles λ_i and the modal participation factors $\langle l_i^T \rangle$ (in case of FRFs) or the operational reference factors $\langle g_i \rangle$ (in case of spectra) can be found from the denominator coefficients α_r by computing the eigenvalue decomposition of their companion matrix. The PolyMax stabilization diagram is constructed with the least squares problem for the maximum model order p_{max} . It is suggested to increase significantly the model order, when estimating the modal parameters. Then, the true physical poles will be discernible from the spurious numerical ones in the stabilization diagram. Indeed, the stable poles will be the ones which when compared to a lower-order model exhibit differences within pre-set limits. The spurious poles will not be stable during this process and can be excluded easily from the modal parameter estimation. The final step of the estimation process is the calculation of the mode shapes from Equation 3.13 (in case of FRFs) and Equation 3.14 (in case of spectra).

$$[H(\omega)] = \sum_{i=1}^n \frac{v_i \langle l_i^T \rangle}{j\omega - \lambda_i} + \frac{v_i^* \langle l_i^H \rangle}{j\omega - \lambda_i^*} + \frac{LR}{(j\omega)^2} + UR \quad (3.13)$$

$$[S_{yy}^+(\omega)] = \sum_{i=1}^n \frac{v_i \langle g_i \rangle}{j\omega - \lambda_i} + \frac{v_i^* \langle g_i^* \rangle}{j\omega - \lambda_i^*} + \frac{LR}{j\omega} + j\omega UR \quad (3.14)$$

LU and UR are the lower and upper residuals, needed to model the influence of the out-of-band modes in the considered frequency band. The operational residuals are different from the usual residual in case of FRFs. Their format is reported in [26] for FRFs, classical full spectra and half spectra. The unknowns, mode shapes v_i and residuals, are computed by solving Equation 3.13 or Equation 3.14 in a least squares sense [26]–[28].

3.3 OMA benefits and drawbacks

The advent of OMA has increased the reliability of modal parameter identification in structural dynamics. OMA has several benefits compared to EMA, which are:

1. enables the dynamic characterization of a structure in its real-life environment and operational conditions, while EMA is conducted in laboratory conditions that may not reflect reality;
2. OMA is carried out using ambient excitation, while EMA requires artificial excitation, which can be challenging to apply properly;
3. ambient excitation, which causes problems during EMA, can be used as input for OMA.
4. lastly, OMA is suitable for continuous monitoring of systems undergoing ambient noise.

However, the OMA approach presents three primary limitations. First, it is unable to estimate all modal parameters, leaving the mode shapes unscaled. Second, if the input signal does not meet the assumption of white noise, there is a risk of inadequate estimation of modal parameters. This is because deviations from the assumption of white noise can lead to the appearance of peaks in the input and output spectra, which may be mistakenly identified as structural modes. Third, if the ambient excitation does not adequately excite the structure, noise in the output data may lead to inaccurate identification of modal parameters.

Additionally, rotating machines in constant rotational speed conditions (stationary operations) may exhibit harmonic components in the measured spectra, which can appear as sharp peaks

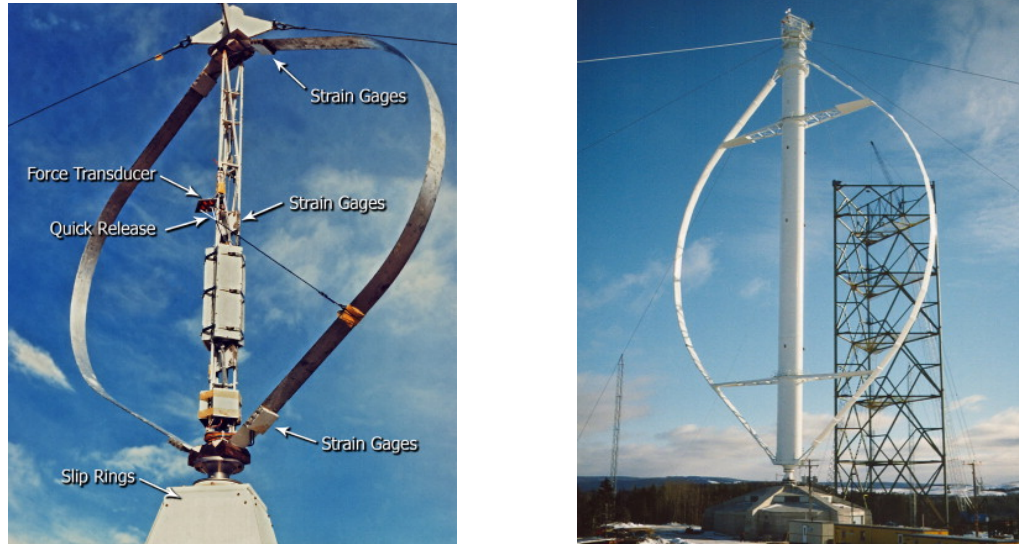
at fixed frequency and potentially influence the dynamic properties nearby. Besides, in transient conditions, such as run-up/coast-down events, these harmonics may sweep through a certain frequency band and their contribution in the cross-correlation function are averaged. Although the resulting spectra is quite flat, the presence of these harmonics can result in peaks appearing at the corresponding frequency where the orders end at maximum rotational speed, or due to other rotational speeds at which the machine rotates for longer periods during manually-controlled run-up and coast-down events. All these peaks may be identified erroneously as natural frequencies and they could affect the dynamics in their close proximity. This phenomena has been called "end-of-order" effect [28]. Therefore, even though OMA is a widely applied technique, its application to rotating machines, like wind turbines, is particularly complex, since their operation violates many of the underlying assumptions of OMA [25]. However, if the rotor has an approximately constant angular speed, then the wind turbine can be approximated as Linear Time Periodic (LTP) and alternative methods such as the Coleman theory may be used to characterize its dynamic behavior. Coleman theory involves a transformation to convert the rotating degrees of freedom into a non-rotating frame by means of the Multi-Blade Coordinate (MBC) transformation. Di Lorenzo, et al. [29] applied the transformation on simulated data and demonstrated the feasibility of this method.

3.4 Wind Turbine OMA Historical background

The origin of OMA lies in the Natural Excitation Technique (NExT), which was developed as an alternative to the traditional step-relaxation excitation method for wind turbine testing. Prior to the development of NExT, operational wind turbine testing was conducted using a quick-release device to excite the structure. Carne, et al. [16] explained this method, that was performed on a Sandia 2-m vertical axis wind turbine (VAWT) built for research purposes (Fig. 3.1a). The test included measuring the structural response in parked condition and at seven different operating speeds up to 800 rpm. For the test in parked condition the traditional technique was employed, via impact excitation and accelerometers to measure the output. Regarding the tests in operational conditions, the main issue was related to the input excitation. The solution was found in a quick-release device attached to the tower that could rotate with the tower. To excite the wind turbine with a measurable input, a pre-load was established between the tower and one of the blades through the device, which would create a step-relaxation input when suddenly released during rotation. However, this procedure was extremely time consuming as the device required to be reloaded for every input, thus the turbine had to be brought down to parked condition and then again up to its rotation speed [16].

In 1986 a new method, developed as an alternative to step-relaxation excitation, was performed on the 110-meter tall Éole turbine (Fig. 3.1b). It was the first OMA conducted on a wind turbine. At the time the technique was known as wind excited or Natural Excitation Testing (NExT), the term OMA was yet to be invented. The NExT method used wind-induced natural excitation, which was faster than step-relaxation excitation as there was no need to load the device between each test. The OMA algorithm employed measured autospectral and cross-spectral densities of all channels in a data set. Assuming real mode shapes, the amplitudes and signs of the shape components were obtained from the cross-spectral densities, and the shape components were normalized via the reference channels. Natural frequencies for the modes were estimated from the auto-spectral densities, although damping was not estimated. The test results validated that wind excitation is a very reliable alternative for large wind turbine testing, reducing testing time and cost when compared to step-relaxation testing [16]. Carne, et al. [16] provided a detailed description of the NExT (OMA) verification process using

simulated data, conventional modal test results, auto-spectrum synthesis in "The inception of OMA in the development of modal testing technology for wind turbines". Additionally, the results for a rotating vertical axis wind turbine (VAWT) and a horizontal axis wind turbine (HAWT) using NExT are briefly presented.



(a) Sandia 2-m VAWT with instrumentation [16] (b) The 110-m tall Éole wind turbine [16]

Figure 3.1: Wind turbines for OMA applications

In its work titled "Extraction of modal parameters from an operating HAWT using the Natural Excitation Technique (NExT)", James, [30] conducted an OMA on a Northern Power Systems 100-kW two-bladed upwind horizontal axis wind turbine (HAWT) with a teetering rotor. The instrumentation consisted in a strain gauge set measuring the flapwise bending and a second set measuring the edgewise bending at the base of the first blade, plus a third one measuring the flapwise bending on the second blade. The data were collected from different wind speeds, ranging from 4.5 m/s up to 13 m/s, while the turbine was rotating at 72 rpm.

One notable finding was a harmonic response attributed to rotation, as evidenced by the discrepancy observed in damping ratio between the apparent numerical damping of the harmonics, which was below 1%, and the actual damping of the true modes, which were all recorded above 1%. This discrepancy, along with the presence of frequencies that were multiples of the rotation speed, provided a clear indicator of the harmonic response.

The comparison between the auto-spectra of the measured data and the synthesis based on the NExT extracted parameters for the root flapwise sensor is illustrated in Fig. 3.2. Although the first edgewise (1E) mode is not clearly discernible in the flapwise sensor, the second edgewise mode (2E) is well depicted. A small peak is visible at 1.5 Hz, but could not be detected, that may be a first tower mode. Furthermore, the third edgewise (3E) and the second flapwise (2F) modes also appear among the harmonic responses.

Other OMA applications for modal parameter estimation on wind turbines can be found in literature. White [31] and Manzato, et al. [32] performed an OMA on the Micon 65/13M on-land wind turbine. The OMA results corresponded with the ones obtained from a previous hammer test. In the second part of the paper, Manzato, et al., analyzed the operating results with a particular attention on the harmonic and periodic components appearing in the measured data and related to the blade rotation. The majority of the identified modes corresponded to harmonic components, thus different harmonic removal techniques were applied

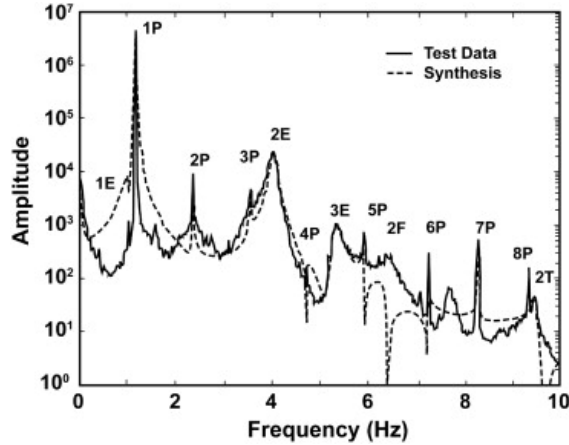
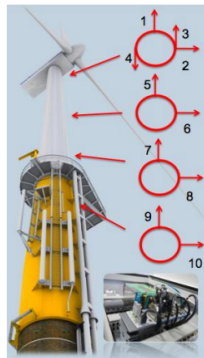
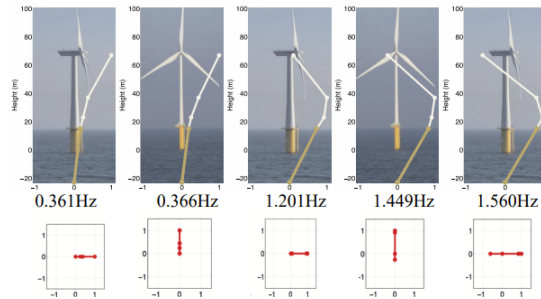


Figure 3.2: Comparison of the auto-spectra from measured data and the synthesis using the NExT extracted modal parameters

to the data to investigate their performance. The reliability of OMA was also investigated by Tcherniak [33] on the Vestas 225 kW V27 wind turbine and Chauhan [34] on the 3 MW ALSTOM wind turbine. These applications are all related to on-land wind turbines, but also results for offshore wind turbines are available. Devriendt, et al. [35] and De Sitter, et al [36] performed measurement campaigns on a Vestas V90 3 MW wind turbine placed on a monopile foundation structure, from the Belwind wind farm in the North Sea, 46 km off the Belgian coast (Fig. 3.3a).



(a) Vestas V90 3 MW



(b) Five dominant identified tower mode shapes

Figure 3.3: Modal results for an offshore wind turbine [36]

The structure instrumented in both campaigns is the tower, the results obtained from the two works proved that the method is very efficient in the identification and tracking of the wind turbine's mode of interest related to the tower structure (fore-aft and side-side bending, Fig. 3.3b). The main issue in the implementation of OMA on offshore wind turbines is the impossibility to perform direct measurements on most of the fatigue sensitive spots due to the inaccessibility of these regions for traditional sensors [37]. This obstacle and the possible solutions to overcome it will be discussed in chapter 4.

Chapter 4

Structural Health Monitoring

In industrial applications, the maintenance of machinery represents a significant portion of the total cost. Early detection of damage is therefore crucial to avoid catastrophic failures that could compromise the structure's operation. SHM strategies provide a continuous detection of the health and the integrity of a structure during its lifespan. This section discusses several damage detection techniques employed in SHM system, mainly focusing on the identification of structural and environmental parameters which highlight the presence of damage in the structure [38]. For instance, degradation of structural elements may alter the dynamical behavior of the system, and damage detection techniques compare the dynamical responses or the structural model matrices of the structure in healthy and damaged conditions [39]. These parameters should be regularly checked to assess the condition of the machine during operation. A damage detection technique should not only be able to discover the presence of damage, but also locate and quantify it [38].

SHM strategies are particularly significant for large structures or rotating machines, which experience very complex and non-linear conditions during their operating cycles [38], [40]. Furthermore, the space industry is also showing an increasing interest in SHM strategies to develop autonomous on-board failure detection capabilities [39]. This section will describe applications of damage detection techniques in rotating machines like wind turbines and helicopter blades and space structures such as large space antennas and inflatable modules.

4.1 SHM System for helicopter composite blades

While many non-destructive techniques are available for inspections of aircraft structures during ground checks, during flight the structures are not controlled for a long time, leaving unchecked the potential latent defects, which may grow and cause unexpected failures. Therefore modal analysis, especially OMA, is a promising technology which would allow to verify the structural integrity of an aircraft component in flight.

The research discussed by Mironov and Doronkin in their work titled "The Demonstrator of Structural Health Monitoring System of Helicopter Composite Blades", [40] aims to prove the potential of OMA techniques for monitoring of rotating blades. The study shows that OMA can be a promising technology for verifying the structural integrity of aircraft structures during flight. They compared analytical and experimental results and studied the sensitivity of the SHM system to seeded faults.

The research also identifies some obstacles in the implementation of OMA to aircraft structures, such as the need to mount numerous accelerometers on the structure, which may interact

with the flow if mounted on a streamlined surface, the influence of external factors, like rotational speed, maneuvers, payload, to the modal parameters of the blade, which can mask the modal variations due to damages in the structure, and the uneven frequency content of aerodynamic and mechanical loads, that is in contrast with OMA assumptions.

To overcome these problems, technical and methodical solutions are presented and applied on the SHM demonstrator. To begin, cheap dynamic deformation sensors with negligible thickness and mass are implemented in spite of the accelerometers. The modal passport (MP) approach is applied, enabling the estimation of modal properties of the operating structure considering the ambient and operational factors, thus reducing their influence on the results. A numerical simulation allowed the estimation of seeded faults to the modal parameters and the results were compared to the ones obtained with the experimental verification. A round hole in the tail (foam-filled) was used as damage, which replicates the main damage in rotor blades while take-off or landing. Two diameters for the damage were considered: 20 mm and 30 mm.

The Modal Parameters Variation (MPV) in Equation 4.1 was used to measure the blade's modal shape variation.

$$MPV = \sqrt{\sum_n (\bar{\epsilon}_n^d / \bar{\epsilon}_n^0 - 1)^2 / 100} \quad (4.1)$$

MPV calculates the total difference between normalized eigenvectors of damaged ϵ_n^d and reference ϵ_n^0 states in N points of the blade model. The Modal Parameter Variation Integrated (MPVI) can be defined from the MPV and represents the geometric average of normalized difference between eigenvectors of damaged and reference states:

$$MPVI = \sqrt{\sum_k MPV_k^2 / K} \quad (4.2)$$

where k is the mode number.

The simulation results showed that the presence of the damage causes slight change in modal frequencies, while the mode shapes are more sensitive, making them more informative for monitoring of rotating blades.

The experimental study was carried out on a light coaxial helicopter Ka-26, with each blade instrumented with 20 dynamic deformation sensors (Fig. 4.1). Four different test series

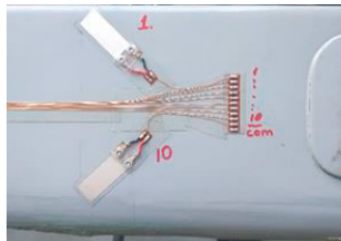


Figure 4.1: Dynamic deformation sensors [40]

were performed: two with healthy blade in reference state and two with seeded faults, with different fault dimension (20 and 30 mm). The modal parameters were estimated from the test results and the resulting eigenvectors of each blade were used to evaluate the influence of the damage on the modal properties. External factors (wind gusts) and own “noise” (electronic interference of the system) define the resolution threshold of the actual SHM system of rotating blade, which is 0.8%, while it was zero for the simulated case. This value was calculated by averaging the eigenvectors of the two reference state analysed in the experimental analysis,

as the blade's state remains the same between the two conditions, this MPVI level indicates the influence of external factors and errors of measurements system on the modal properties. Therefore it can be considered as the resolution level of the SHM system. It was demonstrated that the smaller fault does not exceed the threshold, so it is undetectable by the SHM system, while the larger hole is clearly detected (as can be seen in Fig. 4.2).

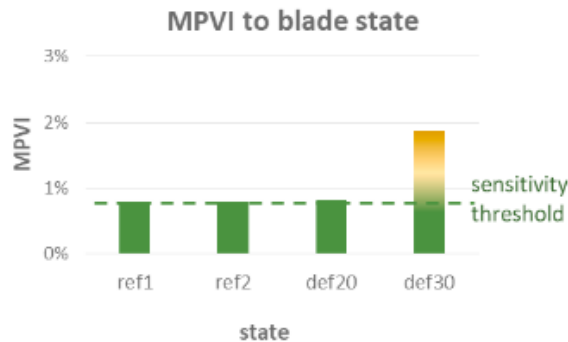


Figure 4.2: MPVI comparison for different states [40]

In conclusion, the research work demonstrated the applicability of deformation sensors rather than displacement sensors to reduce the cost of on-board equipment, while the application of MP approach for SHM strategies on rotating blades permitted the consideration of the external factors influence on modal properties. Therefore the technical and methodical solutions implemented improved the possibility of practical application of structural monitoring techniques to operating aircraft structures [40].

4.2 SHM for space structures

Space structures are designed to be very flexible and lightweight in order to comply with the weight restrictions that are imposed by the maximum take-off weight of rockets. However, the space environment is hostile, with various sources of damage, such as space debris impact, thermal stresses, and fatigue. Therefore, large, lightweight structures are more susceptible to structural damage. The consequences of structural failure are significant, as they can lead to changes in the control/structure interaction dynamics, which may interfere with the mission. This is particularly true for structures as space antennas or deployable solar arrays, which require high precision and stability. If their functionality is compromised by structural deterioration, it may jeopardize the success of the mission.

The implementation of SHM strategies is an intriguing approach for developing in-situ failure detection capabilities and performing in-orbit maintenance. Numerous studies have investigated the possibility of utilizing a distributed set of sensors on space structures to detect damage, identify its position, and quantify its severity to facilitate the development of a mitigation strategy and avoid mission abort before the spacecraft's end-of-life.

In particular, Iannelli, et al. [39] proposed a SHM strategy for a large space antenna (Fig. 4.3) using a Deep Neural Network (DNN). Traditional SHM techniques evaluate the change in modal parameters resulting from a variation in structural stiffness. However, this approach may not be sufficient when investigating large structures. Therefore, Iannelli, et al. [39] tested a data-driven methodology utilizing a DNN for damage detection. They studied the sensor sensitivity to damage classification for a satellite hosting a distributed network of accelerometers on a large mesh reflector antenna. Various damage scenarios were generated via FE

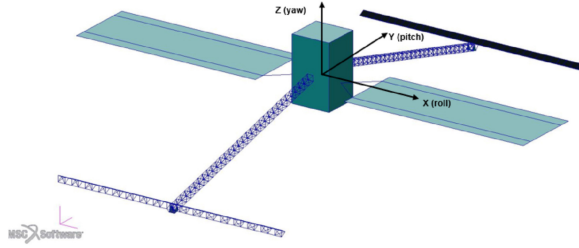


Figure 4.3: Sketch model of the large flexible spacecraft [39]

commercial code, and the DNN model was trained using the sensor-measured time series responses for each scenario. The research demonstrated the applicability of the DNN model for damage identification in large space structures by processing sensor-measured time responses, exhibiting good performance and accuracy.

Monitoring the structural health condition in-situ is highly desirable, also for inflatable structures. Although these structures are becoming increasingly common in space applications, their durability is a major concern due to their highly flexible material and ultralight weight, which increases their susceptibility to deterioration in the space environment.

In a study by Li, et al. [41], vibration-based SHM techniques were investigated on inflatable structures by observing the changes in the dynamic characteristics resulting from alterations in the physical properties due to structural failure. This paper primarily focuses on the integration of devices and the development of a miniature prototype capable of measuring the low-frequency dynamic stiffness of inflatable structures for the implementation of traditional vibration-based SHM approach. The recorded data are downlinked from the satellite to the ground where the dynamic stiffness is computed and compared to the original design to estimate the structural health condition. Experimental analyses were carried out on an inflatable boom (the experimental setup is shown in Fig. 4.4). Three transducers were bonded to the outer surface, one received the excitation signal and excited the structure, while the other two were used as sensors to detect the structural vibration. The three transducers were connected to an excitation output channel and two signal acquisition channels of the prototype, respectively. The experimental outcomes proved the accuracy of this prototype in the estimation of the modal parameters and its high reliability and numerous benefits when compared to conventional devices. In conclusion, this research work showed the potentiality of implementing vibration-based SHM techniques in inflatable space structures.

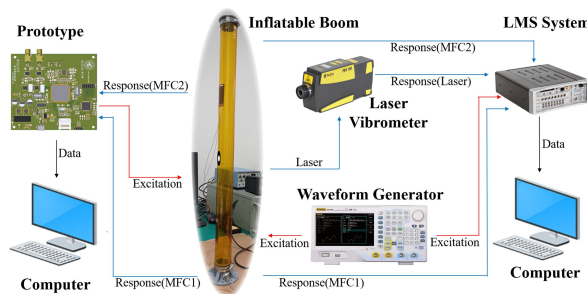


Figure 4.4: Experimental setup for the dynamic testing of the inflatable boom [41]

4.3 Damage detection on wind turbines

Damage detection techniques for wind turbines are typically based on changes in the structure's stiffness caused by damages, which affect the modal properties of the structure. Although natural frequencies are affected by stiffness reduction, the variation is very low, therefore, mode shapes approaches are preferred, as they lead to better estimations of the damaged regions.

The SHM technique is applied to wind turbine rotors by means of whirling modes as damage indicators, which are the most identifiable modes in both simulation and test environments. The whirl mode is described by Di Lorenzo, et al. [38], as follow: the whirling mode is generated by two cyclic in-plane modes of the rotor; in a single-frequency whirl mode, the rotating force vector on the shaft is composed by a regressive force vector rotating at lower frequency and a progressive force vector rotating at higher frequency.

SHM strategies can use the whirling mode as damage indicator for wind turbines, since it is characterized by the fact that the blades are shifted in phase by a factor equal to 120° and have the same amplitude, in a symmetric case. If the symmetric property of the mode is lost under operational conditions, there could be an incipient damage formation.

Di Lorenzo, et al. [38] discussed this possible SHM strategy and the influence of a reduction of the stiffness in the whirl mode. The study resulted in the conclusion that both the amplitude and the phase of these modes are suitable damage indicators, since they are sensitive to small changes in the stiffness of the blades, as shown in Fig. 4.5.

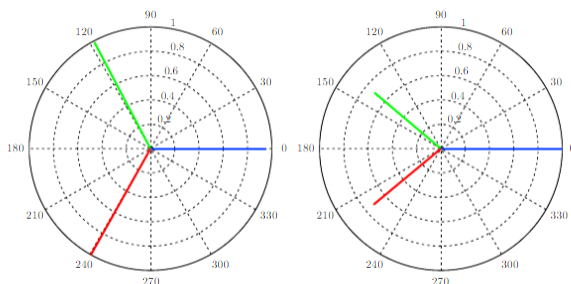


Figure 4.5: Whirling modes: Healthy case (left) vs Stiffness reduction ($k_1=0.99$) [38]

For beam-like structure, Di Lorenzo, et al. [38] described a potential damage detection technique for SHM purposes using modal curvatures. This method involves the computation of modal curvatures for the damaged and undamaged structure and using the last one as normalization parameters. By calculating, the Modal Shape Curvature Index ($MSCI_i$) as shown in Equation 4.3, any discontinuity in this index can indicate the presence of a structural fault in the corresponding regions. Here, $\ddot{\Phi}$ refers to the second derivative of the mode shape.

$$MSCI_i = \frac{\ddot{\Phi}_{i,r}^{undamaged}}{\ddot{\Phi}_{i,r}^{damaged}} \quad (4.3)$$

This damage detection technique was implemented on a wind turbine blade, which can be treated as a beam-like structure. The blade is a 6.5 m fiberglass from a small wind turbine. The FE model of the structure was developed and validated with test data to study its dynamic behavior. Once the numerical model is validated it can be used for vibration-based SHM purposes. The model was simplified for computational reasons in an equivalent 1D beam model. The damage was simulated by reducing the mechanical properties of the beam material in a certain region.

The MSCI technique was then applied for the damage identification. The results showed that the second derivative of the displacement mode shapes (mode curvature) can provide a good

indication of the presence of a crack, and can be used to estimate the position and size of the damaged region of the structure [38]. The extension of the damaged region is evidenced by the intersections between the curvature of healthy structure and the curvature of damaged structure, as illustrated in Fig. 4.6.

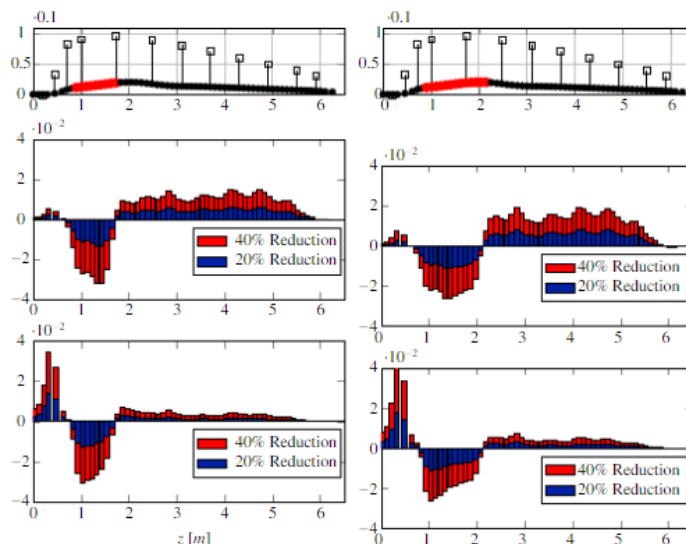


Figure 4.6: Normalized curvatures of the 1st and 2nd mode shapes [38]

The implementation of SHM strategies using physical sensors on wind turbines, especially offshore wind turbines, are hard to find. Many studies have focused on damage detection on blades, such as the previous one from Di Lorenzo, et al. [38].

Siebel, et al. [42] explored the applicability of OMA to detect damage in a small-scaled on-land wind turbine by analyzing the acceleration on the tower and estimating its modal properties. They proved that OMA and the curvature mode shapes are suitable for damage detection in a real small-scale wind turbine.

In Kim, et al.'s work, [43], they proposed a SHM method for Floating Offshore Wind Turbines (FOWTs) using OMA with numerical-sensor signals. Natural frequencies, displacement modes shapes and curvature mode shapes of the tower and blades are investigated. The modal properties were used as damage indicators by comparing the healthy and damaged conditions. This study revealed once more that the curvature mode shapes were the most effective instrument for damage detection.

The proposed SHM method was applied as follow: first the accuracy of OMA was verified using time-domain numerical simulations, by comparing the modal properties of the intact structure obtained from OMA and the ones obtained from the FE model, then the effects of non-linear mooring stiffness, waves, and coupling between tower and blades on modal properties were investigated. The SHM of the tower was performed by comparing intact and damaged conditions in frequency and time domains, and using the results to detect damaged locations and estimate damage intensity. The methodology also included using FE model analysis to verify changes in modal properties obtained from OMA.

4.4 Response estimation techniques for Wind Turbine SHM

The primary issue in SHM of offshore wind turbines is that most of the fatigue sensitive locations are inaccessible for direct measurements since traditional sensors cannot be mounted on those parts of the structure. To overcome this issue, researchers have developed methods to estimate the structural response of the offshore wind turbine at unmeasured locations.

Iliopoulos, et al., [37], developed a method to estimate the structural response of an offshore wind turbine at unmeasured locations using a limited number of response locations and a FE model. The structure instrumented for the OMA is the tower. The FE model was calibrated by comparing the experimental results with the numerical mode shapes in terms of the MAC (Fig. 4.7 shows the comparison between the mode shapes from the FE model and the OMA results). Then, this calibrated numerical model provided information for predicting accelerations at

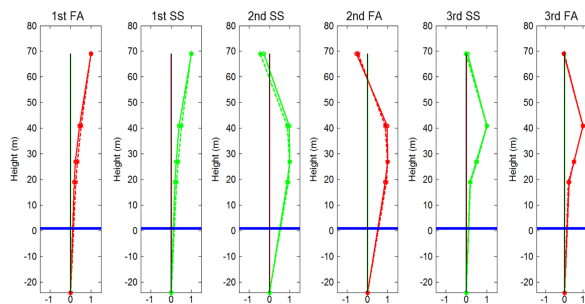


Figure 4.7: Overlay plot of the 6 fundamental tower-foundation mode shapes derived from OMA (continuous line with circular points) and FE model (dashed line with star points) [37]

different locations on the structure. In this work the authors used a modal decomposition and expansion algorithm for response estimation and validated the method using both simulated datasets and real time data from an OMA campaign on a Vestas V90 3 MW offshore wind turbine.

Fig. 4.8 shows the results of the FA acceleration prediction at the lowest sensor level in rotating conditions of the wind turbine. The red curve refers to acceleration obtained from the measured acceleration, while the green one represents the predicted accelerations. There is a good agreement between the measured data derived from the monitoring campaign and the predicted data using the modal decomposition and expansion technique.

Maes, et al. [44] estimated the dynamic strains in a tower of an offshore monopile wind turbine from a limited set of sensors and a system model. The authors compared the results of three response estimation techniques: a Kalman filtering algorithm, a joint input-state estimation algorithm, and a modal expansion algorithm.

The algorithms have been applied to measurement data derived from a monitoring campaign on a Vestas V90 3MW wind turbine on a monopile foundation. The campaign consisted of eight data sets with a duration of 10 min each, both in rotating conditions and in parked conditions. A FE model of the wind turbine was updated using experimental modal results from an output-only system identification procedure with data obtained in parked conditions. The system model was built from this FE model.

To verify the response estimation algorithms feasibility the fore-aft and side-side strain at the lowest measurement level was predicted. All algorithms were evaluated using two different sensor configuration: S1 with acceleration data only and S2 with a combination of acceleration and strain data. The results obtained with the three algorithms in rotating conditions using only accelerations data showed that the joint input-state estimation algorithm and the modal

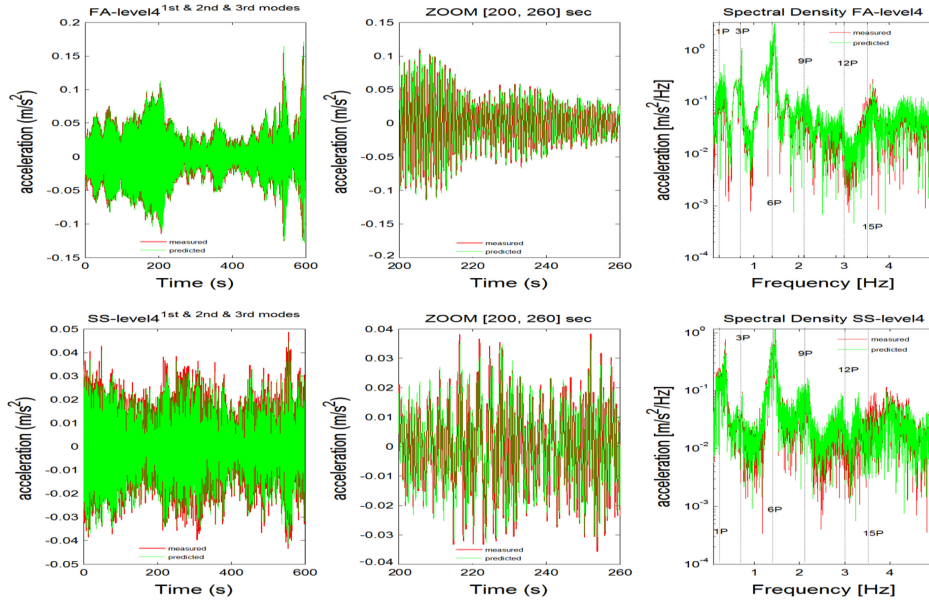


Figure 4.8: Time domain and frequency domain comparison of predicted (green) and measured accelerations (red) at the lowest sensor level in FA and SS direction for rotating conditions of the wind turbine. The nominal rotation frequency 1 P at 0.235 Hz (14.1 rpm) and the higher order harmonics up to 15 P are shown in the frequency domain plot for the indicative timestamp [37]

expansion algorithm yielded better results than the Kalman filter. Minor improvements were detected in the two algorithms when the measured strains were included. On the contrary, including the measured strains improved significantly the results of the Kalman filter. In particular, it showed superior results for the side-side strain with respect to the other two techniques. The results for the three response estimation techniques for rotating conditions and sensor configuration S_2 , which included strain measurements, are shown in Fig. 4.9, 4.10 and 4.11.

In conclusion, the Kalman filter accuracy depends on the data, the results can be improved if the correct data are given to the algorithm, thus the three techniques are competitive and interchangeable for this application.

A digital twin concept is also presented in the work of Branlard, et al. [45], where the focus is posed on the estimation of wind speed, thrust, torque, tower-top position, and loads in the tower of an on-land wind turbine. The model was made with the linear state-space model obtained via OpenFAST linearizations, a wind speed estimator and a Kalman filter algorithm that integrates measurements with the state model to perform state estimations. The model validation was conducted with experimental data from the GE 1.5-MW turbine from the National Renewable Energy Laboratory test site. The OpenFAST linearization capability extends the method to a higher number of states, inputs, outputs, and to the applications to offshore wind turbines.

The model had an average accuracy of 10% in estimating real-time damage equivalent loads of the tower bottom moment. Overall, the proof of concept results were encouraging for further application of the model.

These studies provide valuable insights into the development of SHM for wind turbines, enabling accurate predictions of structural responses and loads to support effective maintenance and management strategies.

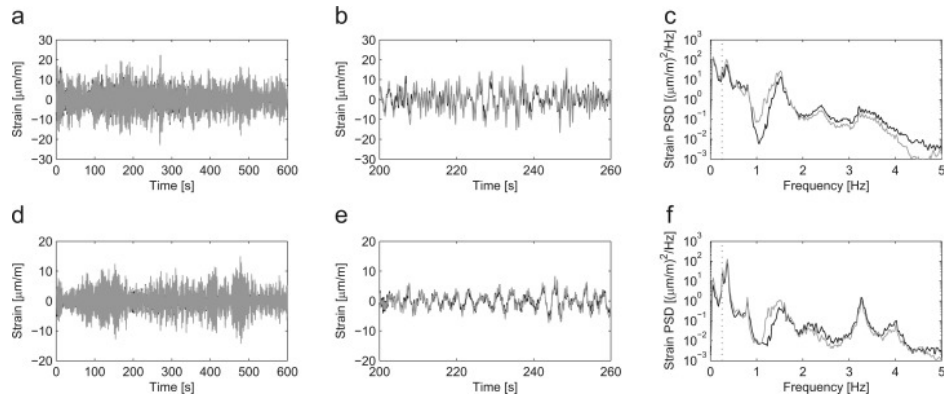


Figure 4.9: Time history (left), detail time history (middle) and estimated PSD (right) of the FA strain (top) and SS strain (bottom) at level $h=19$ m LAT for rotating conditions, sensor configuration S_2 . The measured strains are shown in black, the estimated strains obtained from the Kalman filter are shown in gray [44]

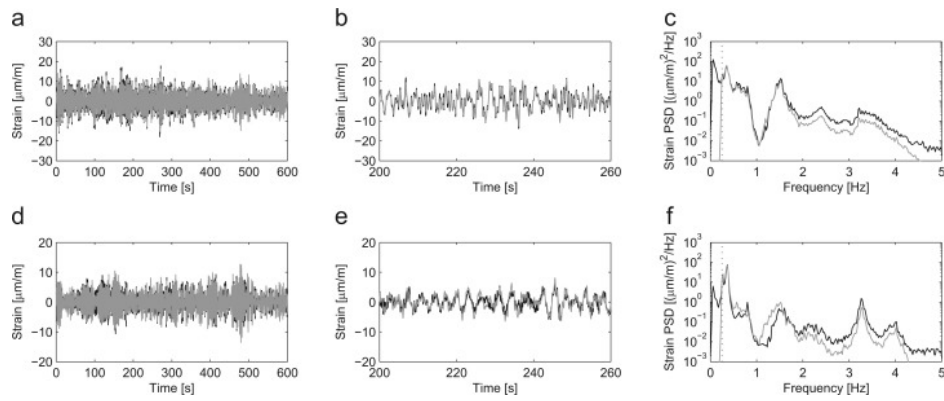


Figure 4.10: Time history (left), detail time history (middle) and estimated PSD (right) of the FA strain (top) and SS strain (bottom) at level $h=19$ m LAT for rotating conditions, sensor configuration S_2 . The measured strains are shown in black, the estimated strains obtained from the joint input-state estimation algorithm are shown in gray [44]

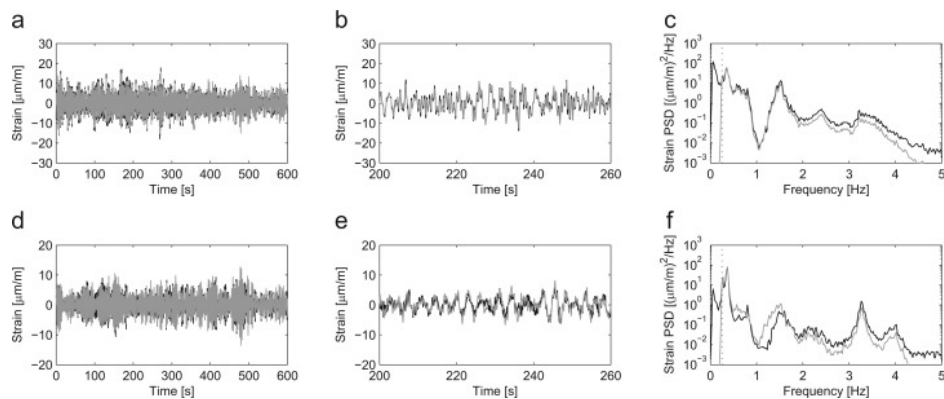


Figure 4.11: Time history (left), detail time history (middle) and estimated PSD (right) of the FA strain (top) and SS strain (bottom) at level $h=19$ m LAT for rotating conditions, sensor configuration S_2 . The measured strains are shown in black, the estimated strains obtained from the modal expansion algorithm are shown in gray [44]

Chapter 5

Wind Turbine FE Model

This section will present the Computer-Aided Design (CAD) and FE model of the small-scale wind turbine under study, along with the challenges encountered during the modeling process and the computational tools utilized to create the numerical model. The CAD model of the wind turbine was provided by the Technical University of Denmark (DTU) together with the small-scale wind turbine specimen.

Because of the advent and development of computer technologies, numerical modeling and simulation for engineering systems has evolved fast. Wind turbines are complicated structures in terms of design and dynamic behavior, necessitating extensive FE modeling.

Simcenter 3D Pre/Post, a software from Siemens Digital Industries Software, is used to construct the FE model. Due to the tower's complexity, it is required to remove bolts and other small parts in order to simplify the model. Then, each item is separately meshed with either 3D or 2D meshes.

5.1 Model Description

The test object is a small replica of a real wind turbine. It is made up of various elements; the tower is the main part that supports the entire structure, it is 1.5 m tall and has an 80 mm diameter (Fig. 5.1). On top of the tower, a cylindrical insert connects the tower to the nacelle (Fig. 5.3), which houses the motor, and bolts hold the three components together. The rotor of the blades is located in front of the nacelle, closed with the conic hub in the front part and connected to the three blades via bolt connections (Fig. 5.2).

The motor inside the nacelle is an electric motor (Fig. 5.4), with its shaft inserted into the hole of the rotor. The two components rotate in tandem, and the motor transfers torque to the rotor of the blades, causing the blades to rotate.

The wind turbine is a three-bladed turbine. The CAD model for blades is unavailable, however the FE model was generated without the geometry and has already been validated. Because there is not a CAD geometry behind the FE model the model is computationally complex.

Three inserts allow the connection of the blades to the wind turbine via six bolts, six nuts, and six washers.



Figure 5.1: WT Tower CAD



Figure 5.2: Rotor CAD

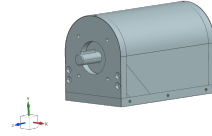
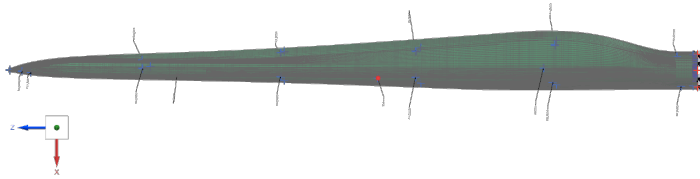


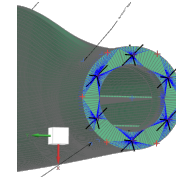
Figure 5.3: Nacelle CAD



Figure 5.4: Motor CAD



(a) Blade FEM



(b) Blade FEM detail

5.2 Material Description

Except for the tower and the blades, which are made of composite materials, the material is primarily aluminum. The electric motor's material properties are unknown.

A material with the same properties as Aluminum 6061 is created and assigned to the mesh collector of the corresponding components (nacelle, rotor, hub and tower inserts). The material properties are shown in Table 5.1.

Table 5.1: Aluminum 6061 material properties

Aluminum 6061	
Mass Density (ρ)	2.711 g/cm ³
Young's Modulus (E)	68980 MPa
Poisson's Ratio (ν)	0.33

Given the unknown material of the motor, its mesh is modelled using a material with the same properties of the Aluminum 6061. Initially, the material properties of the motor are set to the values presented in Table 5.1. As test results become available, the material properties of the motor will be refined in the update process.

The tower of the wind turbine is a tube that was fabricated by Princefibre. It is composed of a composite material, and its specific characteristics and properties are provided by the

manufacturer. It is a unidirectional carbon fiber braded with epoxy resin. The fibers are T300 carbon fibers and are produced using filaments and bounded with epoxy, while the tower shape is created by poltrusion. The composite material contains 60% volume fiber content. The material is composed of 5 layers of varying thickness and fiber orientation, as shown in Table 5.2. Within the Simcenter 3D environment, an NX Nastran PCOMP property is created and assigned to the 2D mesh to represent the composite material. The PCOMP is a Layered Composite Element Property that defines the properties of an n-ply laminated composite material. When defining the PCOMP property, the following properties must be assigned to each ply: material, thickness, orientation angle of the longitudinal direction of each ply with respect to the element’s material axis. The shell element direction is the reference direction for the fiber orientation angle in the PCOMP property. The plies are serially numbered, beginning with the first one at the bottom layer. The surface with the largest negative z value in the element coordinate system is defined as the bottom layer. If the normals are pointing outwards, the first layer is internal. The material assigned to each ply is created in Simcenter 3D using MAT8. MAT8 defines the properties of an orthotropic material for isoparametric shell elements in NX Nastran. Table 5.3 lists the material properties assigned to each ply. An approximate value for G13 and G23 is the in-plane shear modulus G12. These properties are not guaranteed and will be updated just after the correlation with the test results in order to approach the test results with the model ones (chapter 8).

Table 5.2: Composite material layers properties

Ply Number	Thickness mm	Orientation Angle °	Material
1	1.2	0	Carbon fibre/epoxy
2	0.495	90	Carbon fibre/epoxy
3	1.28	0	Carbon fibre/epoxy
4	0.0125	45	Carbon fibre/epoxy
5	0.0125	-45	Carbon fibre/epoxy

Table 5.3: Composite material properties

Carbon fibre/Epoxy	
Mass Density (ρ)	1.55 g/cm^3
Young’s Modulus (E1)	130000 MPa
Young’s Modulus (E2)	7900 MPa
Poisson’s Ratio (ν)	0.3
Shear Modulus G12	5000 MPa
Shear Modulus G13	5000 MPa
Shear Modulus G23	5000 MPa

5.3 FE modeling

The idealized part of the geometry described in Section 1.1 is developed to modify the geometry without altering the original model. Midsurfaces of thin-walled components can be created on the idealized part, after which the new geometry is promoted in the FE model file and the mesh can be applied to the midsurface. This process is carried out prior to the application of 2D meshes to the thin-walled components: the curved nacelle wall, and the cylindrical surface of the tower. The thickness of these two components is minimal; the curved nacelle wall is 0.5 mm thick, while the tower is 3 mm thick. 3D meshes are used to mesh every other component.

The link between the components, which should take into consideration the reciprocal behavior between the pieces of the assembly and their relative motion, is a crucial aspect in modeling.

The chosen method is to apply a mesh mating condition command to the parts that are in contact; this function merges the shared nodes between the adjacent meshes so that the parts behave as if they are joined. The software ensures that connectivity is maintained at that interface and creates identical meshes on two faces to facilitate contact definition.

The complete FE model of the wind turbine was achieved by utilizing CQUAD8 and CQUAD4 elements for the 2D meshes, as depicted in Fig. 5.6 and 5.9b, CTETRA10 elements for the 3D meshes, as illustrated in Fig. 5.7, 5.8, 5.9a, 5.9c, 5.10 and CHEXA8 elements being used for the 3D model of the blades, Fig. 5.11. The resulting FE model of the wind turbine is presented in Fig. 5.12. In particular, for the 2D tower model QUADRANGOLAR elements with 8 nodes were used, while TETRAGONAL elements with 10 nodes were used for the nacelle, the motor and the rotor parts. For the GFRP wind turbine blade, the FE model was provided by DTU, who adopted the in-house Blade Modelling Tool [46], modelled using hexahedral elements with eight nodes per element. Finally, each component's mesh and attributes are summarized in Tables 5.4, 5.5, 5.6.

Table 5.4: Mesh modeling: tower and inserts

Component	Tower	Tower Inserts
Mesh Type	2D	3D tetrahedral
Element Type	CQUAD8	CTETRA10
Mesh Element Size	7 mm	6 mm
Material	Composite Material	Aluminum 6061

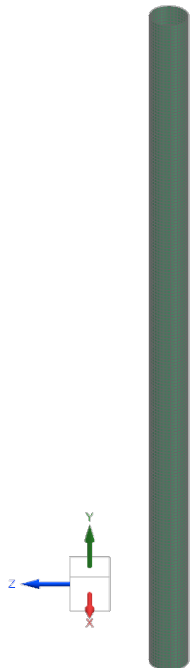


Figure 5.6: Tower mesh

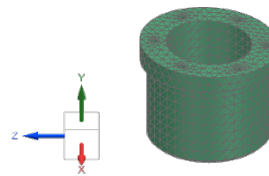


Figure 5.7: Top insert mesh

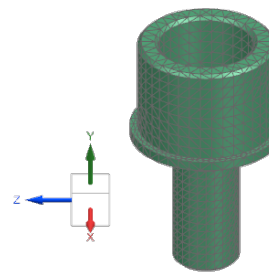


Figure 5.8: Bottom insert mesh

Table 5.5: Mesh modeling: nacelle

Component	Nacelle Walls	Nacelle Curved Surface	Motor
Mesh Type	3D tetrahedral	2D	3D tetrahedral
Element Type	CTETRA10	CQUAD4	CTETRA10
Mesh Element Size	6 mm	2 mm	6 mm
Material	Aluminum 6061	Aluminum 6061	Aluminum 6061

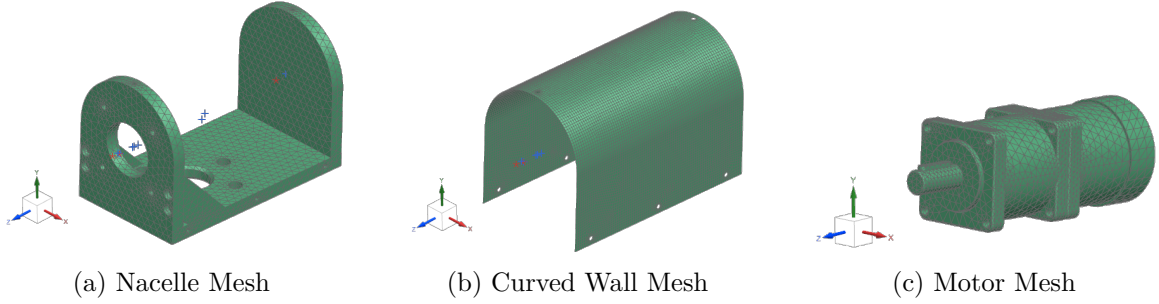


Figure 5.9: Nacelle and Motor Mesh

Table 5.6: Mesh modeling: rotor and hub

Component	Blades' Rotor	Rotor Hub
Mesh Type	3D tetrahedral	3D tetrahedral
Element Type	CTETRA10	CTETRA10
Mesh Element Size	5 mm	5 mm
Material	Aluminum 6061	Aluminum 6061

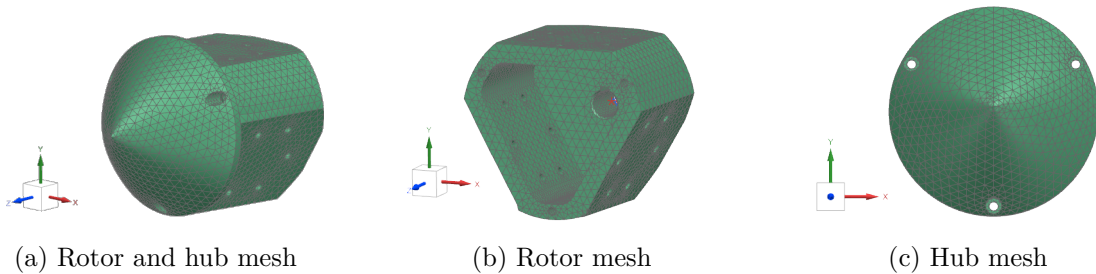


Figure 5.10: Rotor assembly mesh

5.3.1 Gluing and 1D connections

Since the mesh mating command is only supported for 3D meshes, a surface-to-surface gluing between the nacelle curved wall and the other walls has been adopted to model their connection. A surface-to-edge gluing is also modeled between the tower and the inserts for the same purpose.

The surface-to-surface gluing method is utilized to connect two surfaces, ensuring that there is no relative motion in any direction. In Simcenter 3D, a glue connection is a simple and efficient technique for connecting dissimilar meshes. The gluing zones feature shell elements and solid element faces. The glue connection accurately transfers displacement and loads, thereby maintaining an accurate strain and stress condition at the interface.

Simcenter Nastran automatically generates glue elements between selected surfaces or edges

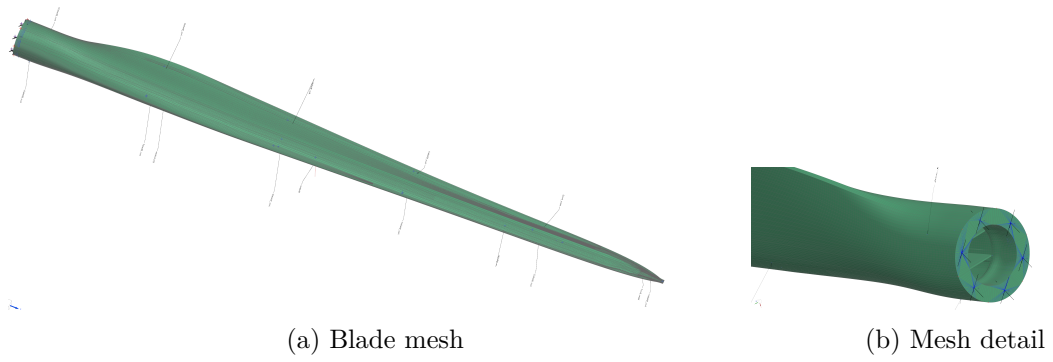


Figure 5.11: Blade mesh

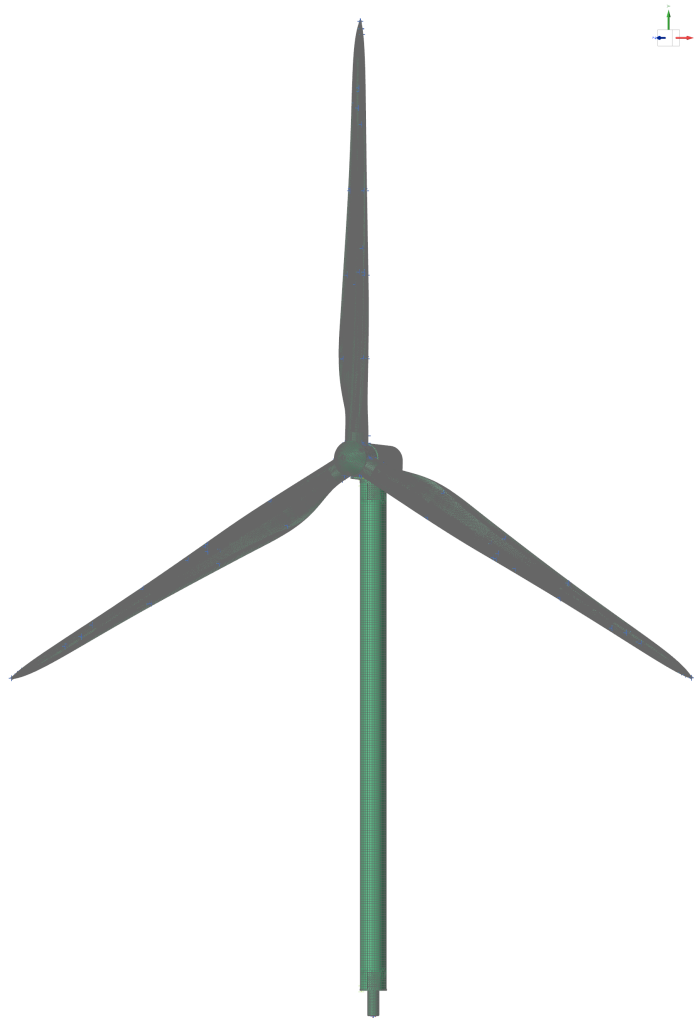


Figure 5.12: Entire FE model

and surfaces during model solving. These glue components act as rigid springs that constrain and link the surfaces and edges. Simcenter Nastran always utilizes a weld-like formulation when creating the connection, corresponding to the `GLUETYPE=2` option on the `BGPARM` bulk entry.

The curved midsurface of the nacelle is glued to the surrounding nacelle walls, as illustrated in Fig. 5.13.

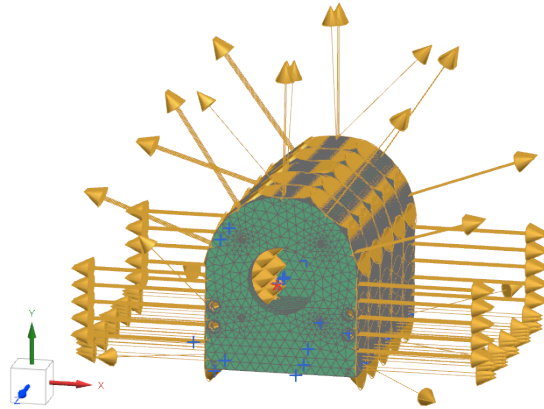


Figure 5.13: Nacelle gluing connection

As illustrated in Fig. 5.14a and 5.14b, the tower is attached to the inserts, and a connection is formed between the tower's circular edge and the insert surface that is in contact with the tower.

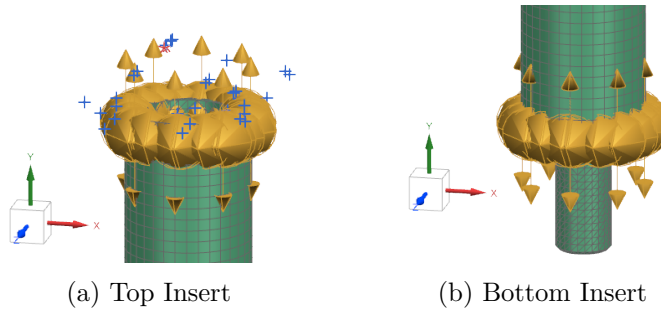


Figure 5.14: Tower and inserts gluing connection

While the glue connection is a useful tool for connecting surfaces that are in contact, it is insufficient for achieving a realistic representation of the structure when components are not in direct contact with one another. In cases where there are components that interact with each other but are not in contact, rigid connections must be introduced to model their connection. These rigid connections are typically 1D in nature and help reduce the relative displacement between the connected components.

This type of connection concerns the positioning of the motor within the nacelle as well as the relative motion of the tower and the two inserts. As previously described, the tower is already attached to the inserts via a gluing connection between the tower's circular edge and the inserts surfaces that are in contact with the tower. However, the rigid interaction between these three elements at the regions that are not in contact must be taken into account. The tower is therefore linked to the two inserts using RBE2 rigid elements via a node-to-node connection. The nodes involved in the connection are the external nodes on the insert cylindrical surface and the internal nodes on the tower surface. The connections are shown in Fig. 5.15a and 5.15b.

Since the motor's placement inside the nacelle cannot be retrieved via a physical inspection, it is uncertain how it is secured within the nacelle. As a result, in the model, its motion is

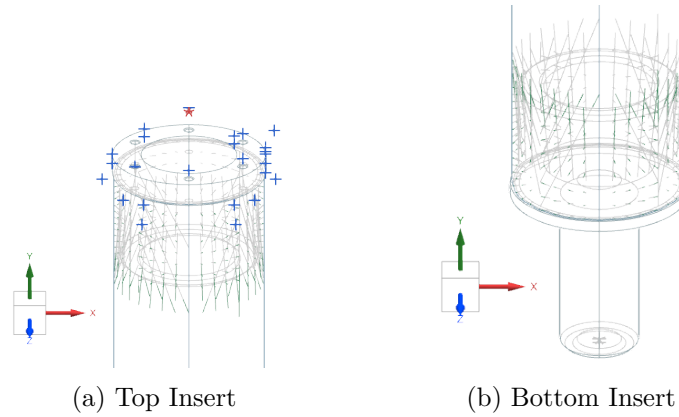


Figure 5.15: Tower and inserts 1D connections

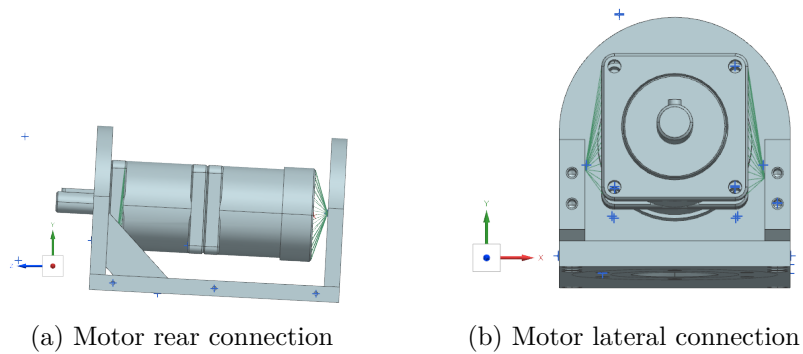


Figure 5.16: Motor 1D connections

limited by creating a spider connection between the motor's rear wall and the nacelle one, as well as between the motor's lateral faces and the nacelle's lateral faces, as shown in Fig. 5.16a and 5.16b.

The major challenge concerning the modeling of wind turbine structure lies in the replication of the connection between the rotor and the motor. The motor shaft, which fits into the rotor hole, connects the two bodies by passing through the nacelle wall hole. In the actual wind turbine, the motor shaft can rotate at a small angle, and the rotor of the blades rotates with it. The challenge consists in connecting the rotor, the motor, and the rest of the structure without limiting the rotational degree of freedom of the blades' rotor and the motor rotor around their axes. For this reason, the motor's CAD has been modified by dividing the body into two parts, a stator and a rotor. As previously stated, the stator is constrained to the nacelle (Fig. 5.16a,5.16b). The rotor is instead constrained to the stator via 1D connections, with unblocked rotor's relative rotation around its axis with respect to the stator. The connection is modeled via a spider connection with RBE2 elements between the nodes of the rotor's cylindrical wall (leg nodes) and an independent central node, as well as a spider connection with RBE2 elements between the nodes of the stator's inner cylindrical wall (leg nodes) and an independent central node. Even though their positions coincide, the two independent nodes of the two spiders are distinct nodes connected by an RBE2. All degrees of freedom except rotation around z are locked in the last RBE2 connecting the two independent nodes, allowing relative rotation of the rotor with respect to the stator.

Another 1D connection is built between the independent node of the motor's rotor spider and the independent node of the spider inside the blades' rotor hole to reduce rotor deformation.

All the nodes on the hole surface serve as leg nodes for the spider connection, and a central node in the hole section serves as an independent node. The spiders' central node-to-node connection is constructed via an RBE2 element with all degrees of freedom fixed.

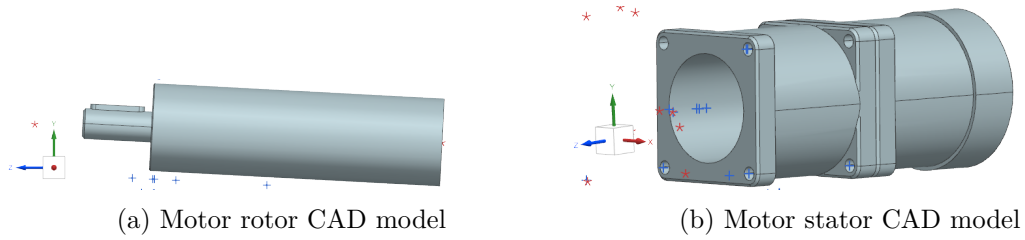


Figure 5.17: Motor CAD modified model

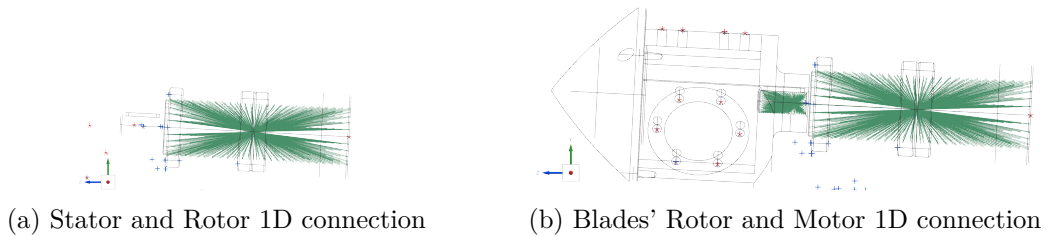


Figure 5.18: 1D connection for the rotor and motor structure

The blades' connection to the rotor is created using i) 6 spider connections, with the dimension of the holes on the rotor surfaces and ii) 6 spider connections on the blade's surface involving the nodes shown in Fig. 5.19a. The spider elements are linked via a node-to-node connection with RBE2 elements. Six spider to spider connection are created to replace the bolt connections.

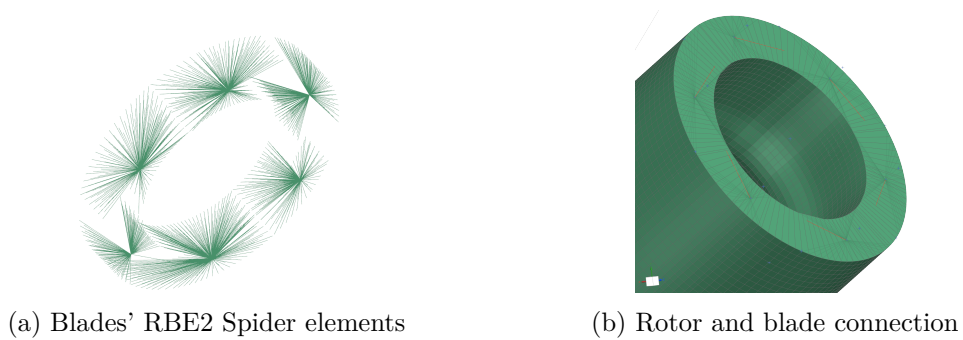


Figure 5.19: Blade and Rotor connection

5.3.2 Boundary conditions

The support of the wind turbine consists in a tripod which secures the wind turbine to the ground, despite the tower's slight movement and oscillation from its nominal position. Although theoretically simple, boundary conditions such as fixed constraints or hinges may pose practical challenges during implementation. Achieving an almost perfect clamping is a difficult task that often results in discrepancies between numerical and experimental resonance

frequencies and mode shapes. Therefore, to closely simulate the actual structural behavior, various solutions are analyzed to determine the optimal configuration that best represents the actual boundary conditions.



Figure 5.20: Wind turbine base and supporting tripod

The initial step of the study involves creating three CELAS spring elements at the base of the tower to emulate the tripod. The stiffness of these elements is not a physical variable but is defined to approximate the rigidity of the support system. Nevertheless, it is crucial not to overestimate the stiffness to achieve accurate results. A spider connection is created at the hole of the tower's bottom insert and the three springs are connected to its central node. A fixed constraint secures the external node of the springs, and the nodes on the external surface of the insert are clamped, as illustrated in Fig. 5.21. However, this approach was found to be excessively rigid, necessitating the investigation of alternative solutions.

In particular, it was found that a too stiff boundary condition was produced by the fixed constraint. Additionally, the springs appeared redundant. As such, they have been discarded in favor of clamping the central node of the three springs elements. Consequently, a preferred solution was identified, which involves a basic spider connection located at the bottom of the insert. The leg nodes are represented by the circumferential nodes of the hole, while the independent core node is the central node of the hole at the same height. A fixed constraint is applied to the core node, as depicted in Fig 5.22. The results obtained with this constraint configuration are deemed satisfactory, and they closely approximate the actual behavior of the structure. This is confirmed by the mode shapes and the first frequency values that reliably match the experimental results, as demonstrated in chapter 6.

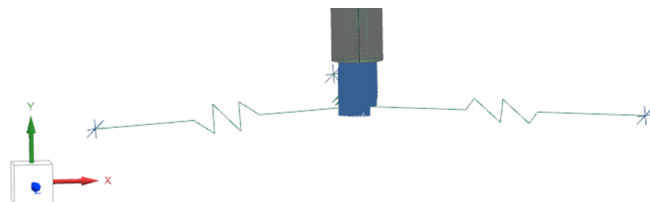


Figure 5.21: 1st Constraint configuration

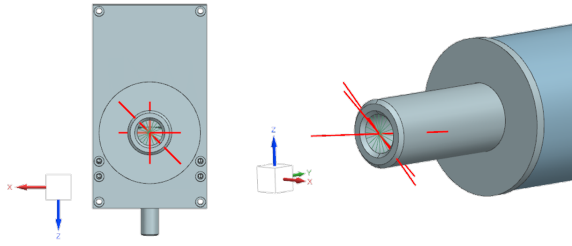


Figure 5.22: Final Constraint Configuration

5.4 Eigenvalue solution

5.4.1 Tower and hub modal parameters

The final step consists in running a SOL103 (Real Eigenvalues) in Siemens NX Software, to determine the undamped natural frequencies and associated mode shapes. It should be noted, however, that SOL 103 does not factor in structural damping. Nevertheless, this approximation is considered reasonable as all the identified modes in the tests have low damping ratios of less than 5%.

A maximum frequency of 850 Hz is used in the analysis, which is restricted to the first 16 modes. The natural frequencies and shapes descriptions are listed in Table 5.7. Fig. 5.23a to Fig. 5.26d illustrate the sixteen mode shapes.

The first fore-aft and side-side bending of the tower and the second bending in the two directions are both included in the structure's first five modes. The fundamental modes for the wind turbine tower are the first two bendings. Indeed, when the entire structure is analyzed, the dominant blades mainly affect the dynamic of the entire wind turbine structure, leaving only the first tower bendings in the fore-aft and side-side directions. As a result, common wind turbine studies mainly focus on the first tower mode.

Resonance is intended to be avoided by keeping this first mode at a safe distance from the turbine's excitation frequency range [10]. The associated natural frequencies for the first mode shape are 7.36 Hz for the first bending FA and 7.51 Hz for the first bending SS. The sixth through ninth mode, or frequencies between 349 and 567 Hz, are high-order bending modes. For frequencies higher than 567 Hz, tower torsional modes are detected.

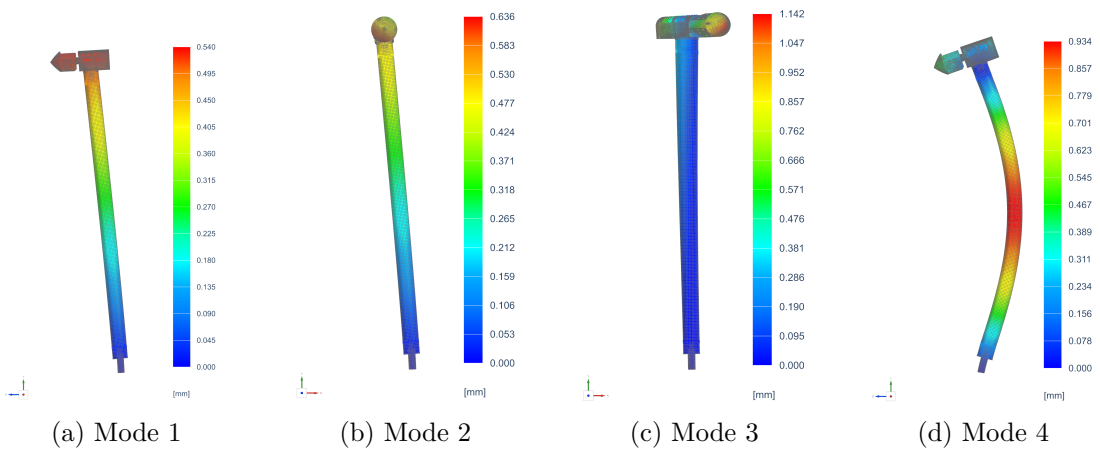


Figure 5.23: Modal shapes of the wind turbine tower structure (1,2,3,4)

Table 5.7: Natural frequencies and shapes description

Mode number	Natural Frequencies [Hz]	Shapes description
1	7.36	1 st bending of the tower FA
2	7.51	1 st bending of the tower SS
3	63.35	1 st torsional of the rotor and the nacelle
4	135.82	2 nd bending of the tower FA
5	145.28	2 nd bending of the tower SS
6	348.85	3 rd bending of the tower FA
7	455.57	3 rd bending of the tower SS
8	514.11	4 th bending of the tower FA
9	567.03	1 st torsional of the tower
10	584.86	Mixed vibration (bending and torsional)
11	596.61	2 nd torsional of the tower (xy plane)
12	603.44	2 nd torsional of the tower (out of plane)
13	654.31	3 rd torsional of the tower (xy plane)
14	663.82	3 rd torsional of the tower (out of plane)
15	785.96	4 th torsional of the tower (xy plane)
16	796.12	4 th torsional of the tower (out of plane)

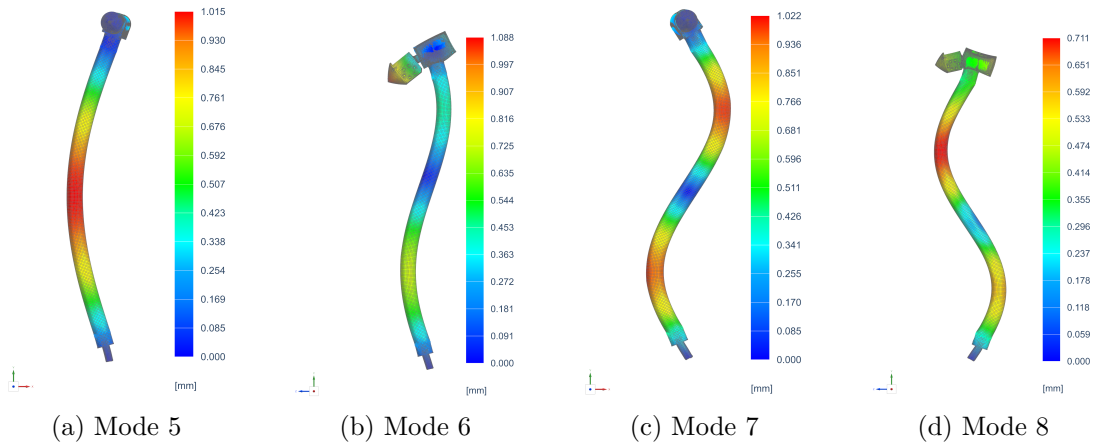


Figure 5.24: Modal shapes of the wind turbine tower structure (5,6,7,8)

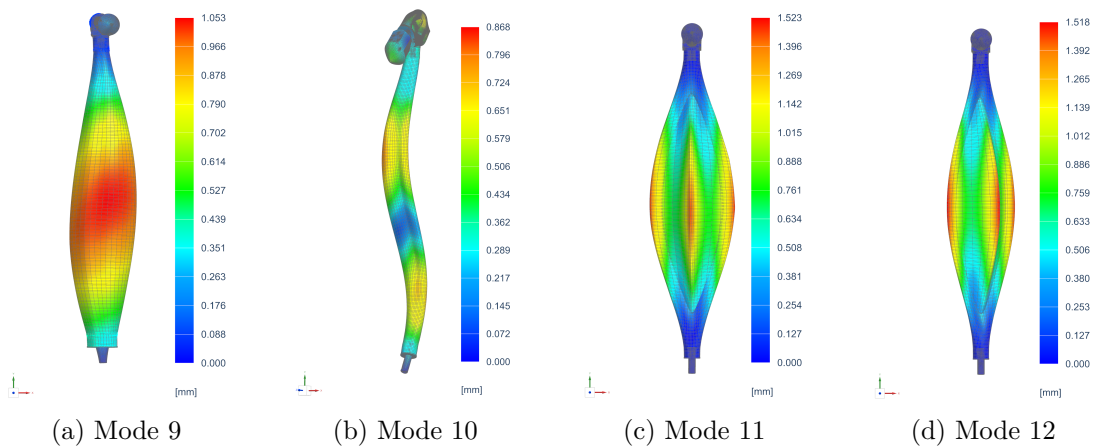


Figure 5.25: Modal shapes of the wind turbine tower structure (9,10,11,12)

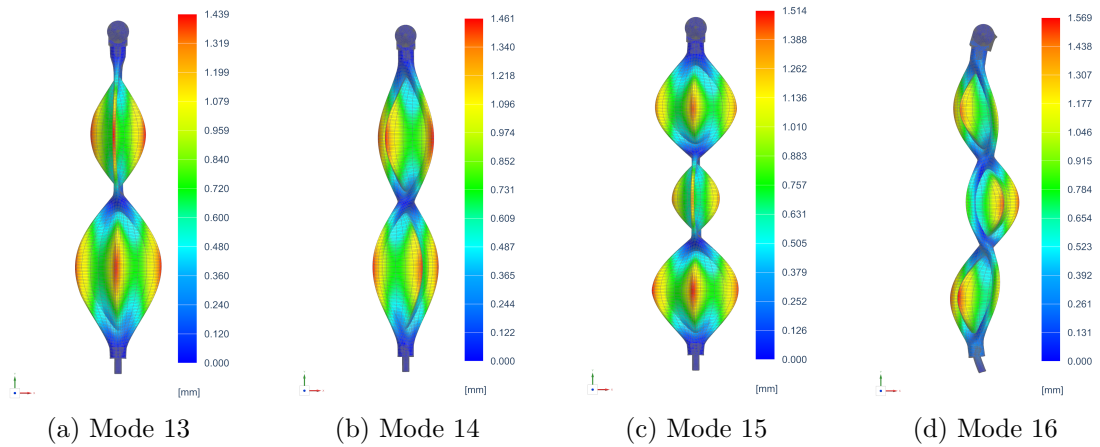


Figure 5.26: Modal shapes of the wind turbine tower structure (13,14,15,16)

Later in the text, the accuracy of these results will be confirmed through EMA, and the Simcenter 3D tool - Model Update and the Sol200 solution will be used to update the model. Chapter 6 presents the EMA results, while chapter 8 presents the results and conclusions obtained through the model update.

5.4.2 Wind turbine modal parameters

The analysis of the wind turbine treated in this section covers the entire system, including the three blades that are connected to the rotor via rigid elements (RBE2) and the tower model, whose update is described in chapter 8. The rigid elements connect the six spiders on the rotor surfaces with the six spiders on the blades' surfaces, as previously described, thus completing the model.

To improve the match between the model and the actual structural configuration, a reassessment of the boundary conditions is necessary, since the blades presence introduces instability of the setup due to the uneven size ratio between the blades and the tower. The previously considered boundary condition configuration is reviewed for the entire model constraint. The tripod rods at the base of the wind turbine tower are replicated by creating three spring elements using CBUSH elements, which feature three translational and three rotational stiffnesses, unlike CELAS elements, which are uniaxial. The stiffness values for all three springs are equivalent, with values of 1×10^{17} N/mm for K_1, K_3, K_4, K_5, K_6 , and 1×10^{12} N/mm for K_2 . The translational stiffness in the y direction is lower because the test results demonstrate that the structure is partially free in this direction. These parameters are used as design variables for the optimization in the final model update (chapter 8).

In order to evaluate the frequencies and mode shapes of the wind turbine, a SOL103 (Real Eigenvalues) analysis was conducted, where the number of mode shapes was set to 10 and the frequency range between 5 and 52 Hz. It should be noted that these first 10 modes include the primary modes of the wind turbine and provide sufficient information to study its dynamic behavior.

The natural frequencies and shapes descriptions are listed in Table 5.8, while Fig. 5.27a-5.30b illustrate the ten mode shapes.

The results of the analysis indicate that the identified mode shapes entail the bending of the tower in both the fore-aft and side-side directions, the first three flapwise modes, comprising two asymmetric modes and one symmetric mode, as well as the two edgewise modes and the second group of flapwise modes. The asymmetric modes are further categorized as either yaw or pitch modes, where "yaw" and "pitch" correspond to their respective coupling with the nacelle-yaw and nacelle-pitching motions [25].

Table 5.8: Natural frequencies and shapes description

Mode number	Natural Frequencies [Hz]	Shapes description
1	5.01	1 st Tower FA
2	5.18	1 st Tower SS
3	9.91	1 st Flap yaw
4	11.51	1 st Flap pitch
5	13.37	1 st Flap sym
6	26.18	2 nd Flap yaw
7	32.79	1 st Edge pitch
8	33.49	1 st Edge yaw
9	39.15	2 nd Flap pitch
10	42.50	2 nd Flap sym

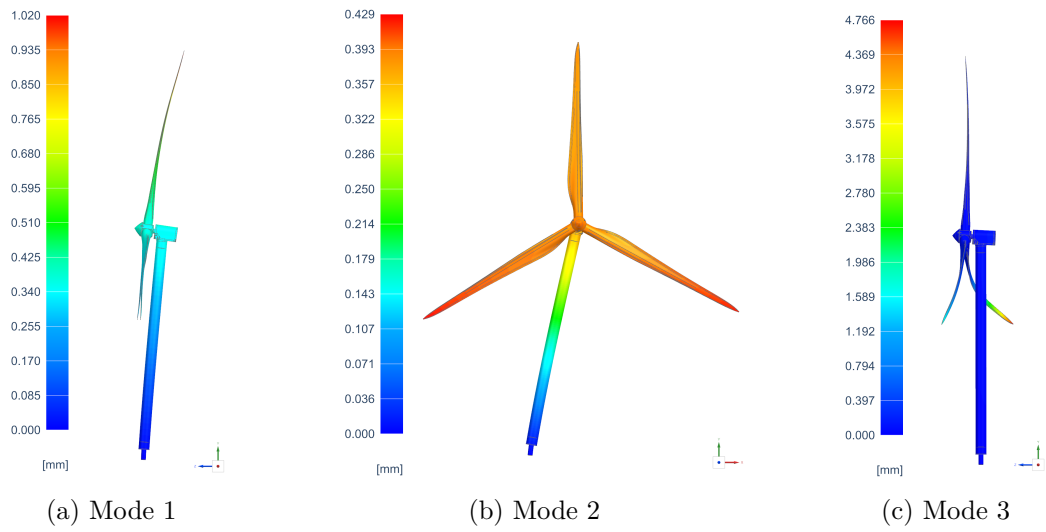


Figure 5.27: Modal shapes of the wind turbine structure (1,2,3)

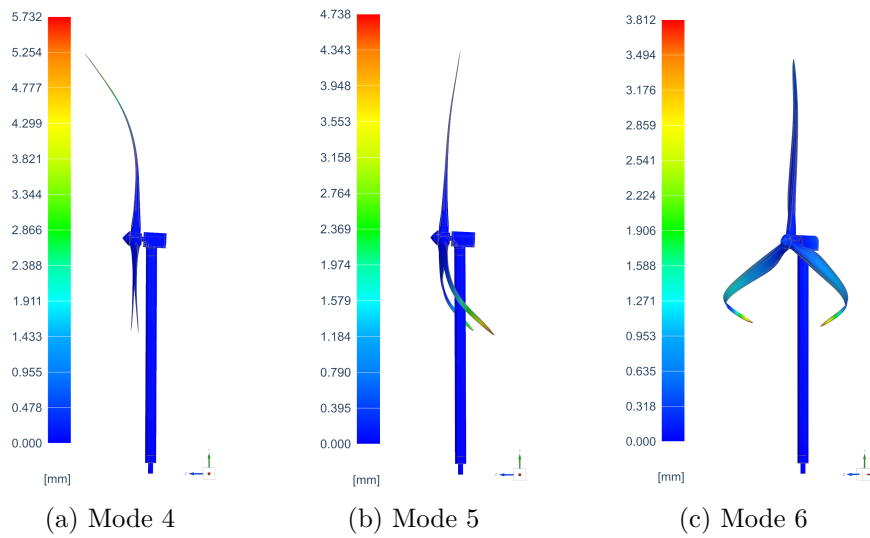


Figure 5.28: Modal shapes of the wind turbine structure (4,5,6)

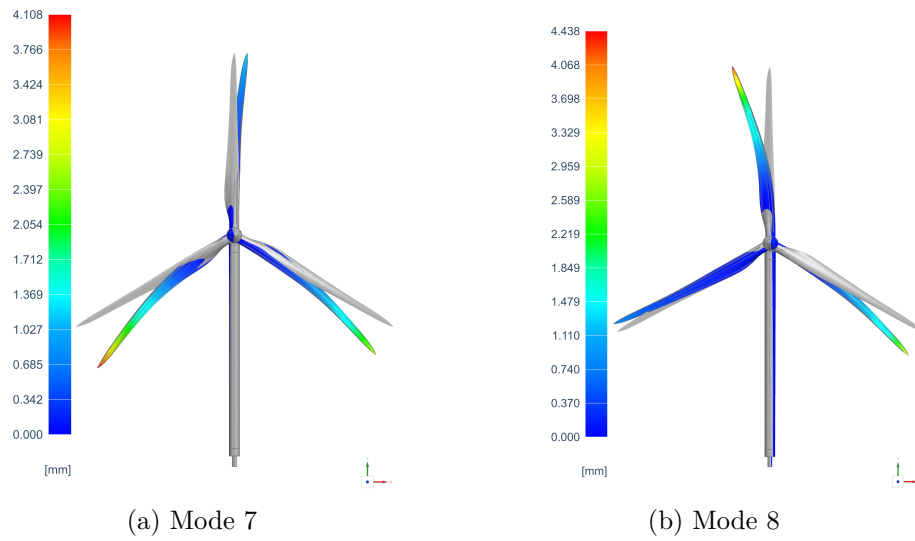


Figure 5.29: Modal shapes of the wind turbine structure (7,8)

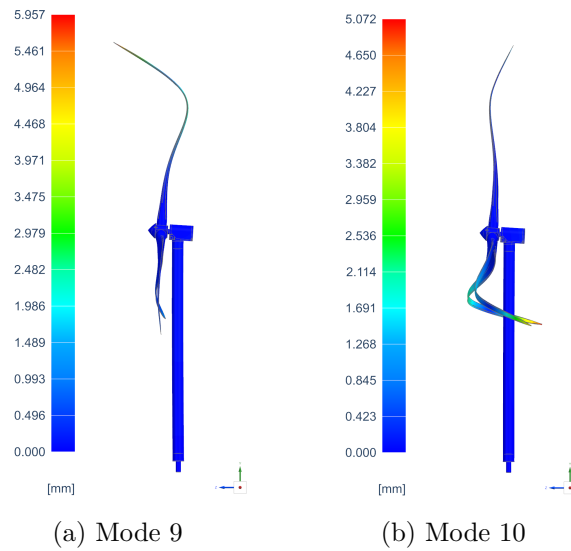


Figure 5.30: Modal shapes of the wind turbine structure (9,10)

Chapter 6

Wind turbine EMA results

To assess the reliability of the results, modal data from a FE analysis are compared to modal test outputs; typically, the frequencies and mode shapes from the model are compared. A proper test must be performed to ensure that the appropriate measurements are made while also reducing testing effort and avoiding unnecessary measurements. Decisions about the number and location of response sensors, as well as the number, location, and orientation of excitation, are made during the design process.

6.1 Wind turbine tower EMA

This section provides a brief overview of the EMA method. The focus will be on the wind turbine tower structure tests, which will be discussed in three parts: pre-test, impact hammer testing, and modal parameter estimation. During the pre-test, the sensor configuration and exciter point selection are established. The impact hammer testing is then performed, followed by the presentation of the modal parameter estimation results.

6.1.1 Pre-Test Solution Process

A pre-test solution must be performed prior to the EMA to determine the optimum locations for the sensors and the exciter. The purpose of pre-test planning is to ensure that, during the modal test:

- The sensors are positioned so that the desired modes are captured and distinguishable from one another.
- The exciters are positioned in such a way that all normal modes of interest are stimulated.

The Pre-test solution is created in Simcenter 3D Pre/Post under the tab correlation. The Pre-Test solution works with two group of nodes: the Candidate DOFs and the required or initial DOF. The solution's algorithm will search for possible sensor locations between the Candidate DOFs. The required or initial DOFs are a set of DOF necessary to initialize the algorithm. Based on the DOF selections made previously, the solver computes optimal sensor and exciter DOFs. To define the Candidate DOFs the best way is to use the command Maximum Spread Node Group and create a group of spatially distributed nodes. The maximum number of nodes is set to 400 and the minimum distance between them is 30 mm. The nodes are selected between the ones on the external surfaces of the model. The Identify High Displacement DOFs command can be used to identify the DOFs with the highest displacements across all target modes of a group of spatially distributed nodes, creating a DOF Set that can

be used to define the candidate sensor locations. After defining the candidate DOFs for the algorithm, the initial or required DOFs can be determined. Using the commands show and hide nodes independently, it is possible to visualise only the nodes in the previously created group, the candidate nodes, and select the required nodes between them. The chosen algorithm will then add nodes to the initial ones from the candidate group.

Two algorithms can be used to define sensor configurations: Min-MAC and Maximum Off Diagonal MAC (MODMAC). They are both sensitive to the initial or required DOFs and generally, do not yield the same results. It is critical to define a suitable set of required/initial DOFs. Then, to define the required or initial sensors, one must select accessible nodes with large deflections and/or at the boundaries of large components. Required Sensors are used by the Min-MAC method. Initial Sensors are used in the MODMAC method. The primary distinction between the two is that Initial Sensors are optional.

Min-MAC Algorithm

The Min-MAC sensor placement algorithm finds the optimal sensor positions by minimizing the MAC matrix's off-diagonal terms. It starts with a required set of DOFs and adds one DOF for uniaxial sensors and three DOFs for triaxial sensors from the candidate DOF set. During the selection phase, the solver inspects a subset of the off-diagonal MAC terms, starting with the biggest off-diagonal member in the MAC matrix. When a new element surpasses the previous one in size, it is added to the tracking list. The algorithm then proceeds in several stages, including computing the MAC matrix, tracking off-diagonal terms, and selecting the DOF that minimizes the tracked elements. The solver loops over all other candidate DOFs to determine which DOF minimizes the off-diagonal elements of the MAC matrix that the solver is tracking. If the DOF selection minimizes the off-diagonal elements, the solver adds this DOF to the sensor selection. The solver stops when the user-specified number of DOFs is reached.

MODMAC algorithm

The maximum off-diagonal MAC (MODMAC) algorithm determines which additional degree-of-freedom (DOF) reduces the off-diagonal MAC values. It adds either one DOF for a uniaxial sensor, or three DOFs for a triaxial sensor from the candidate DOFs to an optional set of initial DOFs until the off-diagonal MAC values are below a given limit, or until the maximum number of DOFs is reached. The solver tracks a subset of the off-diagonal MAC values during the selection process. This subset starts with the current maximum off-diagonal element of the MAC matrix, or the element at position (0,1), when the initial set is empty. As other elements become the maximum off-diagonal element of the MAC matrix, they are added to the tracking list. In the absence of initial DOFs, the solver sets a maximum off-diagonal MAC value to 1.0. The algorithm follows the same passages as the Min-MAC algorithm.

Accelerometers Location

During the test campaign carried out at Siemens, ten triaxial accelerometers and ten uniaxial accelerometers were available for the instrumentation. The MODMAC algorithm is used in the first attempt. The sensor setup for triaxial accelerometers is defined, with the maximum number of degrees of freedom for the algorithm set to 30. After 4 iterations, the solver finds a solution. The MODMAC evolution can be seen to examine the amount of iterations and how the maximum off diagonal value decreases. The Auto-MAC matrix is a major tool. The diagonal members of the matrix should be roughly equal to one, while the off-diagonal elements should be as low as feasible. The findings reveal a maximum off-diagonal value for the MAC

matrix ($MAC_{off-diagonal_{max}}$) of 0.34. However, the final outcome is heavily influenced by the initial DOF set evaluated.

The Min-MAC method is then implemented. This approach produces significantly better results than the previous one, with a $MAC_{off-diagonal_{max}}$ of 0.17. As a result, the MAC matrix is fairly accurate. The accelerometers' locations are easily accessible and situated on the structure's surface. The correct sensors spacing must be verified. The optimal system would have uniformly distributed sensors; the configuration acquired is adequate in this regard. The acquired sensor configuration is depicted in Fig. 6.1.

The MAC matrix related to this configuration is shown in Fig. 6.2. It can be seen that the results are pretty accurate, the diagonal elements are equal to 1 as expected, while the off-diagonal elements are very low, below 0.2 (optimal results should be higher than 0.7 for the diagonal elements and below 0.3 for off-diagonal elements).

To determine where the uniaxial accelerometers are located on the structure, another Pre-Test solution is applied. The nacelle and rotor surfaces are taken into consideration for the Candidate DOFs, excluding the tower, because uniaxial accelerometers are added to the upper portion of the structure to better examine the behavior of these components. The uniaxial sensors configuration shows two accelerometers on each nacelle vertical wall and three accelerometers on the rotor surfaces. Additionally, two sensors are placed on the tower base and one on the tower top oriented as the fore-aft direction to measure possible excitation of the structure in that direction.

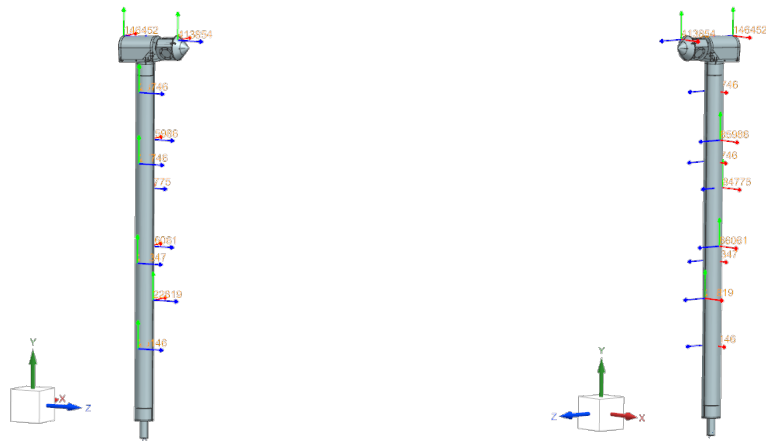


Figure 6.1: Triaxial Accelerometers Configuration

Excitation selection algorithm

Once the response sensor configuration is known, the number, location, and orientation of excitation must be defined in order to conduct a proper test. The selection of optimal excitation points is carried out using the driving point residue (DPR) algorithm. The exciter selection command is then employed to define the sets of candidate DOFs and sensors that will be used by the solver to identify the best exciter points. It is advisable to choose excitation candidates solely from the DOFs defined by the response sensors.

Subsequently, the DPR algorithm is used to generate a sorted matrix of DOFs along with their corresponding DPR values, from which a user-defined number of optimal exciters are identified. This algorithm seeks the most efficient DOF in exciting the different modes. In the

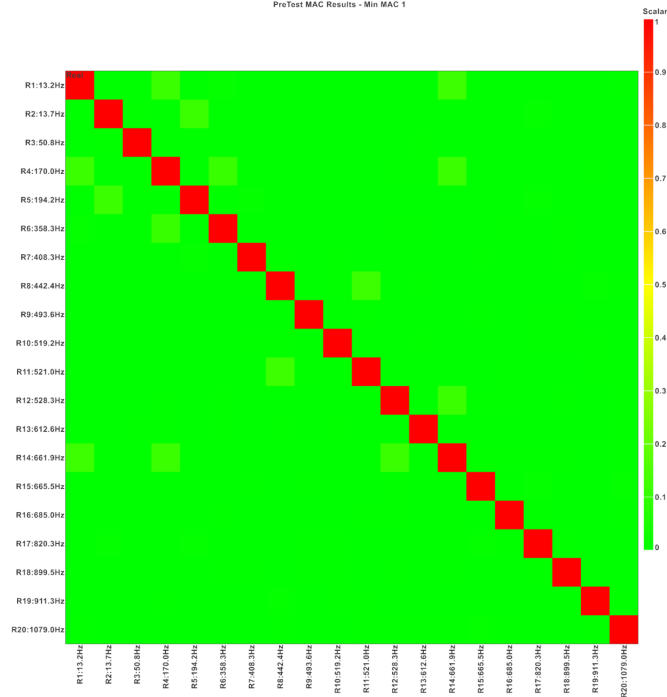


Figure 6.2: MAC matrix - Min-MAC algorithm

FRF model, the residue $r_{ij,k}$ between the location i and j for mode k is computed as:

$$r_{ij,k} = a_k \nu_{ik} \nu_{jk} \quad (6.1)$$

where a_k is a scaling factor and ν_{ik}, ν_{jk} are the modal vector components in both locations. The modal vectors of the structure are real and the residues are imaginary if the structure is proportionally damped. Hence, also the scaling factor is imaginary. The scaling factor is:

$$a_k = \frac{1}{2j\omega_{dk} m_k}. \quad (6.2)$$

The magnitude of the driving point residue is:

$$|r_{ik}| = \frac{\nu_{ik}^2}{2\omega_{dk}} \quad (6.3)$$

where the modal mass m_k is equal to one to scale the modes. To capture the structural acceleration response, the DPR is computed as:

$$|r_{ik}| = \frac{a_{ik}^2}{2} \dot{\omega}_{dk}. \quad (6.4)$$

The solver calculates the driving point residue (DPR) for all selected modes at each node of the exciter input. From these calculations, the algorithm generates minimum, maximum, average, and weighted average DPR values. The weighted average DPR is calculated by multiplying the average DPR by the minimum DPR. This weighted value is low, even if the DPR is high on average, except for one mode. The algorithm then utilizes these computed values to determine the efficacy of exciting the modes of interest from the various nodes in the exciter group. Specifically, the DPR algorithm identifies the DOFs that exhibit a relatively high average value across all modes, thereby enabling the excitation of all modes from these DOFs. Furthermore, the algorithm identifies the DOFs that exhibit a sufficiently high minimum value, thereby enabling the excitation of the weakest mode.

Exciter selection

Firstly, the sensor DOFs are initialised from the ones defined previously in the sensor configuration selection. After that, the DPR algorithm is implemented to determine the optimal exciter location. The algorithm calculates minimum, maximum, average, and weighted average residue values, which can then be plotted; the results for one exciter are shown in Fig. 6.3.

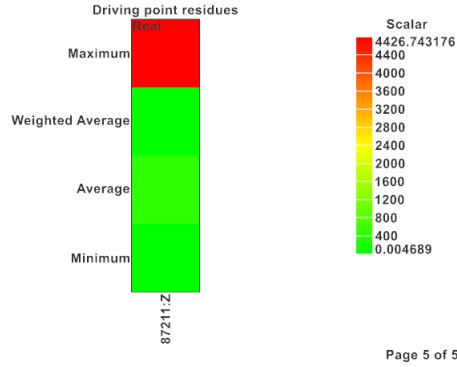


Figure 6.3: DPR algorithm results for a single exciter point

The weighted average value is used as the sorting criterion to select the exciter. It is also possible to sort by minimum DPR to eliminate any DOFs with relatively low minimum DPR values, indicating that one or more modes are poorly excited. The results are the same as for the weighted average, with the sorted node being the 87211:Z (Fig. 6.3), which corresponds to the accelerometer 8 in Fig. 6.4.

More than one excitation point is chosen to ensure that the test captures all modes of interest. The excitation points on the structure are shown in Fig. 6.4; the structure is excited next to the adjacent accelerometers, which are framed in red squares. Driving points are locations where the structure is excited and its response is measured at the same time.

6.1.2 Modal Survey Test: Impact Hammer Test

In a modal survey test, forces are applied to the test object using electrodynamic shakers or a modal impact hammer at carefully selected points. The structure is mounted in well-known clamped boundary conditions during this test. During the test, forces and response accelerations are measured at numerous locations throughout the structure, and FRFs are measured during excitation.

The input force is set by the operator when performing a modal test with electrodynamic shakers, so it is reliable; however, the same cannot be stated when performing a modal test with an impact hammer. Indeed, the ability of the test operator determines the reliability of an impact hammer test. The load cell on the hammer head measures the input force, allowing the input to be analysed to ensure its quality. The impact should be quick enough that the contact is as close to instantaneous as possible. It should also not be too heavy, and double contacts should be avoided.

The ability to tailor the impact pulse to the frequencies of most interest is made possible by multiple hammer tips. A tip with a higher hardness provides a larger frequency content. The tip selection is an important factor in impact hammer tests. The tip must be chosen so that the impact force excites all modes of interest. Increasing hammer velocity (magnitude of impact) may result in unfavorable tip wear while having no effect on the excited frequencies. The FRF of the input force should be relatively flat in the range of interest to assess its reliability.

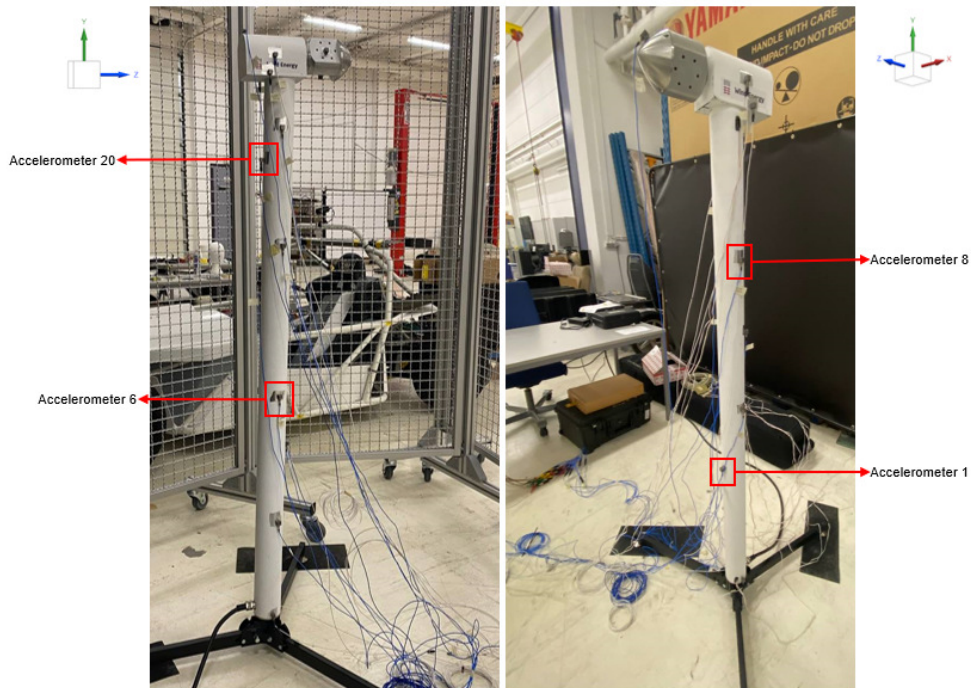


Figure 6.4: Exciter Selection

The mass of the hammer head also influences how long the hammer and structure remain in contact; the greater the mass of the hammers, the longer will be the contact and the lower will be the frequency content. However, adding weight to the hammer head can aid the test engineer by allowing more control over the impact execution. The optimal circumstances for impact testing are determined by the test structure and the operator's skills. Indeed, prior to the test, some attempts are made to determine the most appropriate tip and the appropriate impact force to be applied.

The application site of the impact also has an effect on the test outcomes. The impact application point is known as the driving point, and it is chosen from the previous Pre-Test solution. Following that, the set of potential driving points obtained from the Pre-Test solution must be analysed and the results obtained at different locations compared to determine the best data set that excites more modes of the structure, resulting in more peaks in the driving point's FRF. One or more points can be chosen for the exciter depending on the test object; if multiple spots are selected, the test is classified as roving hammer impact test. The advantages of multiple inputs are:

- better distributed energy over the structure, thus implying homogeneous response;
- repeated roots identification (several modes with same frequency and damping, characteristic of symmetric structure), which is guaranteed if the number of inputs is higher than number of repeated modes;
- test time reduction;
- avoid moving exciters around and thus altering the boundary conditions.

Lastly, the impact hammer test is simpler to implement because it does not require a link to the structure and, when conducted correctly, has no effect on the dynamic behavior of the

structure. Shakers, on the other hand, impact the results since they come into contact with the structure, and the test setup must account for the need to connect the structure to the stingers via rods.

Test setup

The sensors used for the EMA are triaxial and uniaxial accelerometers from PCB Piezotronics. They have a high sensitivity, ($100 \text{ mV/g} \pm 10\%$) and their weight is equal to 5.4 g for the triaxial ones and 4 g for the uniaxial ones. The setup consists of ten triaxial accelerometers and ten uniaxial accelerometers. The triaxial accelerometers are mostly located on the tower, which is where the highest displacements occur. The uniaxial ones are located on the upper part of the structure to capture the displacements of the top components and close to the base to study the structure's boundary condition. In more detail, four uniaxial and one triaxial accelerometer are mounted on the nacelle, one triaxial and three uniaxial are mounted on the rotor and hub of the blades, and the remaining accelerometers are mounted at various heights on the tower according to Fig. 6.10.

Table 6.1: Accelerometers' Model

Model	DOFs	Number	Weight (without cable) [g]
356A32	Triaxial	1-10	5.4
333B30	Uniaxial	11-20	4



(a) Triaxial accelerometer



(b) Uniaxial accelerometer

Figure 6.5: Accelerometers

The accelerometers are glued to the structure, and a layer of aluminum tape is positioned between the structure and the sensor to protect the surface from the adhesive's damaging effects.

As seen in Fig. 6.6, the hammer is a modally tuned impulse hammer with force sensor and tips. The force range varies from 0 to 500 lbf. The sensitivity is $2.2 \text{ mV/N} (\pm 15\%)$. The hammer total mass is 0.16 kg.

To prevent energy wastage, the input force should only be strong enough to excite the frequency range of interest. If required, a further mass can be added on the hammer head. The mass of the hammer head, however, also has an impact on how long the hammer and the structure are in contact. As the hammer mass increases, the contact lasts longer and has a lower frequency content.

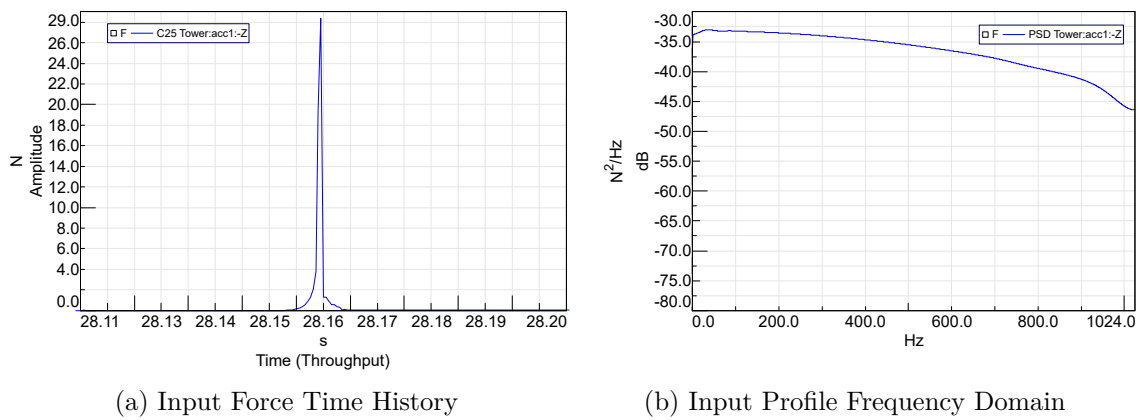
In order to determine the best configuration for the hammer, various conditions are compared, and the best input excitation is determined by comparing the input FRFs. Several tips are available and the input force PSD can be used to confirm the tip selection. It is necessary for the input PSD to be fairly flat over the desired frequency range. The final configuration is a hammer with a medium tip (a white tip) but no additional mass on the hammer head.

The hammer's input force features the time history plotted in the first graph in Fig. 6.7a. Under the input plot, the structural response in terms of accelerations is shown in Fig. 6.8a. Fig. 6.7b shows that a correct excitation could be achieved via the applied force. Indeed, the



Figure 6.6: Impact Hammer

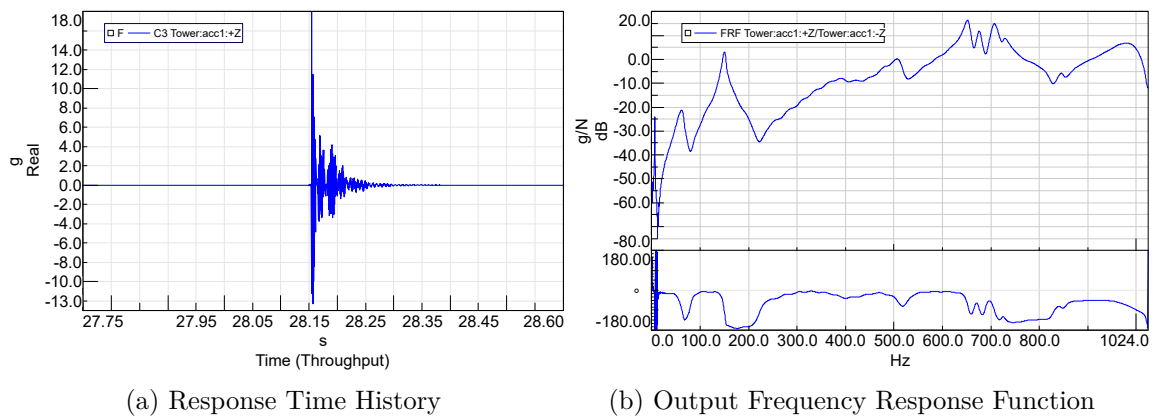
input frequency spectrum should be reasonably flat over the analyzed frequency range with a maximum of a 30 dB roll-off, diminishing only towards the end. In Fig. 6.7b the decay is equal to 15 dB until 1024 Hz. The FRF should be as clear as possible, as seen on the lower right (Fig. 6.8b).



(a) Input Force Time History

(b) Input Profile Frequency Domain

Figure 6.7: Input Profile



(a) Response Time History

(b) Output Frequency Response Function

Figure 6.8: Response Profile

The driving point is the location where the impact is provided and an accelerometer measures

the response. The phase of this point should always be between 0 and 180° or between 0 and -180°. For instance, in Fig. 6.8b, the phase is always below 0° and falls within the range of 0 -180°. The FRF of this point should always be clear with anti-resonances occurring between each resonance. It's important to choose the excitation sites carefully. In the driving point FRF, each mode must be present and spatially separated. If the driving point also happens to be a nodal point, the corresponding mode is not excited.

The accelerometers are connected to the Simcenter SCADAS via cables. The Simcenter SCADAS is a data acquisition hardware platform. The SCADAS hardware features built-in signal conditioning to power transducers. The analog signals of the transducers are collected at speeds up to 200 kHz per channel. Simcenter SCADAS Mobile comes with two source signal generators, two tachometer inputs, digital CAN bus input, and ethernet connection for use with PC. Depending on the frame size, there can be one (1) to nine (9) slots available for input cards.

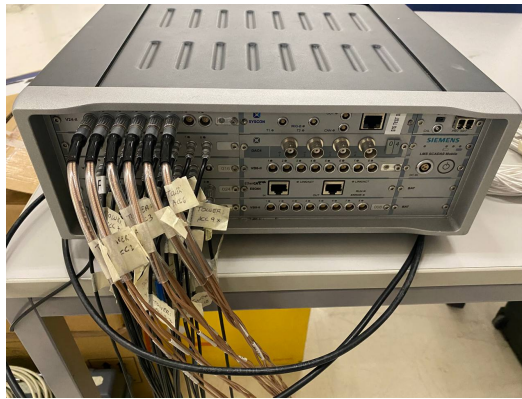


Figure 6.9: Simcenter SCADAS Mobile

Simcenter Testlab is the acquisition software developed by Siemens. In the channel set-up, all the sensors and the inputs are itemized. The following table shows how the Simcenter Testlab acquisition parameters are configured. The maximum frequency for the FE model is 819 Hz, which corresponds to the twentieth mode, so 1024 Hz was chosen as bandwidth.

Table 6.2: Testlab Acquisition Parameters

Bandwith [Hz]	Spectral lines	Acquisition time [s]	Resolution	Window	Average
1024	2048	2	0.5	Exponential	10

In the geometry, the response location is set by creating nodes for each sensor and defining the measured response direction. It is particularly important that the name of each sensor in the channel setup is the same of the corresponding node in the geometry. Otherwise there will be problem in the analysis of the results and it will not be possible to animate the mode shapes.

The geometry must include both points where the input force is applied and points where response is needed for mode shape visualization and the correlation with the analytical model. The geometry of the test object created on Testlab is displayed in the next image (Fig. 6.10). The red points are the accelerometers, while the green points are geometrical points to aid in the visualization of the results.

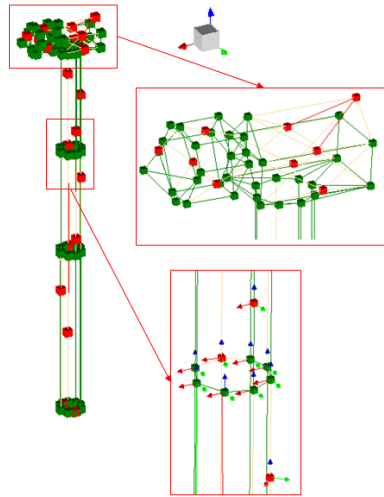


Figure 6.10: Testlab Geometry

6.1.3 Test Results

The outcomes are then depicted on the following graphs in terms of the driving point FRF and the coherence function. The functions for four distinct driving points—accelerometers 1, 6, 8 and 20—are overlaid on the plots. Fig. 6.4 already showed the corresponding accelerometers. The consistency between several measurements is assessed by the coherence function. A measurement done with consistency has a value of 1. This value often decreases in the anti-resonance frequencies.

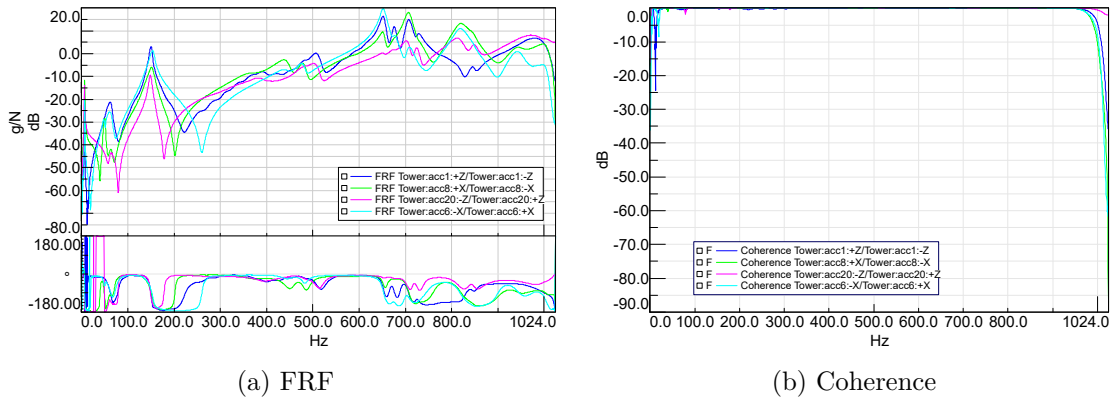


Figure 6.11: FRF and Coherence of 4 driving points

Once the test is performed, the results in terms of natural frequencies, damping ratios and mode shapes are estimated from the data acquired using curve fitting. Different methods exist, they are divided in time domain and frequency domain methods. In this case, the adopted algorithm relies on a least square method, a statistical procedure to find the best fit for a set of data points by minimizing the sum of the offsets or residuals of points from the plotted curve.

The Simcenter PolyMax or Polyreference Least Squares Complex Frequency Domain method is the name of this technique. First, a stabilization diagram, depicted in Fig. 6.12a, is used to determine the frequencies, damping ratios, and participation factors. The FRF sum of all measurement points (red curve) and the Imaginary MIF (green curve) can be seen on the

diagram. The letters denote the repeatability of a specific potential modal solution, they have the following meaning: "o": new pole, "f": stable frequency, "d": stable frequency and damping, "v": stable frequency and eigenvector, "s": all criteria stable.

The method's benefits include the development of extremely clear stabilization diagrams that make it very easy to identify the system's very stable poles as a function of the specified system order. As a result, the stabilization diagrams are simple to analyze and the method can be automated and applied to complex structures like high-order and/or highly damped systems with large modal overlap as well as noisy data set [22].

As previously mentioned, four tests were carried out on various accelerometers, and using the Polymax algorithm for the estimation of the modal parameter, stabilization diagrams for each of them were obtained, as shown in Fig. 6.12. When the structure is excited in the Z direction, all of the poles in this direction are determined, but the poles in the XY plane are not. Similarly, the mode shapes in the YZ plane are not excited when the structure is excited in the X direction.

The test results in the Z direction are coupled with the results in the X direction to determine all the frequencies and mode shapes of the structure.

Fig. 6.13 displays the stabilization diagram that took into account both the input on the accelerometer 6 with input direction X and the input on the accelerometer 1 with input direction Z. This diagram was chosen for the modal parameter estimation as a result of the earlier considerations because it displays more stable poles than the others. Indeed, the diagram contains both of the f_n frequencies at 148.2 and 153.2 Hz, whereas in the diagrams where only one direction was excited, only one pole was stable. Since the poles at 441 and 479 Hz are related to the same mode shape, only the more stable pole at 479 Hz was chosen for the final estimation.

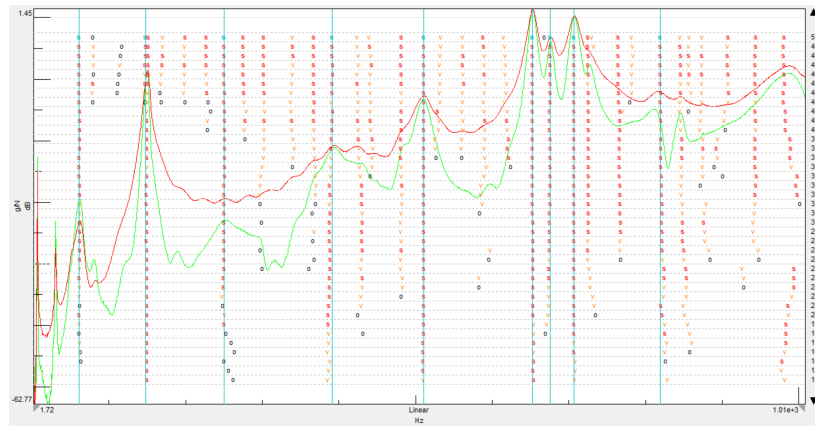
The configuration of 10 triaxial and 10 uniaxial accelerometers, as seen from the Auto-MAC matrix, is sufficient to analyze the mode shapes up to 1000 Hz, as previously demonstrated by the Min-MAC in Fig. 6.2. The poles were manually selected and the values for the frequency and damping ratios are listed in Table 6.3.

To acquire the first two stable poles of the structure at 6.55 and 7.02 Hz, the stabilization order has been raised to 120.

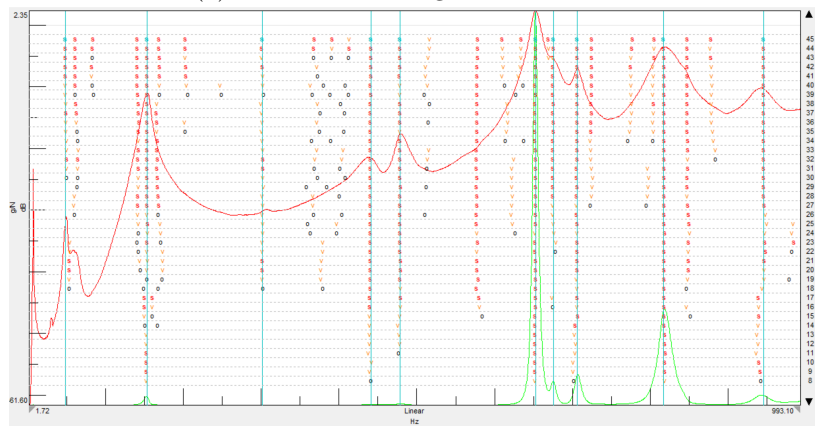
Table 6.3: Natural frequencies and damping ratios

Modes	Natural frequency [Hz]	Damping ratio [%]
1	6.55	1.53
2	7.02	1.29
3	48.69	2.85
4	148.21	2.65
5	153.26	3.30
6	250.87	5.66
7	391.65	3.66
8	479.25	1.79
9	509.83	2.06
10	577.09	3.26
11	653.03	1.03
12	675.80	0.80
13	706.77	1.05
14	724.97	0.89
15	819.17	2.16
16	945.94	1.97

After choosing the stable poles, a second least squares step is used to evaluate the mode shapes.



(a) Stabilization Diagrams Z direction



(b) Stabilization Diagrams X direction

Figure 6.12: Stabilization Diagrams for single input configurations

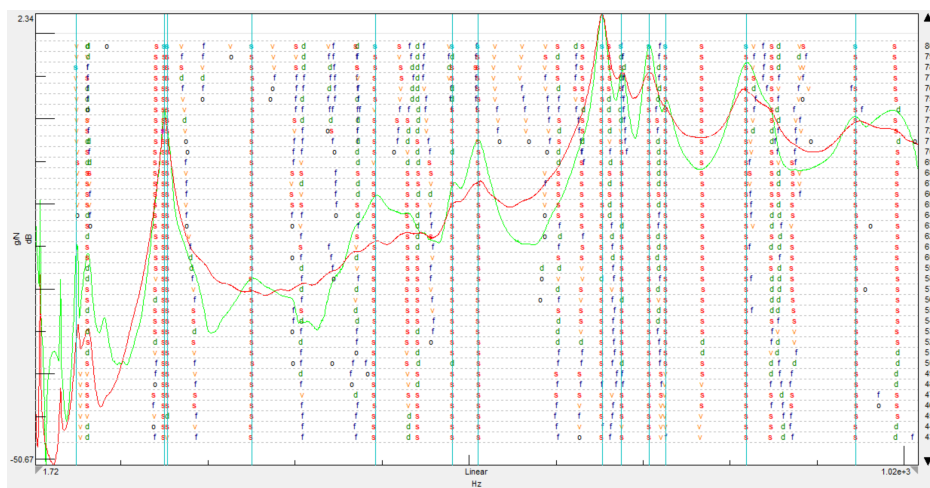


Figure 6.13: Stabilization Diagram XZ Input

Fig. 6.15 compares the synthesized and measured FRFs for two examples; the correlation index is fairly high, indicating that the correlation is good.

The design of tower structures can be categorized into three types based on their stiffness

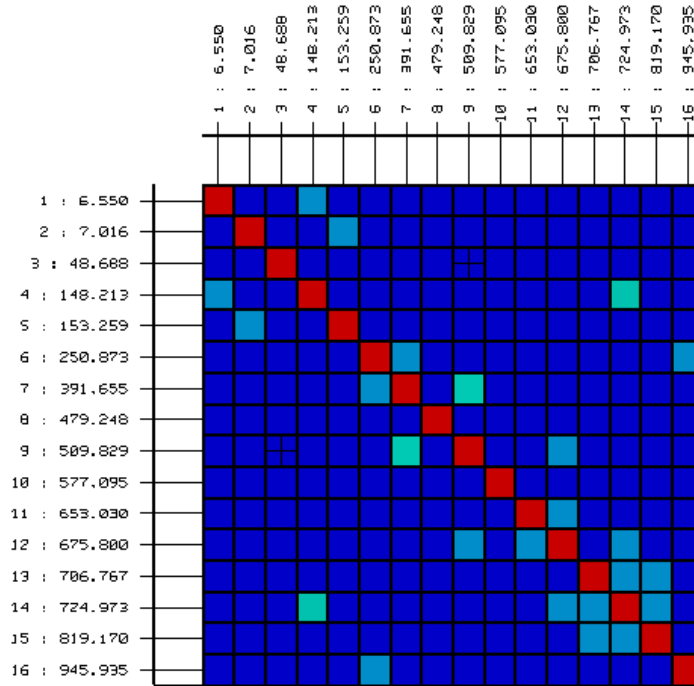


Figure 6.14: Auto-MAC XZ Input

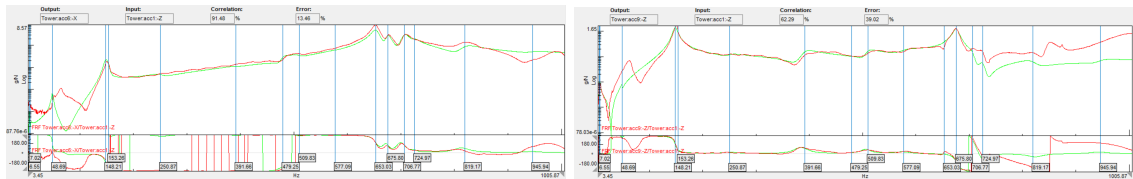


Figure 6.15: Synthesized and Measured FRFs

properties, namely "soft-soft," "soft-stiff," and "stiff-stiff" zones. The classification of a tower into one of these zones is dependent on its first bending frequency, with two critical frequencies, the first order of rotor speed (1P), and the blade passing frequency (3P). The "soft-soft" zone is characterized by frequencies lower than 1P, the "soft-stiff" zone falls between 1P and 3P, while the "stiff-stiff" zone is associated with frequencies above 3P. The "soft-stiff" zone, where the tower exhibits a balance between stiffness and cost-effectiveness, is considered desirable. In this study, the first bending frequency of the tower structure is measured at 6.55 Hz. The rotor speed required for the tower to fall into the "soft-soft" region, where the tower is considered too flexible, is at least 393 rpm. Conversely, to fall into the "stiff-stiff" region, where the tower is considered too rigid and consequently more expensive, the rotor speed must be lower than 131 rpm. These results are somewhat inconsistent due to the fact that the wind turbine tower is made of a composite material and is much lighter than a real wind turbine tower. Nonetheless, evaluating the structural classification of the tower as per the existing literature is considered valuable for the dynamic characterization of the structure. Finally, the test mode shapes obtained are displayed in Fig. 6.16, 6.17, 6.18.

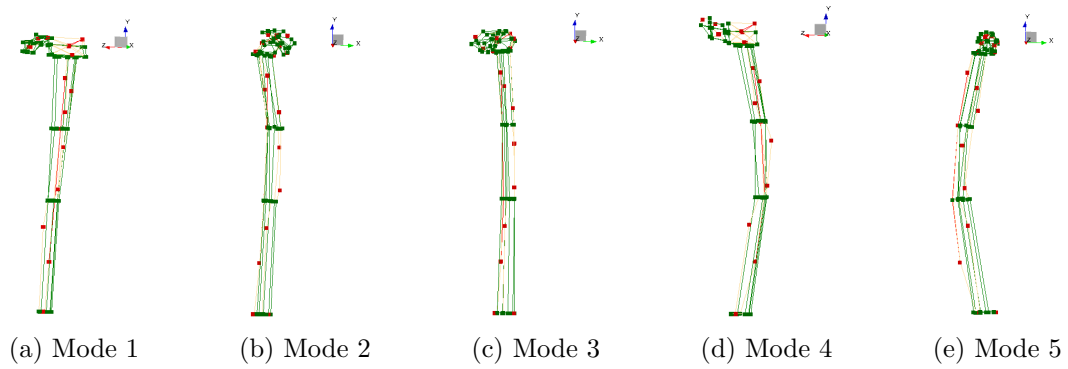


Figure 6.16: Modal shapes of the wind turbine tower structure (1,2,3,4,5)

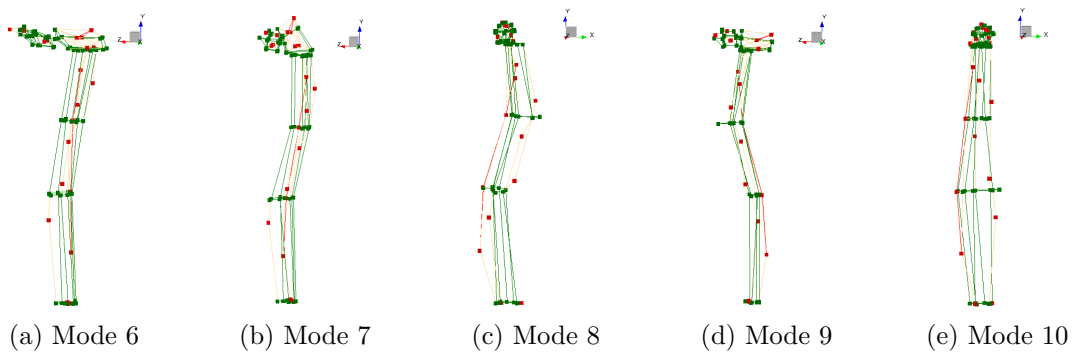


Figure 6.17: Modal shapes of the wind turbine tower structure (6,7,8,9,10)

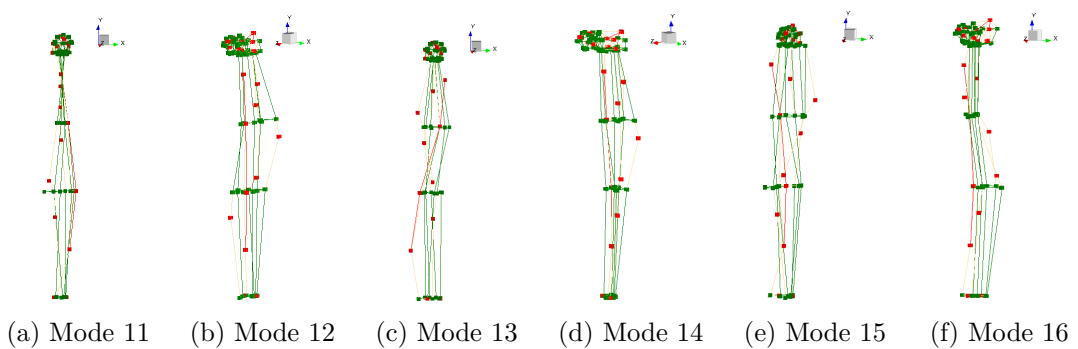


Figure 6.18: Modal shapes of the wind turbine tower structure (11,12,13,14,15,16)

6.2 Wind turbine EMA

This section will discuss the EMA of the entire wind turbine system, including the test setup, the methodology and the results obtained.

6.2.1 Test setup

The EMA of the entire wind turbine system is conducted. The instrumentation follow what previously implemented for the tower EMA, with triaxial and monoaxial listed in Table 6.1 and the impact hammer in Fig. 6.6. The tip used for the hammer is a medium tip.

In total, 15 accelerometers are placed on the wind turbine. Four accelerometers are placed on each blade, two triaxial and two uniaxial, the uniaxial accelerometers measure the flap-wise direction, the sensor set-up is shown in Fig. 6.19.

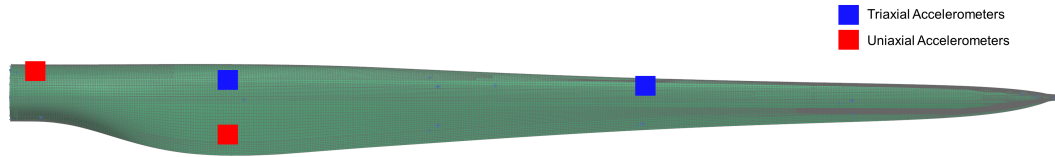


Figure 6.19: Wind turbine blades' sensor configuration

The tower sensor configuration is defined based on similar studies found in literature [47],[48]. Three triaxial accelerometers are located on the tower, at three different height: bottom, middle and top. In addition to the accelerometers, six strain gages are placed on the tower, three uniaxial strain gages and three rosettes. In correspondence of each accelerometers a uniaxial strain gage and a rosette is positioned, on the opposite side of the tower. The sensor configuration is shown in Fig. 6.20, 6.21.

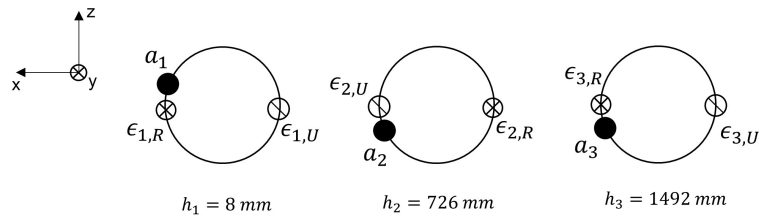


Figure 6.20: Tower sensor configuration

A roving hammer impact test is performed. The impact excitation is applied on three driving points: the tower top accelerometer and the two triaxial accelerometers on the vertical blade and on the right blade at the maximum chord. In accordance with established criteria, the selection of excitation points is based on ensuring that the power spectral density (PSD) of the input remains fairly flat across the relevant frequency range, while exhibiting a roll-off that does not exceed 30 dB. This condition is depicted in Fig. 6.22. The PSD of the accelerometer located at the tower top demonstrates a favourable result across the relevant frequency range, with a decay of 8 dB. Comparatively, the PSD of the excitation on the blades exhibits a decay of 25 dB, which remains within the permissible range of 30 dB.

The acquisition parameters in Testlab are set as before and are listed in Table 6.4.

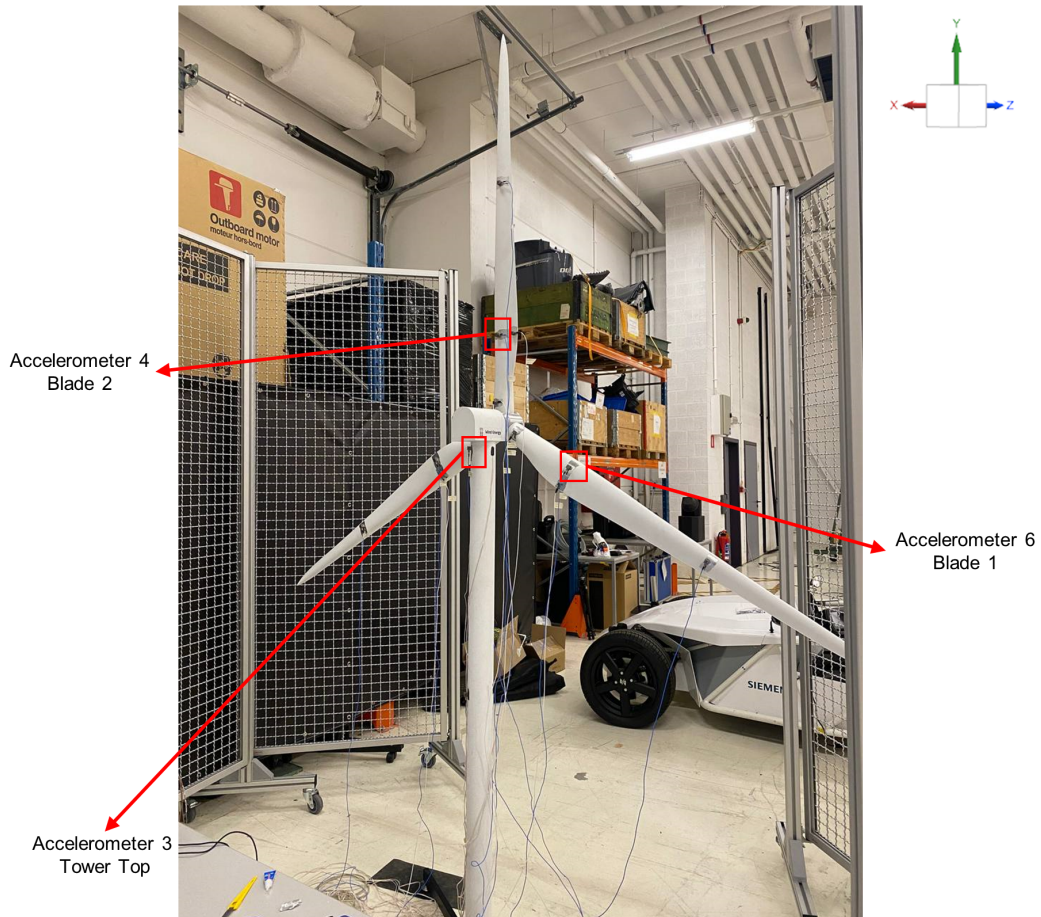


Figure 6.21: Wind turbine measurement set-up

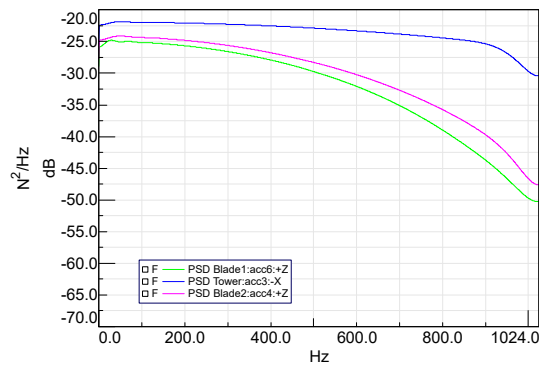


Figure 6.22: Input Profile Frequency Domain

Table 6.4: Testlab Acquisition Parameters

Bandwidth [Hz]	Spectral lines	Acquisition time [s]	Resolution	Window	Average
1024	2048	2	0.5	Exponential	10

6.2.2 Test results

The FRF obtained from the tests for each driving point are depicted in Fig. 6.23a, Fig. 6.23b shows the coherence for the three measurements. The FRFs are clear and the phase is always between 0° and -180° , while the coherence is equal to 1 in the entire frequency range, except in the anti-resonance frequency where a decay is present, as expected.

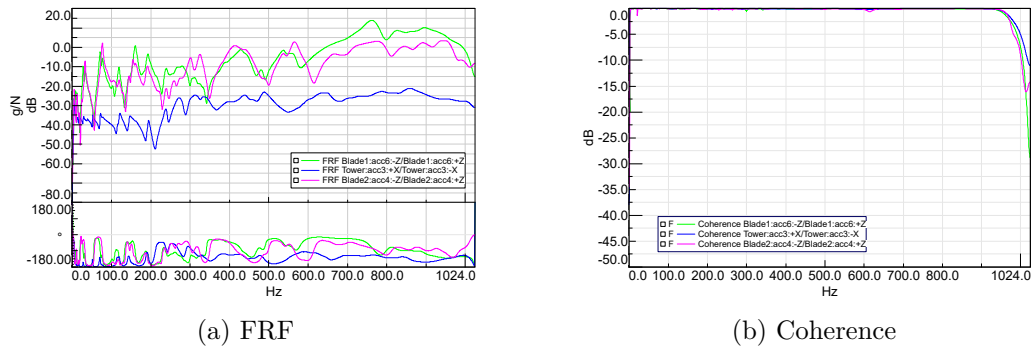


Figure 6.23: FRF and coherence of the three driving points

The modal parameters are extracted from the data acquired using Simcenter PolyMax algorithm. Fig. 6.24 illustrates the stabilization diagram from the combination of two measurements: excitation on accelerometer three on the tower top station and on accelerometers six on the right blade (Fig. 6.25). This combination of test data is selected because it leads to a higher number of stable poles found and a more clear stabilization diagram. As previously noticed from the numerical modal analysis, the first 10 modes of interest are comprised in a frequency range between 5 and 60 Hz. Therefore, the modal parameter estimation is conducted in this bandwidth. The poles were manually selected and the frequency and damping ratio values for the first 10 mode shapes are listed in Table 6.5.

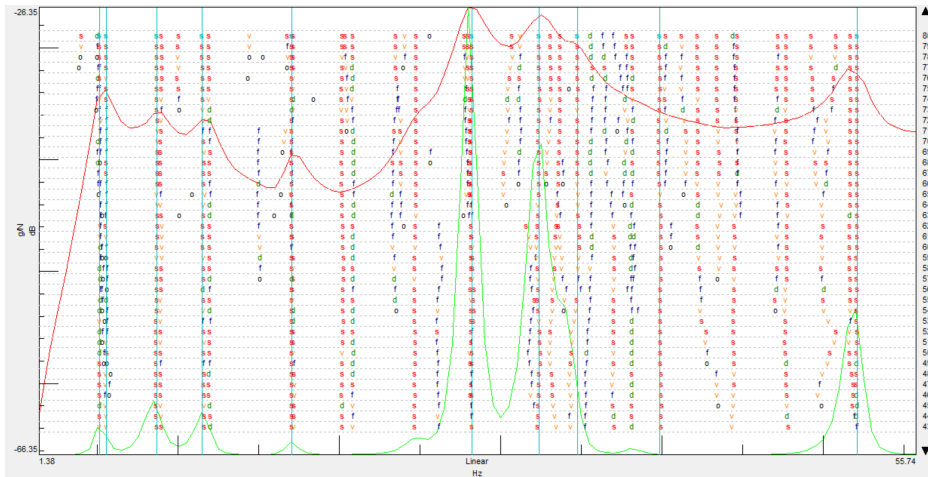


Figure 6.24: Stabilization diagram

After the selection of the stable poles, a second least square step is applied to extract the mode shapes. The first-order flap-wise modes of the wind turbine results into three modes, two asymmetric modes and one symmetric mode. A high frequency resolution is necessary to capture these modes, because they are closely spaced. The auto-MAC correlating the test mode shapes with themselves is calculated after the modal parameter estimation and shown

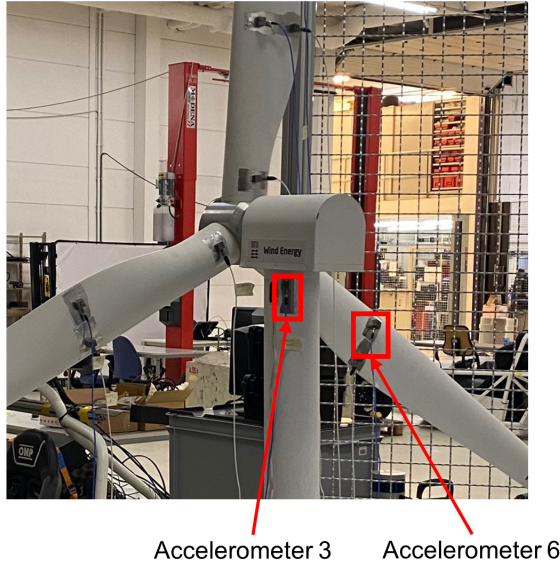


Figure 6.25: Driving points

Table 6.5: Test modal parameters

Mode number	Natural Frequencies [Hz]	Damping ratio [%]	Shapes description
1	5.12	1.70	Tower FA
2	5.55	1.35	Tower SS
3	8.70	6.82	1 st Flap yaw
4	11.61	4.45	1 st Flap pitch
5	17.03	0.33	1 st Flap sym
6	28.19	3.10	2 nd Flap yaw
7	32.28	2.70	2 nd Flap pitch
8	34.85	1.37	1 st Edge pitch
9	38.11	1.11	1 st Edge yaw
10	52.08	0.73	2 nd Flap sym

in Fig. 6.26. It demonstrates that the sensor configuration is sufficient for the study in the frequency range of interest as all the mode shapes are captured with good accuracy. The diagonal values are unity because they show the correlation of the mode with itself. The off-diagonal elements represent the MAC between different modes. Some off-diagonal elements are close to one, showing that some mode shapes are similar to each other. These mode shapes are the three ones of the first and second-order flap-wise modes, which are listed in Table 6.6. This is because of the spatial aliasing due to the few numbers of accelerometers. The discrete number of accelerometers on the blades leads to a discrete number of response point and the difficulty to capture the high-order flap-wise modes with great accuracy.

Table 6.6: Off-diagonal elements with high MAC value

Correlated Modes			
Frequency [Hz]		Shapes description	MAC
8.70 Hz	28.19 Hz	1st and 2nd Flap yaw	0.66
11.61 Hz	32.28 Hz	1st and 2nd Flap pitch	0.54
17.03 Hz	52.08 Hz	1st and 2nd Flap sym	0.90

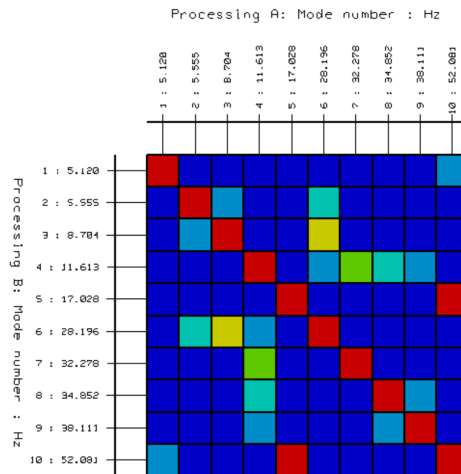


Figure 6.26: Auto-MAC matrix

Finally, the test mode shapes obtained are displayed in Fig. 6.27, 6.28.

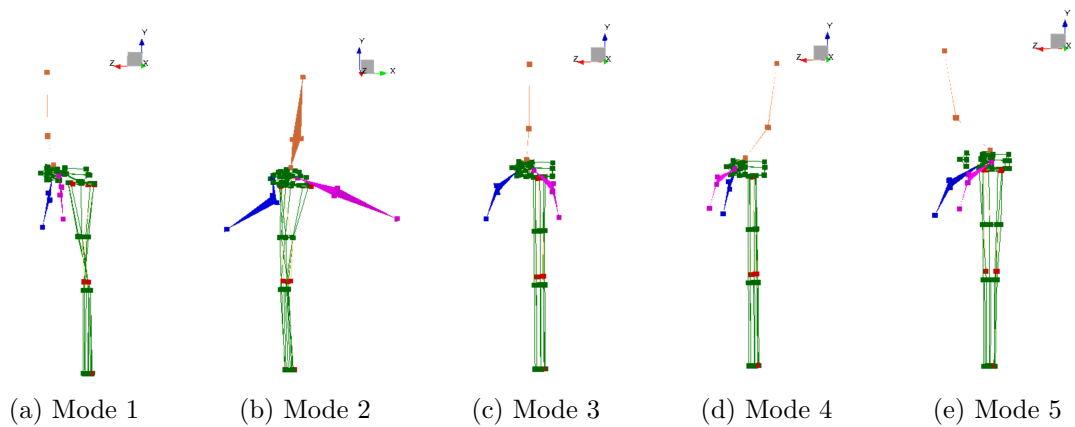


Figure 6.27: Modal shapes of the wind turbine (1,2,3,4,5)

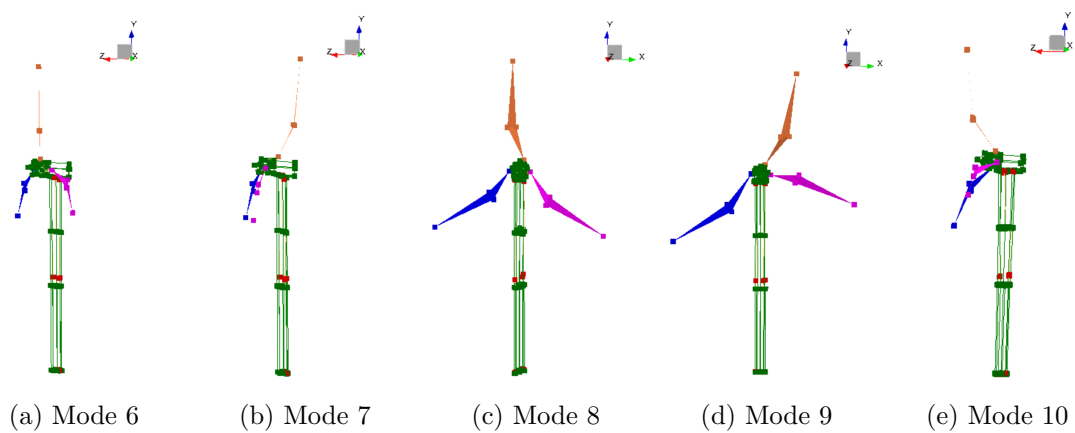


Figure 6.28: Modal shapes of the wind turbine(6,7,8,9,10)

Chapter 7

Wind turbine OMA results

Operational Modal Analysis (OMA), also known as output-only modal analysis allows for the estimation of modal parameters of a structure under operating conditions. The main difference and advantage when compared to EMA is that it does not require knowledge of the input forces, thus the structure can be tested in operational conditions or in other situations where the input is unknown.

This technique can be used to extract modal parameters for numerical model validation and improvement as well as monitoring systems in operating conditions. A forthcoming application of this methodology is the possibility to use a validated numerical model to predict in advance damages and apply SHM techniques. Virtual damages can be introduced in the model and the generated data compared to the modal parameters extracted from the structure in nominal conditions. Therefore, the obtained outcomes can be used to monitor the wind turbine in operation and study the risk of failure during its lifetime with reliability.

7.1 Wind turbine OMA

In this chapter the operational measurements conducted on the small-scale wind turbine are described. OMA is used to extract the modal parameters while the blades rotate and the results are discussed and compared to those obtained previously from EMA.

7.1.1 Test setup

The tower is instrumented as in the EMA for the modal parameter estimation of the tower structure without the blades. The sensor configuration is made up of sixteen accelerometers, nine triaxial and seven uniaxial. Eight triaxial accelerometers are located on the tower and one on the nacelle. The uniaxial accelerometers are mostly placed on the upper part of the structure to better capture the nacelle deformation and on the base of the tower to study the constraint behavior. Six strain gages are added on the tower on three station at different height, the configuration is the same presented in the entire wind turbine EMA (Fig. 6.20): two at the tower top, two at the middle and two at the tower bottom. The blades are not instrumented. Fig. 7.1a shows the sensor configuration. The accelerometers and strain gages are connected to the SCADAS via cables (Fig. 7.1b). The acquired data are transferred from the SCADAS to the PC connected to the data acquisition system and post-processed in Simcenter Testlab.

The acquisition parameters in Simcenter Testlab Signature are reported in Table 7.1. The wind turbine blades rotation is controlled through an electric motor inside the nacelle. The



(a) Sensor configuration



(b) Scadas

Figure 7.1: Test set-up

motor is a brushless DC motor controlled by a stepper motor driver. The speed is set manually on the driver and transferred from the motor to the blades.

Table 7.1: Testlab acquisition parameters

Bandwidth	Resolution	Frequency lines	Window
800 Hz	0.5	1600	Hanning

The OMA is conducted with the blades rotating at constant speed and increasing the speed during the acquisition. The electric motor in the nacelle rotates and transfers the rotation to the blades.

7.1.2 Run-up test

A run-up test is conducted to study the "end-of-order" phenomena. The FRF might present some peaks that are not characteristic of the structure own dynamics, but are due to the verification of a repetitive event that happens several times per cycle and affects the structural dynamics. These cycle events that repeat the same amount of times every cycle are referred to as orders. They may be due to external events, such as the motor operation and transmission. The "end-of-order" phenomena consists in the presence of a order component that suddenly stops at the maximum speed. As a result, the identification of the modal parameters might be wrong if the data are not carefully analyzed. Thus, performing this type of tests allows to avoid wrong interpretation of the findings. This is the main weakness of the OMA technique:

it can estimate the physical poles of the system, but on top of them it also identifies the "end-of-order" poles which are physically not present in the system. In this case the "end-of-order" poles will be ignored a-posteriori, but this is not always possible, in particular when there are many orders and they influence the modes identification close in frequency, reducing the confidence in the identified modal model [28].

The run-up test is conducted starting from zero rpm, increasing the speed to 10 rpm, keeping it constant for 15 seconds, increasing the speed of 5 rpm and keeping it constant for 15 seconds again. The test ends when the speed reaches 30 rpm and it is kept constant for 15 seconds. The blades experience the following speed during the test: 0, 10, 15, 20, 25, 30 rpm.

From the colormap in Fig. 7.2a, the presence of a peak at a frequency proportional to each speed is highlighted. In the intervals where the speed is increasing, also the peak moves to higher frequency linearly with the velocity. Thus, it is demonstrated that this peak is an order, related probably to the motor and it should be excluded from the modes identification. The peaks appear at the following frequencies: 100 Hz, 150 Hz, 200 Hz, 250 Hz, 300 Hz for 10 rpm, 15 rpm, 20 rpm, 25 rpm, 30 rpm, respectively. The "end-of-order" phenomena is also confirmed by the presence of these characteristic peaks stopping suddenly when the test ends. For this reason, these peaks are also visible in the FRF curve fitted by means of Operational PolyMax and they appear as sharpest peaks.

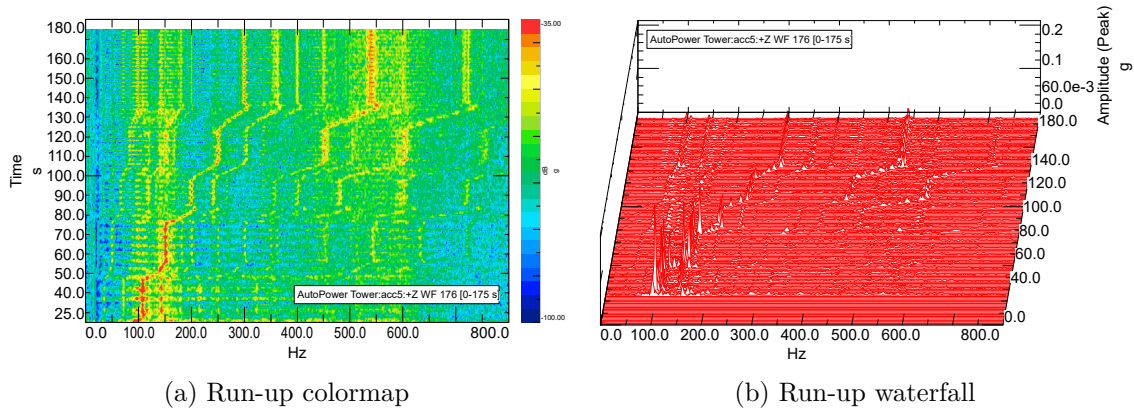


Figure 7.2: Run-up test results

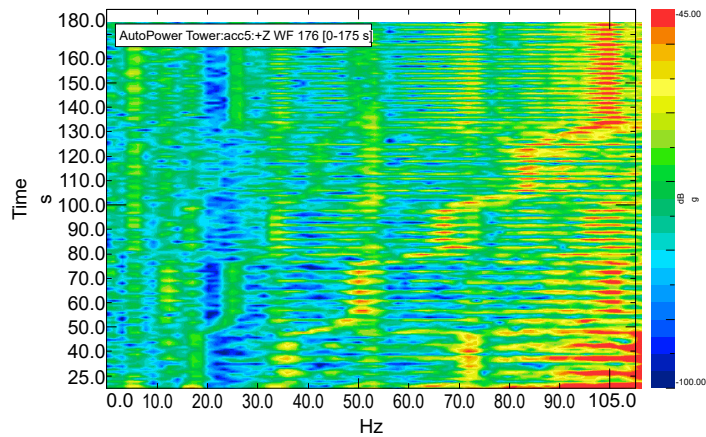


Figure 7.3: Run-up colormap - restricted bandwidth

In conclusion, these "end-of-order" peaks must be excluded from the modal parameter estimation. Moreover, considering that the modes of interest are included in the frequency range below 60 Hz, the tests at low speeds might be highly affected by the presence of these sharp peaks at low frequencies. For instance the speed test at 10 rpm that presents a peak at 100 Hz, thus corrupting the results obtained from the curve fitting. Fig. 7.3 shows the colormap in the restricted bandwidth where the primary wind turbine modes are collocated. Also in this bandwidth, sharp peaks due to orders can be found, which may affect the modal parameter estimation. Since there is a sharp peak at 100 Hz in correspondence with the 30 rpm speed, also the test results at this speed may be corrupted due to the presence of this order. For this reason, it is better to analyze the results from other speed test, such as 20 rpm, where the peak is smaller and switched to higher frequency with respect to the modal parameters to be identified. In the next paragraph, the results obtained from different constant speed test will be discussed and compared, then the modal parameters will be extracted.

7.1.3 Constant speed test

To extract the modal parameters, several tests are performed at constant speed. The speed is set manually on the stepper motor driver through an handle. The first test is conducted at 10 rpm. The data acquired are the time histories collected during operational conditions, that are then processed in the Simcenter Testlab operational data collection tab into auto and cross-spectra; the accelerometer 8, placed at the tower top, is chosen as reference for the correlations and spectra computation. To calculate the crosspower functions, the number of time lags and the window must be defined; the number of time lags indicates the number of steps in the time domain and obviously affects the frequency resolution: if the number increases the resolution is higher and the time of data is higher; for this case study, this parameter is set to 4096 time lags, thus the resolution is 0.391. The exponential window is applied to force the signal to zero in the frequency range of interest. For this tests the necessary window is equal to 1%. The spectra can be analyzed by means of a curve-fitting method such as Operational Polymax to extract the modal parameters.

The stabilization diagram for the 10 rpm speed test is illustrated in Fig. 7.4. As expected from the conclusions of the previous paragraph there is a sharp peak at 100 Hz. This peak is associated to an "end-of-order" phenomena, as a result the bandwidth for the curve fitting is restricted to the left band, between 2 Hz and 57.7 Hz, as shown in Fig. 7.5. The stabilization diagram is much clearer in the limited bandwidth considered and the stable poles associated to physical modes of the structure (blue lines) can be easily selected.

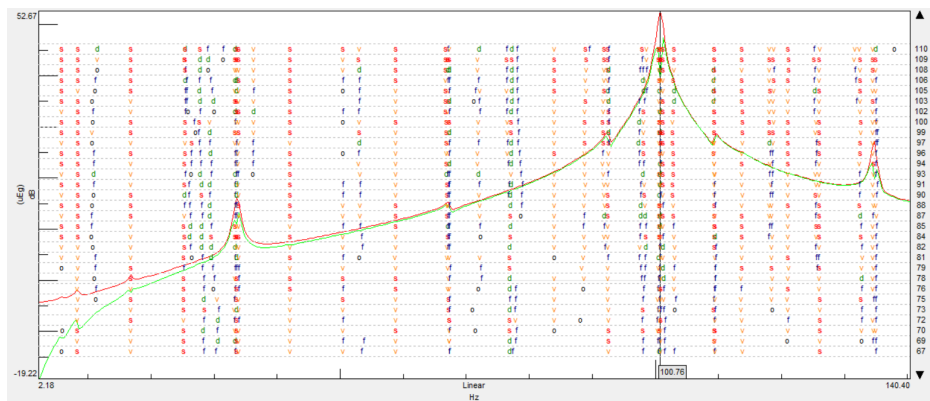


Figure 7.4: Stabilization diagram (10 rpm)

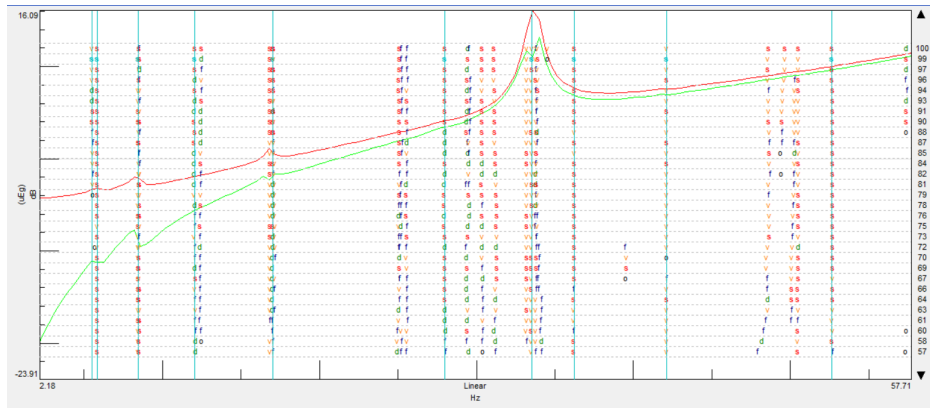


Figure 7.5: Stabilization diagram (10 rpm) - restricted bandwidth

In order to avoid the 100 Hz peak, more tests are conducted at higher speeds. In total, five tests are executed and the speeds are: 10 rpm, 15 rpm, 20 rpm, 25 rpm, 30 rpm.

Fig. 7.6 and 7.7 illustrate the stabilization diagram for the tests at 20 and 30 rpm. The band of interest is always limited to 2-60 Hz.

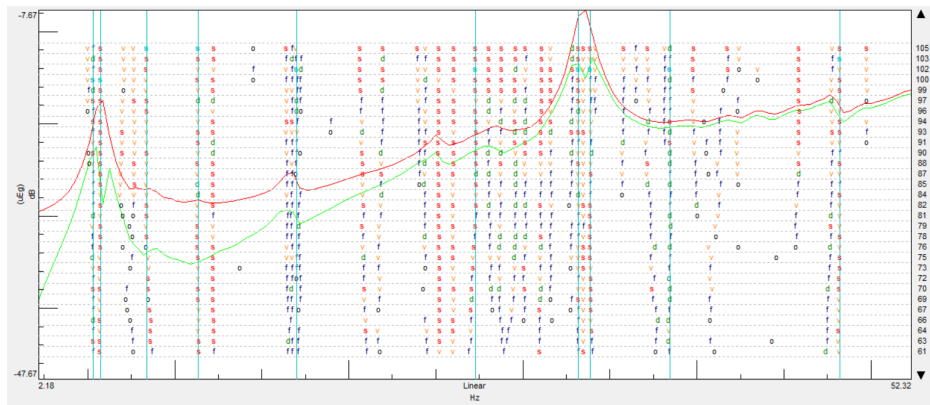


Figure 7.6: Stabilization diagram (20 rpm)

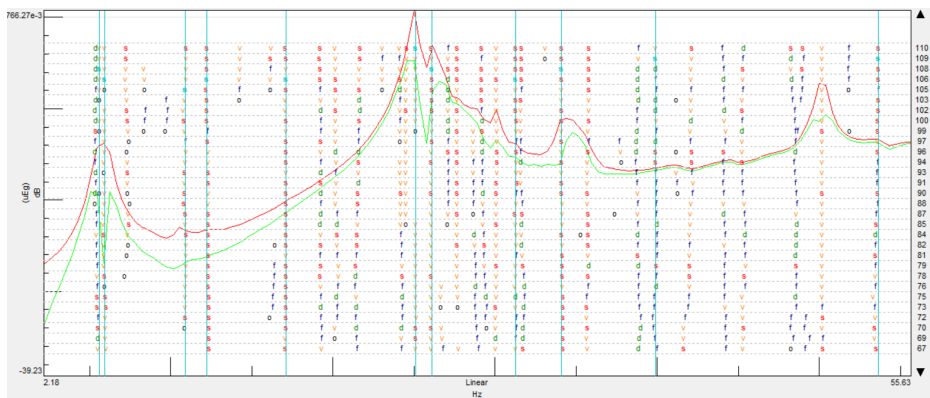


Figure 7.7: Stabilization diagram (30 rpm)

Fig. 7.8 shows a comparison between the Autopower spectra for the accelerometer 8 in X-direction between 10, 20 and 30 rpm. The spectrum at 10 rpm presents a sharp peak at 100 Hz, with a much higher amplitude than the other two spectra. Looking at the spectra at 20 and 30 rpm alone (Fig. 7.9), it is possible to highlight the presence of a peak at 200 Hz for the results related to the 20 rpm test and at 100 and 300 Hz for the 30 rpm test. These findings are consistent with the run-up test results. Moreover, the speed test at 30 rpm shows a spectrum with lower amplitude than the other two.

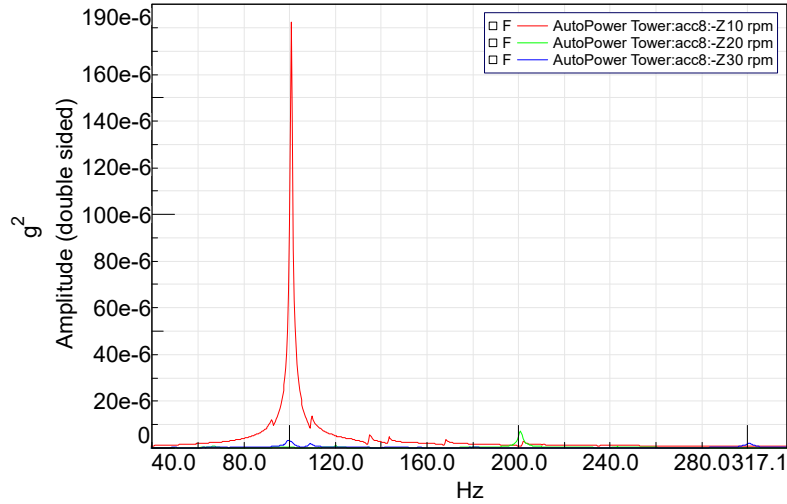


Figure 7.8: Autopower comparison 10, 20, 30 rpm

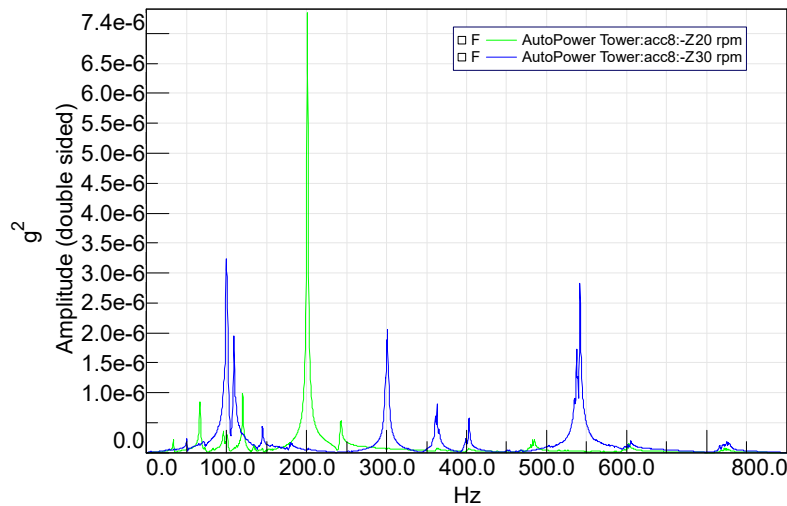


Figure 7.9: Autopower comparison 20, 30 rpm

The results, in the form of frequencies and damping ratios, for the test at 20 rpm, are shown in Table 7.2 for the first ten modes. The natural frequencies are the same obtained from the EMA, so the results are consistent. Some modes show very low damping ratios, therefore they may not be physical modes, but numerical ones, corresponding to the wind turbine harmonics due to blade rotation. This issue is typical in wind turbine studies and was also investigated by Manzato et al. [32], who examined different harmonic removal techniques to study their performance.

Table 7.2: Natural frequencies and damping ratios

Modes	Natural frequency [Hz]	Damping ratio [%]
1	5.36	2.19
2	5.74	1.36
3	8.36	5.30
4	11.39	1.52
5	17.05	0.66
6	28.07	1.41
7	33.13	0.20
8	34.21	0.30
9	40.40	0.92
10	52.24	0.18

In conclusion, the whirling modes phenomena is studied. It regards the edgewise modes of the wind turbine. It was observed that in the EMA these modes appear at two close frequencies, 34.85 Hz and 38.11 Hz. In rotating conditions, the two edgewise modes split into two modes at different frequencies, named whirling modes. These modes tend to move away from each other and the distance between them increases as the rotational speed increases. The graph in Fig. 7.10 represents the two whirling modes' frequencies as the speed increases: on the x-axis there is the frequency while on the y-axis the speed.

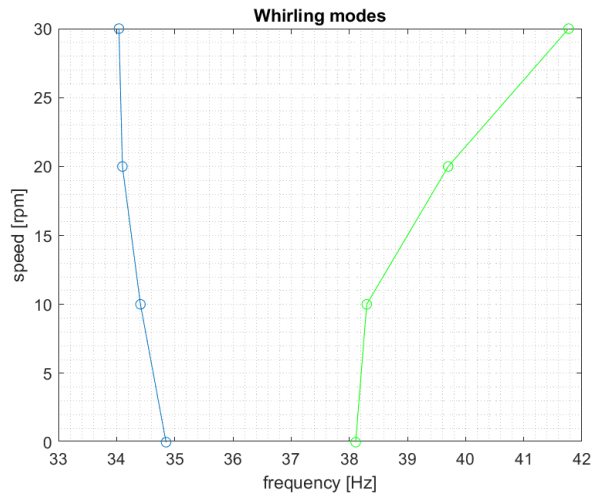


Figure 7.10: Whirling modes' frequency - test speed

Chapter 8

Model Update

In this chapter, the wind turbine model will be updated to improve its consistency with the experimental results. The first step towards achieving this goal will involve an update of the tower model, which will be performed through the use of a Simcenter 3D tool. Subsequently, the process of correlating and validating the entire wind turbine model will be discussed in detail.

8.1 Wind turbine tower model update

After the correlation with the test results and prior to the model update, the tower model is modified to better replicate the structure's behavior. The design focuses on the upper part of the structure, specifically the connection between the rotor of the blades, the motor, and the nacelle. Initially, the rotor was connected to the nacelle via rigid elements, but it was discovered that the model worked better if the connection was made with the motor inside the nacelle. Furthermore, the tests revealed that the rotor and motor are not completely stationary, but can rotate at a small angle together. To replicate this behavior, the motor CAD model was divided into two pieces as described in chapter 5, with an external part that serves as stator and is fixed to the nacelle through its external walls, and an internal part that operates as rotor, that is, the motor part that rotates and transmits the rotation to the blades through the blades' rotor. The three components, the blades' rotor, the motor stator, and the rotor, are linked together by spider connections made of rigid elements (RBE2). The spider connections between the two motor parts are connected by an RBE2, with the rotational degree of freedom along the motor axis remaining free. This allows the motor rotor to rotate with respect to the stator, and the rotor of the blades to rotate with it. The modified motor and the connection with the rotor of the blades are shown in chapter 5, in Fig. 5.17 and 5.18. This final model better replicates the system behavior revealed by the test results, improving the correlation between the numerical and experimental models. Fig. 8.1a and Fig. 8.1b illustrate the MAC matrix comparison for the correlation with the original motor and after the motor was split.

8.1.1 Model update process

The final model configuration chosen is the design with the modified motor, that corresponds to the starting point for the model update. First, a SOL 200 Model Update solution was developed, in which a modal reduction is carried out and the design variables for the model update process are specified.

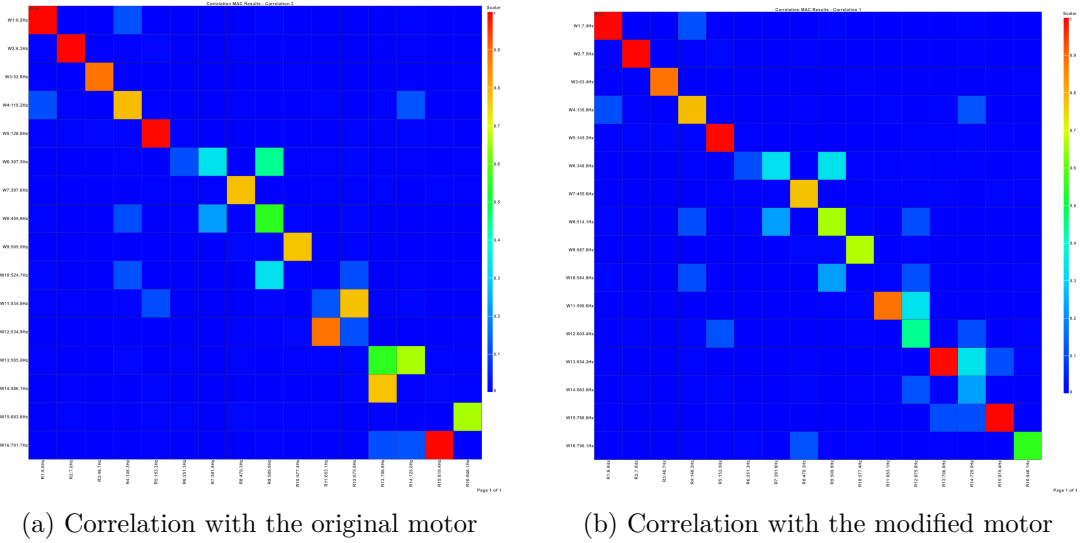


Figure 8.1: MAC matrices before and after the motor change

The test results are evaluated on a discrete number of points, which corresponds to a limited number of DOFs. The numerical model is made up of a large number of nodes and related DOFs, so it must be reduced to match the test DOFs number. Modal reduction involves decreasing the rank of the stiffness, damping, and mass matrices, which must match the number of modes n taken into account in the SOL 200 Model update solution. The reduced modal mass matrix is defined as follow:

$$[M_R] = [\Phi^T][M][\Phi]$$

where the eigenvectors $[\Phi^T]$ are the mass normalized initial work mode shapes in physical coordinates. The reduced modal stiffness matrix is expressed as follows:

$$[K_R] = [\Phi^T][K][\Phi]$$

$[K_R]$ contains the initial eigenvalue, because the eigenvectors are mass normalized.

In the model update, the design variables are defined in the SOL 200 solution. These variables are the material characteristics of the different components, which are listed in Tables 8.1-8.3 with the lower and upper bounds.

Table 8.1: Aluminum design variables

Aluminum		
Property	Lower bound	Upper bound
E	0.9	1.1
ν	0.9	1.1
ρ	0.9	1.1

Table 8.2: Motor design variables

Motor material		
Property	Lower bound	Upper bound
E	0.5	1.5
ν	0.5	1.5
ρ	0.5	1.5

The MAC matrix obtained from the correlation is illustrated in Fig. 8.1b. There are 16 test modes and simulation modes. The correlation between the test and the simulation modes is shown by the diagonal terms, but there are some exception, where the correlation is with the elements near the diagonal terms. The modes do not follow the same sequence, but there are some mode swap, thus the off-diagonal terms close to the diagonal are close to 1, instead of the diagonal ones. The first five mode shapes are well correlated with values close to 1

Table 8.3: Composite material design variables

Carbon fiber/Epoxy laminate		
Property	Lower bound	Upper bound
t_{layer1}	0.9	1.1
t_{layer2}	0.9	1.1
t_{layer3}	0.9	1.1
t_{layer4}	0.9	1.1
t_{layer5}	0.9	1.1
E_{1comp}	0.8	1.2
E_{2comp}	0.8	1.2
ν_{12comp}	0.8	1.2
G_{12comp}	0.8	1.2
G_{1Zcomp}	0.8	1.2
G_{2Zcomp}	0.8	1.2
ρ_{comp}	0.8	1.2

on the diagonal and low values on the off-diagonal elements. Numerical modes 7, 8 and 9 are correlated with test modes 8, 9 and 10 respectively. In Table 8.4 the mode shapes are sequentially paired, thus the MAC value are very low for modes 7, 8 and 9. In the update process these numerical mode shapes are manually paired with the corresponding test mode shapes. By manually pairing the mode shapes the MAC value are 0.742 between test mode 8 and simulation mode 7, 0.615 between test mode 9 and simulation mode 8 and 0.694 between test mode 10 and simulation mode 9. In the update process, the frequency error between these mode pairs is given as objective and the mode swap can be removed by decreasing the frequency difference.

Table 8.4: Modal parameters before update

Mode Number	Model Frequency [Hz]	Test Frequency [Hz]	Frequency Error [%]	MAC
1	7.4	6.6	12.35	0.954
2	7.5	7.0	7.09	0.961
3	63.4	48.7	30.12	0.853
4	135.8	148.3	-8.36	0.784
5	145.3	153.3	-5.20	0.918
6	348.8	251.3	39.05	0.129
7	455.6	391.9	16.32	0.024
8	514.1	479.3	7.27	0.011
9	567.0	509.9	11.22	0.086
10	584.9	577.4	1.35	0.001
11	596.6	653.1	-8.64	0.897
12	603.4	675.8	-10.70	0.421
13	654.3	706.8	-7.42	0.910
14	663.8	725.0	-8.43	0.297
15	785.9	819.4	-4.05	0.947
16	796.1	946.1	-15.84	0.556

Except for the modes 11th, 13th and 15th, which are the torsional modes, the modes after the 5th mode shape have the worst results in terms of MAC value and frequency error. The update strategy will prioritize these modes' optimization while avoiding changing the ones that are already optimally correlated.

Since the initial solution is unmodified during the optimization, it is always possible to restore the starting values during the update. The original FE model should only be updated once

a satisfactory solution has been found. The process is fully reversible as long as the original solution is not changed.

There isn't a single, universal strategy for the model update; rather, it is necessary to select a method that is unique to the given situation.

Tables 8.1-8.3 show the various ranges of variation that were set for the design variables. Given that the motor material is unknown, a wider range of variation is taken into account. Contrarily, the remaining properties of the structure for aluminum are well known, so the range of variation is limited. The margin of variation for the composite material is lower than that used for the motor material, because the manufacturer partially provided the material specifications. Although it is still higher than for aluminum because of the uncertainties on composite's properties.

The Least Square algorithm is the first algorithm used in the model update. With no restrictions on the design variables, this algorithm minimizes the objective function at each iteration. Then, it fixes the design variables that went over the upper or lower bound by setting them to those values. The objective function is then minimized once more without restrictions on the design variables, this time while taking into account a smaller set of variables. These two steps are repeated until no variable exceeds the limits. The optimization ends when the total error does not improve for five iterations in a row, all design variables have reached their bounds, or the maximum number of iterations or the minimum improvement have been reached. This algorithm's primary drawback is the possibility of discovering an objective function minimum that is not a global minimum. It is especially possible when there are many targets involved. However, compared to other algorithms used in this optimization process, such as the genetic algorithm, it converges extremely rapidly.

An initial update attempt was made by turning off the mode shapes and setting the frequencies as optimization targets with the same weight. After the first optimization with only the frequencies as target, a second optimization is carried out including also the mode shapes. It was observed that using the default weight $W = 1$ for all mode shapes and frequencies did not lead to improvements in the overall error, therefore different weight were set for the frequencies and mode shapes. In particular, it was observed that a greater weight equal to 1.5 on the first five frequencies and on f_7 , f_8 and f_9 led to good improvements in the results.

The least square algorithm was able to decrease the overall error for some optimization steps, but it reached a local minimum in the objective function and it was unable to improve the results even if the target weights were changed.

For this reason, the genetic algorithm was implemented. The fundamental tenet of the Genetic Algorithm is based on Charles Darwin's theory that the best genetic material is produced by individuals who are best at adapting to their environment. From a given initial set of suggested solutions, the most effective ones are chosen and used to develop new solutions. Then, over succeeding generations, better solutions are created. The algorithm creates the initial population at each iteration, which consists of random design points constrained by the linear range of the design variable and its lower and upper bounds. The objective function is used to determine each population member's fitness, and the fittest members of the population will participate in the process of creating new populations more frequently. Through mutation and cross-over, it virtually mates the numerical digits of two individuals to produce a new population for the following generation. These steps are repeated for the total number of generation. It always cycles over all iterations. Because of the quasi-randomness of this algorithm, there is no guarantee that the total error will go down between two iterations. When the maximum number of iterations is reached or there has been no improvement for five iterations in a row, the optimization stops.

The optimization steps with the genetic algorithm are the following ones:

1. all the frequencies are optimized with unit weight;
2. all the frequencies have unit weight except for the first five frequencies and f_7 , f_8 and f_9 , which feature a weight equal to 1.5;
3. all the frequencies have unit weight except for the first five frequencies and f_6 and f_7 , which feature a weight equal to 1.5;
4. all the frequencies and mode shapes have unit weight except for the first five frequencies and f_7 , f_8 and f_9 and the related mode shapes, which feature a weight equal to 1.5;
5. all the frequencies and mode shapes have unit weight except for the first five frequencies and f_6 , f_7 and the related mode shapes, which feature a weight equal to 1.5;
6. all the frequencies and mode shapes have unit weight except for the first five frequencies and on f_{15} , f_{16} and the related mode shapes, which feature a weight equal to 1.5;
7. all the frequencies and mode shapes have unit weight.

8.1.2 Model update results

The results of the model update are described in this section. The MAC matrix is now diagonal as shown in Fig 8.3b. Although the first five modes have seen a slight improvement, they were already excellent prior to the update. Three of them (modes 1, 2, and 5) have MAC values above 0.9, while mode 4 MAC value is the lowest at 0.791, which can be still considered as acceptable. Modes 6 and 7 show little correlation, but mode 7 MAC value increased from 0.024 to 0.307. The mode swap between the test modes 8,9, and 10 and the numerical modes 7,8, and 9 is resolved, and the corresponding diagonal values for these modes are 0.773, 0.597, and 0.690, respectively. In Fig. 8.2a, the MAC diagonal values before and after the update are compared. The middle modes show a significant improvement as a result of the mode swap fixing. Modes 11, 12, 13, and 14 have also seen improvements. Mode 15 has a higher MAC value, but the frequency error increased, leading to a mode swap between modes 15 and 16, which are now correlated with test modes 16 and 15, respectively. Despite being lower after the update, the MAC value for test mode 15 and numerical mode 16 is still equal to 0.928, indicating that there is a strong correlation between the two mode shapes. There has been a general improvement in frequency errors, with the exception of modes 4, 5, 8, and 9, for which the error is still kept below 10% or close to this value (as for mode 4, where $f_{err} = -11.938\%$). Although the frequency error for modes 6 and 7 is high (25.136% and 10.517%), it is significantly lower than the initial value, with mode 7 error falling from 50.653% to 10.517%. The modes between 10 and 14 have a frequency error that has decreased to an extremely low value—under 5%. Tables 8.5 and 8.6 report on the design variables and their updated values. In Table 8.7, the final MAC values and frequency errors are listed.

Table 8.5: Model Update Design Variables

Variable name	Initial value	Lower bound	Upper bound	Final value (fractional)	Final value
$E_{al,modified}$	68980 MPa	0.9	1.1	0.9	62082 MPa
$\nu_{al,modified}$	0.33	0.9	1.1	0.9	0.297
$\rho_{al,modified}$	2.711 g/cm^3	0.9	1.1	1.1	2.982 g/cm^3
$E_{al,motor}$	68980 MPa	0.5	1.5	0.5	34490 MPa
$\nu_{al,motor}$	0.33	0.5	1.5	0.752	0.248
$\rho_{al,motor}$	2.711 g/cm^3	0.5	1.5	1.5	4.067 g/cm^3

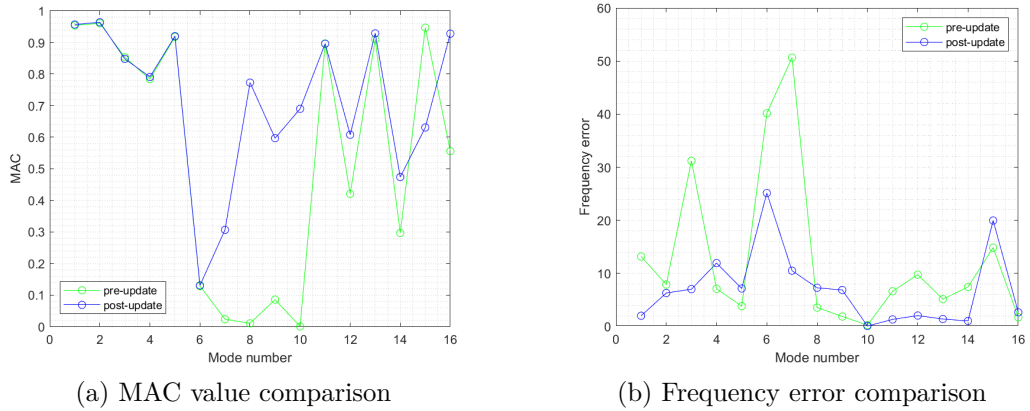


Figure 8.2: MAC and frequency error comparison for the diagonal values before and after the update

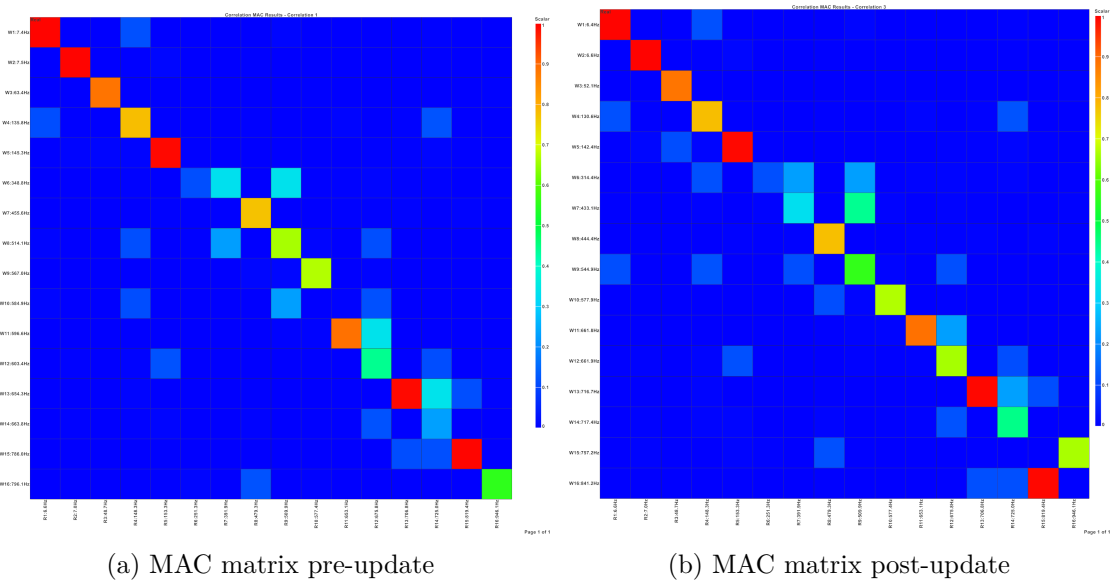


Figure 8.3: MAC matrix comparison before and after the update

Overall, the majority of modes experience enhancements in frequency errors and MAC values. Significantly, modes 6 and 7 exhibit substantial enhancements, given their high frequency errors. It is worth noting that establishing correlations for high modes such as torsional modes is challenging due to their atypical mode shape. Thus, the presence of high MAC values for some torsional modes may be considered a favorable outcome. Lastly, the findings show optimal correlation for the first 5 modes, including the first two tower bending, that are the modes of interest of the structure. Therefore, the update has been successfully completed with acceptable results. Fig. 8.4a to Fig. 8.7d illustrate the sixteen mode shapes after the model update.

Table 8.6: Model Update Design Variables

Variable name	Initial value	Lower bound	Upper bound	Final value (fractional)	Final value
t_{layer1}	1.2 mm	0.9	1.1	0.9	1.080 mm
t_{layer2}	0.495 mm	0.9	1.1	1.015	0.502 mm
t_{layer3}	1.28 mm	0.9	1.1	0.9	1.152 mm
t_{layer4}	0.0125 mm	0.9	1.1	0.943	0.012 mm
t_{layer5}	0.0125 mm	0.9	1.1	0.9	0.011 mm
t_{total}	3 mm	/	/	/	2.757 mm
$E_{1_{comp}}$	130000 MPa	0.8	1.2	0.8	104000 MPa
$E_{2_{comp}}$	7900 MPa	0.8	1.2	1.2	9480 MPa
$\nu_{12_{comp}}$	0.3	0.8	1.2	1.199	0.36
$G_{12_{comp}}$	5000 MPa	0.8	1.2	0.8	4000 MPa
$G_{1Z_{comp}}$	5000 MPa	0.8	1.2	0.804	4020 MPa
$G_{2Z_{comp}}$	5000 MPa	0.8	1.2	0.84	4200 MPa
ρ_{comp}	1.55 g/cm ³	0.8	1.2	0.823	1.276 g/cm ³

Table 8.7: Model Update Results

Mode Number	Model Frequency [Hz]	Test Frequency [Hz]	Pre-Update Frequency Error [%]	Post-Update Frequency Error [%]		MAC	
1	6.4	6.6	13.179	-2.015	↑	0.957	↑
2	6.6	7.0	7.902	-6.307	↑	0.964	↑
3	52.1	48.7	31.200	7.028	↑	0.848	↓
4	130.6	148.3	-7.096	-11.938	↓	0.791	↑
5	142.4	153.3	-3.842	-7.162	↓	0.920	↑
6	314.4	251.3	40.150	25.136	↑	0.131	↑
7	433.3	391.9	50.653	10.517	↑	0.307	↑
8	444.4	479.3	-3.566	-7.287	↓	0.773	↑
9	545.0	509.9	1.884	6.874	↓	0.597	↑
10	577.9	577.4	-0.255	0.089	↑	0.690	↑
11	661.8	653.1	-6.636	1.334	↑	0.896	=
12	661.9	675.8	-9.757	-2.054	↑	0.608	↑
13	716.7	706.8	-5.157	1.405	↑	0.929	↑
14	717.4	725.0	-7.444	-1.043	↑	0.474	↑
15	757.2	946.1	-14.852	-19.963	↓	0.631	↑
16	841.2	819.4	-1.725	2.669	↓	0.928	↓

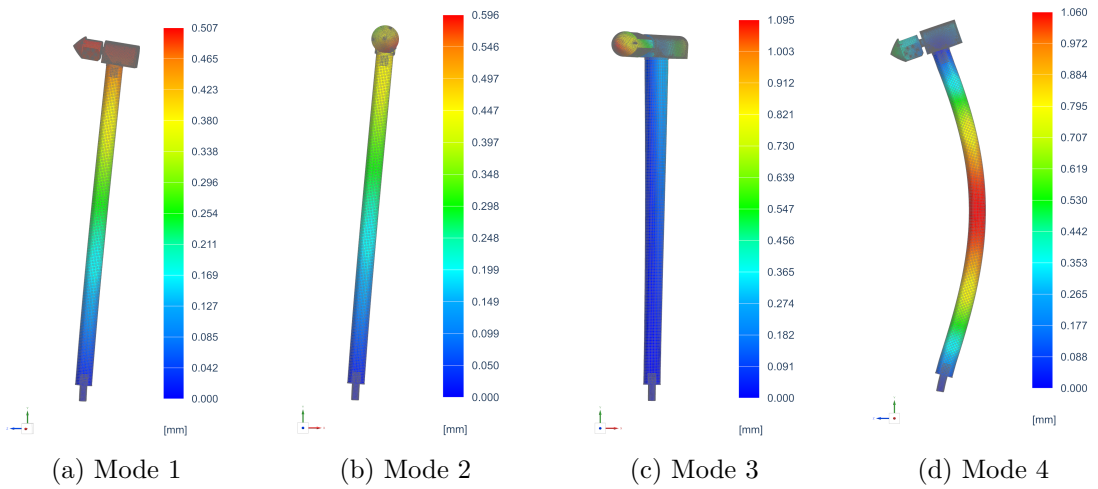


Figure 8.4: Modal shapes of the wind turbine tower structure (1,2,3,4)

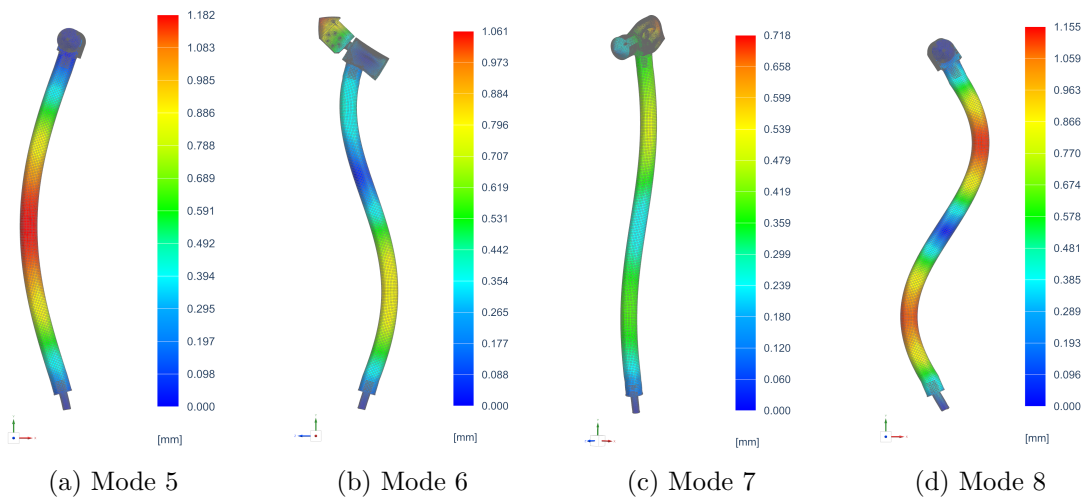


Figure 8.5: Modal shapes of the wind turbine tower structure (5,6,7,8)

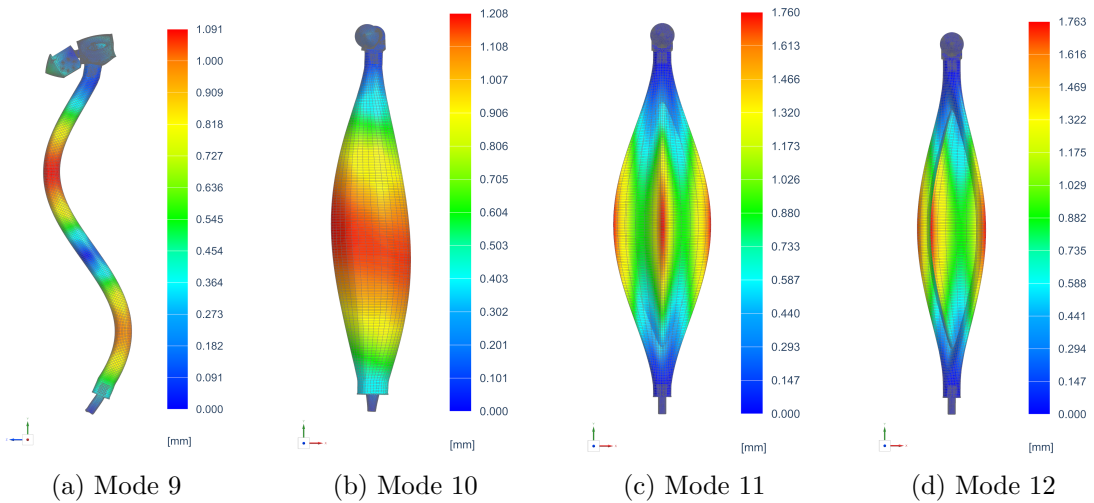


Figure 8.6: Modal shapes of the wind turbine tower structure (9,10,11,12)

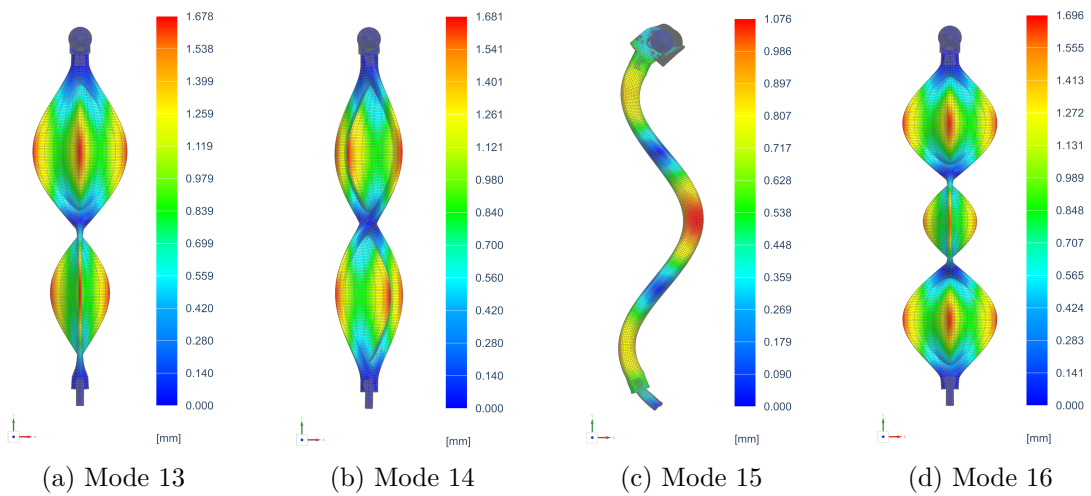


Figure 8.7: Modal shapes of the wind turbine tower structure (13,14,15,16)

8.2 Wind turbine model update

In this final paragraph, the wind turbine entire model composed by the three blades and the tower is correlated with the modal results obtained from the EMA described in chapter 6. The results in terms of frequency errors and MAC values are listed in Table 8.8. The MAC matrix is illustrated in Fig 8.8.

Table 8.8: Wind turbine correlation parameters

Mode Number	Model Frequency [Hz]	Mode Number	Test Frequency [Hz]	Frequency Error [%]	Mode Shape	MAC
1	5.01	1	5.13	-2.33	1 st Tower FA	0.967
2	5.54	2	5.54	-6.52	1 st Tower SS	0.719
3	9.91	3	8.70	13.90	1 st Flap yaw	0.869
4	11.51	4	11.62	-0.99	1 st Flap pitch	0.692
5	13.37	5	17.03	-21.49	1 st Flap Sym	0.337
6	26.18	6	28.19	-7.12	2 nd Flap yaw	0.790
7	32.79	8	34.91	-6.07	1 st Edge pitch	0.264
8	33.49	9	38.11	-12.13	1 st Edge yaw	0.717
9	39.15	7	32.39	21.25	2 nd Flap pitch	0.530
10	42.5	10	52.08	-18.41	2 nd Flap sym	0.810

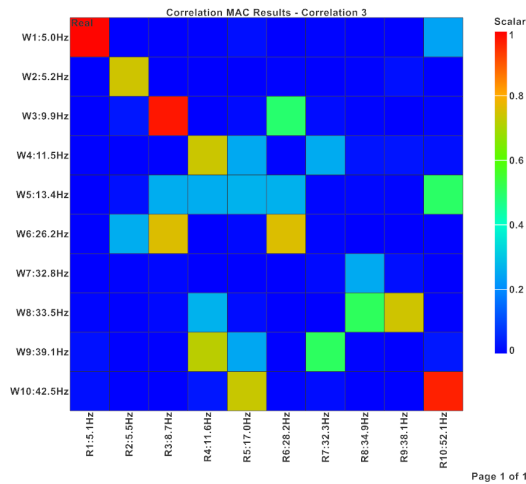


Figure 8.8: Wind turbine correlation

The final step involves updating the model for the complete wind turbine system. Due to the blades mesh being modeled via the PCOMPS property, which is not compatible with model updates in Simcenter 3D, Simcenter HEEDS will be employed for updating the wind turbine model.

The parameters chosen to update the model are provided as input from Simcenter 3D and comprise the material properties of the tower and motor, as well as the stiffness of the celas elements serving as model constraint. To examine the system's behavior in the vertical direction and the potential presence of an up/down tower mode, the stiffness in this direction is initially set to a lower value. Table 8.9 presents an overview of the variables, including their initial values, as well as the upper and lower bounds and the final value after the update.

The objectives of the analysis are: maximize the MAC values and minimize the frequency errors. The final results for the ten mode pairs are presented in Table 8.10.

Table 8.9: Model update design variables

Property	Initial value	Lower bound	Upper bound	Final Value
Base_spring_K1 [N/mm]	1e+17	1e+16	5e+18	1e+16
Base_spring_K2 [N/mm]	1e+12	1e+10	5e+17	4.75e+17
Base_spring_K3 [N/mm]	1e+17	1e+16	5e+18	1e+16
Base_spring_K4 [N/mm]	1e+17	1e+16	5e+18	5e+18
Base_spring_K5 [N/mm]	1e+17	1e+16	5e+18	1e+16
Base_spring_K6 [N/mm]	1e+17	1e+16	5e+18	5e+18
CF_EPOXY_E1 [MPa]	104000	93600	114401	93600.9
CF_EPOXY_E2 [MPa]	9480	8532	10428	8645.7
CF_EPOXY_G12 [MPa]	4000	3600	4400	3600
CF_EPOXY_G13 [MPa]	4020	3619	4423	3618.7
CF_EPOXY_G23 [MPa]	4200	3782	4622	3832.1
CF_EPOXY_NU12	0.36	0.324	0.396	0.324
CF_EPOXY_RHO [g/cm^3]	1.276	1.148	1.403	1.160
Motor_E [MPa]	34490	27598	41397	28288.2
Motor_RHO [g/cm^3]	4.067	3.253	4.879	3.253
Motor_NU	0.248	0.198	0.298	0.198

Table 8.10: Wind turbine correlation parameters

Mode Number	Model Frequency [Hz]	Mode Number	Test Frequency [Hz]	Frequency Error [%]		MAC	
1	5.08	1	5.13	-1.06	↑	0.967	=
2	5.25	2	5.54	-5.20	↑	0.729	↑
3	9.77	3	8.70	12.32	↑	0.887	↑
4	11.52	4	11.62	-0.89	↑	0.704	↑
5	13.32	5	17.03	-21.79	↓	0.354	↑
6	25.82	6	28.19	-8.40	↓	0.795	=
7	32.78	8	34.91	-6.09	=	0.262	=
8	33.50	9	38.11	-12.11	=	0.715	=
9	39.12	7	32.39	21.15	=	0.539	↑
10	42.49	10	52.08	-18.41	=	0.820	↑

The model update resulted in slight enhancements in the overall outcomes. The majority of the frequency errors and MAC values remained unchanged, with the improvements limited to the first four modes, specifically the first two modes. This observation aligns with the update configuration since the considered variables, apart from the constraint stiffnesses, pertain to the tower structure material, resulting in the improvement of the first two bending modes of the tower.

Moreover, replicating the boundary conditions of the tower on the model is challenging due to the wind turbine tower’s high instability, which affects the blade modes. Creating a clamped condition for the tower that does not excessively limit its behavior is a difficult task. For instance, the first flapwise symmetric mode, mode 5, displays poor correlation with the experimental outcome due to the limited tower model deformation. Indeed, the model includes a constraint on the tower base that fixes the rotation around the vertical axis; when this constraint is removed, mode 5 correlation improves. However, this results in excessively high tower deformation, which reduces the correlation for the other modes. As a result, the rotational constraint is required.

Furthermore, since the number of accelerometers on the blade is limited, the test results are discretized compared to the numerical ones, which may contribute to the low correlation.

Chapter 9

Conclusions and Future Work

9.1 Conclusions

This thesis has successfully conducted both numerical and experimental modal analyses to dynamically characterize a scaled wind turbine. Prior to the entire wind turbine dynamic characterization, the wind turbine tower's dynamic behavior was investigated.

The tower numerical simulation and EMA results confirmed the presence of fundamental bendings in the FA and SS direction, as well as high-order modes, including the tower torsional modes. Despite the complex shape of these modes, the results showed a good correlation between the numerical and the experimental modal parameters.

The model update led to improvements in frequency errors and MAC values. The first 5 modes, including the first two tower bendings, showed optimal correlation. Modes 6 and 7 exhibited substantial enhancements. Additionally, the mode switching for numerical modes 7,8, and 9 was fixed, and the correlation was on the diagonal of the MAC matrix. Therefore, the update has been successfully completed with acceptable results.

The validated tower FE model was used for the entire wind turbine dynamic characterization. Based on the results of both numerical and experimental analyses, it could be concluded that the dominant modes of the wind turbine blades mainly affect the dynamic behavior of the entire structure. The results indicated that the identified mode shapes entail the bending of the tower in both the FA and SS directions, the first three flapwise modes, comprising two asymmetric modes and one symmetric mode, as well as the two edgewise modes and the second group of flapwise modes, as expected.

The experimental and modal analysis efficiently captured the modal behavior of the structure and estimated the modal parameters with great accuracy. It is particularly interesting to be able to confirm the presence of the flap-wise and edgewise modes of the wind turbine not only through simulation results but also by experimental results. The sensor configuration used in the study was found to be sufficient for the frequency range of interest, with good accuracy in capturing all the mode shapes. However, some mode shapes were found to be similar to each other due to spatial aliasing resulting from the limited number of accelerometers on the blades.

The feasibility of applying OMA to an operating small-scale wind turbine has been established. The natural frequencies obtained through OMA were consistent with the EMA results. However, the sensor configuration used was insufficient to visualize all the mode shapes, and some modes with low damping ratios might correspond to numerical rather than physical modes related to wind turbine harmonics. The study also investigated whirling modes, which appear at close frequencies in parked conditions and split into two modes at different frequencies under rotating conditions.

Overall, the study provided valuable insights into the dynamic behavior of wind turbines and has enabled the estimation of modal parameters in both parked and operating conditions through physical sensors, which is a significant improvement over the limited use of simulated data in previous studies. Furthermore, this research work provided a foundation for implementing SHM strategies using OMA in wind turbines. While previous studies have focused on damage detection on blades, this study demonstrated the potential for OMA to be used for monitoring the overall health of wind turbines.

9.2 Future Work

The following are potential future steps that can be taken to improve the wind turbine dynamic characterization:

- the wind turbine FE model can be enhanced by including the material properties of the blade in the update process. A sensitivity analysis can also be conducted to increase the efficiency of the process.
- A multibody flexible model can be developed from the validated wind turbine FE model to simulate the actual behavior of the wind turbine.
- EMA with a larger set of sensors on the blades might result in better identification of the wind turbine mode shapes.
- Since the wind turbine fundamental modes are limited to a frequency range below 100 Hz, the test can be replicated with a lower bandwidth and a longer acquisition time for the OMA to improve the outcomes.
- OMA with instrumented blades can be investigated as the results shown in this work are encouraging. Therefore, data from a fully instrumented wind turbine are desirable to fully comprehend the modes.
- Finally, additional studies can be conducted to evaluate potential methods for canceling the harmonics from the results to obtain more clear and precise stabilization diagram, and as a result, a more accurate modal parameter estimation.

Bibliography

- [1] S. M. Avila, M. A. Shzu, M. V. Morais, and Z. J. D. Prado, “Numerical modeling of the dynamic behavior of a wind turbine tower”, *Journal of Vibration Engineering and Technologies*, vol. 4, 3 2016, ISSN: 25233939.
- [2] L. Zhou, Y. Li, F. Liu, Z. Jiang, Q. Yu, and L. Liu, “Investigation of dynamic characteristics of a monopile wind turbine based on sea test”, *Ocean Engineering*, vol. 189, 2019, ISSN: 00298018. DOI: 10.1016/j.oceaneng.2019.106308.
- [3] F. Z. Joyce Lee, “Global wind report - annual market update 2022”, Global Wind Energy Council (GWEC), Brussels, Belgian, 2022.
- [4] Y. Chen, A. S. Escalera Mendoza, and D. T. Griffith, “Experimental and numerical study of high-order complex curvature mode shape and mode coupling on a three-bladed wind turbine assembly”, *Mechanical Systems and Signal Processing*, vol. 160, p. 107873, 2021, ISSN: 0888-3270. DOI: <https://doi.org/10.1016/j.ymsp.2021.107873>. [Online]. Available: <https://www.sciencedirect.com/science/article/pii/S0888327021002685>.
- [5] K. Jahani, R. G. Langlois, and F. F. Afagh, *Structural dynamics of offshore wind turbines: A review*, 2022. DOI: 10.1016/j.oceaneng.2022.111136.
- [6] O. Ramírez, D. Tcherniak, and G. C. Larsen, “Comparative study of oma applied to experimental and simulated data from an operating vestas v27 wind turbine”, 2015.
- [7] Y. Zheng, “Flutter stability analysis of stochastic aeroelastic systems via the generalized eigenvalue-based probability density evolution method”, *Mechanical Systems and Signal Processing*, vol. 156, p. 107666, 2021, ISSN: 0888-3270. DOI: <https://doi.org/10.1016/j.ymsp.2021.107666>. [Online]. Available: <https://www.sciencedirect.com/science/article/pii/S0888327021000613>.
- [8] M. Chetan, D. T. Griffith, and S. Yao, “Flutter predictions in the design of extreme-scale segmented ultralight morphing rotor blades”, 2019. DOI: 10.2514/6.2019-1298.
- [9] X. Dong, J. Lian, H. Wang, T. Yu, and Y. Zhao, “Structural vibration monitoring and operational modal analysis of offshore wind turbine structure”, *Ocean Engineering*, vol. 150, pp. 280–297, 2018, ISSN: 0029-8018. DOI: <https://doi.org/10.1016/j.oceaneng.2017.12.052>. [Online]. Available: <https://www.sciencedirect.com/science/article/pii/S0029801817307904>.
- [10] F. Ferroudji, “Numerical modal analysis of a 850 kw wind turbine steel tower”, *International Review of Applied Sciences and Engineering*, vol. 12, 1 2021, ISSN: 20634269. DOI: 10.1556/1848.2020.00091.
- [11] C. Rebelo, A. Moura, H. Gervásio, M. Veljkovic, and L. S. da Silva, “Comparative life cycle assessment of tubular wind towers and foundations - part 1: Structural design”, *Engineering Structures*, vol. 74, 2014, ISSN: 01410296. DOI: 10.1016/j.engstruct.2014.02.040.

- [12] Y. Hu, C. Baniotopoulos, and J. Yang, "Effect of internal stiffening rings and wall thickness on the structural response of steel wind turbine towers", *Engineering Structures*, vol. 81, 2014, ISSN: 01410296. DOI: 10.1016/j.engstruct.2014.09.015.
- [13] J. Peeters, "Simulation of dynamic drive train loads in a wind turbine", 2006.
- [14] S. Adhikari and S. Bhattacharya, "Dynamic analysis of wind turbine towers on flexible foundations", *Shock and Vibration*, vol. 19, 1 2012, ISSN: 10709622. DOI: 10.3233/SAV-2012-0615.
- [15] L. Arany, S. Bhattacharya, J. H. Macdonald, and S. J. Hogan, "Closed form solution of eigen frequency of monopile supported offshore wind turbines in deeper waters incorporating stiffness of substructure and ssi", *Soil Dynamics and Earthquake Engineering*, vol. 83, 2016, ISSN: 02677261. DOI: 10.1016/j.soildyn.2015.12.011.
- [16] T. G. Carne and G. H. James, "The inception of oma in the development of modal testing technology for wind turbines", *Mechanical Systems and Signal Processing*, vol. 24, 5 2010, ISSN: 08883270. DOI: 10.1016/j.ymsp.2010.03.006.
- [17] P. Avitabile, *Modal testing: a practitioner's guide*. John Wiley & Sons, 2017.
- [18] H. Vold, J. Kundrat, G. T. Rocklin, and R. Russell, "A multi-input modal estimation algorithm for mini-computers", *SAE Transactions*, vol. 91, pp. 815–821, 1982, ISSN: 0096736X, 25771531. [Online]. Available: <http://www.jstor.org/stable/44631984> (visited on 03/10/2023).
- [19] D. J. Ewins, *Modal testing: theory, practice and application*. John Wiley & Sons, 2009.
- [20] D. L. Brown, R. J. Allemang, R. Zimmerman, and M. Mergeay, "Parameter estimation techniques for modal analysis", *SAE Transactions*, vol. 88, pp. 828–846, 1979, ISSN: 0096736X, 25771531. [Online]. Available: <http://www.jstor.org/stable/44633920> (visited on 03/10/2023).
- [21] N. M. M. Maia and J. M. M. Silva, "Modal analysis identification techniques", *Philosophical Transactions: Mathematical, Physical and Engineering Sciences*, vol. 359, no. 1778, pp. 29–40, 2001, ISSN: 1364503X. [Online]. Available: <http://www.jstor.org/stable/3066392> (visited on 03/10/2023).
- [22] B. Peeters, H. Van der Auweraer, P. Guillaume, and J. Leuridan, "The polymax frequency-domain method: A new standard for modal parameter estimation? shock and vibration", *Special Issue Dedicated to Professor Bruno Piombo*, vol. 395, Jan. 2004.
- [23] B. Peeters, H. Van der Auweraer, J. Leuridan, and T. Vassel, "Polymax modal parameter estimation: Challenging automotive and aerospace applications", pp. 1–13+572, Jan. 2004.
- [24] S. L. Ward Heylen and P. Sas, "Modal analysis theory and testing", 2012.
- [25] E. D. Lorenzo, S. Manzato, B. Peeters, and H. V. D. Auweraer, "Virtual structural monitoring of wind turbines using operational modal analysis techniques", vol. 569-570, 2013. DOI: 10.4028/www.scientific.net/KEM.569-570.523.
- [26] B. Peeters and H. Van der Auweraer, "Polymax: A revolution in operational modal analysis", *1st International Operational Modal Analysis Conference*, Jan. 2005.
- [27] P. Guillaume, P. Verboven, S. Vanlanduit, H. V. D. Auweraer, and B. Peeters, "A poly-reference implementation of the least-squares complex frequency-domain estimator", 2003.
- [28] E. Di Lorenzo, "Operational modal analysis for rotating machines", PhD Thesis, KU Leuven, University of Naples "Federico II", 2017.

-
- [29] E. D. Lorenzo, S. Manzato, B. Peeters, and F. Marulo, “Modal parameter estimation for operational wind turbines”, 2014.
- [30] G. H. James, “Extraction of modal parameters from an operating hawt using the natural excitation technique (next)”, Nov. 1993. [Online]. Available: <https://www.osti.gov/biblio/10191336>.
- [31] J. R. White, “Operational monitoring of horizontal axis wind turbines with inertial measurements”, Ph.D. dissertation, Purdue University, 2010.
- [32] S. Manzato, J. R. White, B. LeBlanc, B. Peeters, and K. Janssens, “Advanced identification techniques for operational wind turbine data”, in *Topics in Modal Analysis, Volume 7: Proceedings of the 31st IMAC, A Conference on Structural Dynamics, 2013*, Springer, 2014, pp. 195–209.
- [33] D. Tcherniak and G. C. Larsen, “Application of oma to an operating wind turbine: Now including vibration data from the blades”, in *5th International Operational Modal Analysis Conference*, 2013.
- [34] S. Chauhan, D. Tcherniak, J. Basurko, *et al.*, “Operational modal analysis of operating wind turbines: Application to measured data”, in *Rotating Machinery, Structural Health Monitoring, Shock and Vibration, Volume 5: Proceedings of the 29th IMAC, A Conference on Structural Dynamics, 2011*, Springer, 2011, pp. 65–81.
- [35] C. Devriendt, M. Elkafafy, G. De Sitter, P. J. Jordaens, and P. Guillaume, “Continuous dynamic monitoring of an offshore wind turbine on a monopile foundation”, *ISMA2012*, 2012.
- [36] G. De Sitter, W. Weijtjens, M. El-Kafafy, and C. Devriendt, “Monitoring changes in the soil and foundation characteristics of an offshore wind turbine using automated operational modal analysis”, in *Key Engineering Materials*, Trans Tech Publ, vol. 569, 2013, pp. 652–659.
- [37] A. Iliopoulos, R. Shirzadeh, W. Weijtjens, P. Guillaume, D. Van Hemelrijck, and C. Devriendt, “A modal decomposition and expansion approach for prediction of dynamic responses on a monopile offshore wind turbine using a limited number of vibration sensors”, *Mechanical Systems and Signal Processing*, vol. 68, pp. 84–104, 2016.
- [38] E. D. Lorenzo, S. Manzato, B. Peeters, F. Marulo, and W. Desmet, “Structural health monitoring strategies based on the estimation of modal parameters”, vol. 199, 2017. DOI: 10.1016/j.proeng.2017.09.521.
- [39] P. Iannelli, F. Angeletti, P. Gasbarri, M. Panella, and A. Rosato, “Deep learning-based structural health monitoring for damage detection on a large space antenna”, *Acta Astronautica*, vol. 193, 2022, ISSN: 00945765. DOI: 10.1016/j.actaastro.2021.08.003.
- [40] A. Mironov and P. Doronkin, “The demonstrator of structural health monitoring system of helicopter composite blades”, vol. 37, 2021. DOI: 10.1016/j.prostr.2022.01.080.
- [41] P. Li, S. Xu, C. Xu, F. Du, and S. Cao, “Development of a miniature dynamic stiffness measurement prototype toward structural health monitoring of space inflatable structures”, *Measurement*, vol. 194, p. 111051, 2022, ISSN: 0263-2241. DOI: <https://doi.org/10.1016/j.measurement.2022.111051>. [Online]. Available: <https://www.sciencedirect.com/science/article/pii/S0263224122003177>.
- [42] T. Siebel, A. Friedmann, M. Koch, and D. Mayer, “Assessment of mode shape-based damage detection methods under real operational conditions”, vol. 1, 2012.

- [43] H. C. Kim, M. H. Kim, and D. E. Choe, “Structural health monitoring of towers and blades for floating offshore wind turbines using operational modal analysis and modal properties with numerical-sensor signals”, *Ocean Engineering*, vol. 188, 2019, ISSN: 00298018. DOI: [10.1016/j.oceaneng.2019.106226](https://doi.org/10.1016/j.oceaneng.2019.106226).
- [44] K. Maes, A. Iliopoulos, W. Weijtjens, C. Devriendt, and G. Lombaert, “Dynamic strain estimation for fatigue assessment of an offshore monopile wind turbine using filtering and modal expansion algorithms”, *Mechanical Systems and Signal Processing*, vol. 76, pp. 592–611, 2016.
- [45] E. Branlard, J. Jonkman, S. Dana, and P. Doubrawa, “A digital twin based on open-fast linearizations for real-time load and fatigue estimation of land-based turbines”, in *Journal of Physics: Conference Series*, IOP Publishing, vol. 1618, 2020, p. 022 030.
- [46] M. Peeters, G. Santo, J. Degroote, and W. Van Paeppegem, “High-fidelity finite element models of composite wind turbine blades with shell and solid elements”, *Composite Structures*, vol. 200, pp. 521–531, 2018.
- [47] A. Iliopoulos, R. Shirzadeh, W. Weijtjens, P. Guillaume, D. V. Hemelrijck, and C. Devriendt, “A modal decomposition and expansion approach for prediction of dynamic responses on a monopile offshore wind turbine using a limited number of vibration sensors”, *Mechanical Systems and Signal Processing*, vol. 68-69, pp. 84–104, 2016, ISSN: 0888-3270. DOI: <https://doi.org/10.1016/j.ymssp.2015.07.016>. [Online]. Available: <https://www.sciencedirect.com/science/article/pii/S0888327015003350>.
- [48] K. Maes, A. Iliopoulos, W. Weijtjens, C. Devriendt, and G. Lombaert, “Dynamic strain estimation for fatigue assessment of an offshore monopile wind turbine using filtering and modal expansion algorithms”, *Mechanical Systems and Signal Processing*, vol. 76-77, pp. 592–611, 2016, ISSN: 0888-3270. DOI: <https://doi.org/10.1016/j.ymssp.2016.01.004>. [Online]. Available: <https://www.sciencedirect.com/science/article/pii/S0888327016000066>.

Acknowledgements

Ringrazio i Professori Alfonso Pagani e Matteo Filippi, relatori di questa tesi, per avermi dato l'opportunità di svolgerla. Grazie per avermi seguita e aiutata durante la stesura del mio lavoro e avermi fornito preziosi consigli.

Ringrazio i Dr. ing. Emilio Di Lorenzo e Alberto Garcia De Miguel, senza i quali la collaborazione con Siemens non sarebbe stata possibile. Grazie perchè la vostra esperienza e i vostri consigli mi hanno arricchita e grazie per quest'opportunità che mi ha regalato 6 mesi bellissimi e intensi al fianco di persone fantastiche.

Un ringraziamento speciale va alla mia supervisor, l'Ing. Silvia Vettori, per essere stata una guida preziosa e aver creduto in me. Le sono grata per la fiducia e il sostegno che mi ha dato. È stata e sarà in futuro un riferimento e un esempio da seguire.

Grazie ai miei genitori, per essere stati i miei primi sostenitori, senza avermi mai fatto sentire il peso delle aspettative, perchè mi avete insegnato prima di tutto che l'importante è essere felice. Mi avete sempre spronato a oltrepassare i miei limiti e a credere in me stessa. Tutte le scelte che ho preso finora sono frutto del vostro incoraggiamento a superare le mie insicurezze, per scoprire che posso arrivare sempre molto più in là di quel che immagino. Quando rifletto su come voglio costruire il mio futuro penso a voi.

Grazie Vale, per aver seguito sempre le mie orme fin dalla scuola elementare da brava sorellina minore e poi aver compreso che non sono un buon esempio. Scherzi a parte, grazie per essermi stata d'ispirazione per diventare una persona migliore, perché quando io ero chiusa e introversa, tu sei stata un esempio di forza, socievolezza, vivida immaginazione a cui io da sempre cerco di avvicinarmi.

Grazie a tutta la mia famiglia, zii, zie, cugini, la nonna Giovita e la zia Elda, per avermi cresciuta e riempita di amore. Grazie ai miei cugini, Alessandro, Francesco, Federico e Claudia, per aver condiviso un'infanzia e un'adolescenza stupenda, so che potrò sempre contare su di voi.

Ringrazio i miei compagni di classe, che sono stati molto più di questo. Siamo cresciuti insieme e continuiamo a farlo, è bellissimo sapere che dopo più di 10 anni tornando per le vacanze ci ritroviamo tutti più cresciuti, ma in fondo sempre gli stessi. La vostra amicizia è una delle cose per cui sono più grata.

Grazie Giorgia, per essere un'amica geniale e avermi sempre dato consigli preziosi, le nostre chiacchierate sono sempre state un tesoro per me e anche se la vita ci ha portato su strade diverse, spero un giorno potranno essere più frequenti.

Grazie agli amici di Barcellona, per le bellissime esperienze, le gite sfortunate con la pioggia, le notti a ballare e i viaggi improvvisati a Valencia. Lo ricorderò sempre come uno dei periodi più belli, un'esperienza che mi ha cambiato la vita.

Grazie ai ragazzi di Siemens, Antonio, Emanuele, Roberto, Maurizio, Claudio, Gian Paolo, Riccardo, Massimo, Luca, Josh, Eduardo, per aver reso unica quest'esperienza, avete colorato anche le giornate più grigie di Leuven.

Grazie ai leccesi di Torino per avermi accolta e fatta sentire in famiglia quando ero una piccola

matricola che si doveva ambientare in una città sconosciuta.

Grazie Raffa, Bianca, Rossella, Chiara, Alba, Deg, Edoardo, Turi, Lorenzo, Vez (Simone), Emanuele, siete stati i compagni di avventure di questi anni pieni di emozioni e avete reso magica Torino che adesso è un album di ricordi che affiorano da ogni angolo. Grazie perchè se questi sono stati i migliori anni della mia vita è merito vostro.

Grazie Alb, per essere stato il mio compagno di viaggio per tutti questi anni, condividendo ogni traguardo da festeggiare con doppia felicità e rendendo ogni sofferenza più sopportabile. Per avermi teso la mano ogni volta che ne avevo bisogno e per aver creduto nelle mie capacità molto più di me. Per essere la persona meravigliosa che sei e avermi regalato tanta gioia e tante risate. Custodisco nel cuore i ricordi e l'affetto immutabile che provo per te.

Grazie alla mia Nico, perché sono 19 anni che sei al mio fianco e anche se la vita ci ha portate lontane tu mi sei sempre vicina. Sei un pilastro della mia vita, perchè siamo cresciute insieme e ci siamo scelte, è da quando ricordo che abbiamo condiviso ogni momento, dal più stupido al più importante. Spero tu possa sentire il mio affetto e il mio sostegno ogni giorno tanto quanto io sento il tuo.

Grazie alle mie sorelle e coinquiline, Allegra e Francesca, per questi 6 anni pieni di emozioni. È difficile accettare che corso Mediterraneo 94 non sia più casa nostra, quelle quattro mura ne hanno viste così tante che camminando tra le stanze sento le nostre risate e mi sembra di non essere mai andata via. Grazie per avermi dato tutto il vostro affetto e sostegno ogni giorno di questi anni che ci hanno visto affrontare così tante difficoltà, ma anche così tante avventure. Grazie per esserci state dal primo all'ultimo giorno durante gli anni più belli della mia vita. Ma grazie soprattutto perchè quando sono con voi è ogni volta come tornare a casa. Anche se non vivremo più sotto lo stesso tetto, so che le Alefralle saranno sempre le stesse.

Infine, ringrazio tutti voi che mi avete accompagnato fin qui, grazie per il vostro tempo, le vostre parole, i vostri abbracci e i vostri sorrisi. Con oggi si chiude un capitolo e ne inizia uno nuovo in cui non ci sarà più qualcuno a indicarmi la via, ma dovrò trovare la mia strada da sola, questo un po' mi elettrizza e un po' mi spaventa, ma penso che a 25 anni sia normale sentirsi spaesati. Ogni nuovo inizio mi ha fatto paura, eppure adesso Lecce, Torino, Barcellona, Leuven, sono tutte casa mia, per cui non vedo l'ora di affrontare le prossime sfide che mi aspettano, sapendo che comunque ci siete tutti voi a tenermi per mano.